9

Solid-State, Dye, and Semiconductor Lasers

9.1. INTRODUCTION

Chapter 9 considers the most important types of lasers involving high-density active media, namely solid-state, dye, and semiconductor lasers. The chapter concentrates on examples in widest use whose characteristics are representative of a whole class of lasers. The main emphasis is on the laser's physical behavior and how this relates to general concepts developed in previous chapters. Some engineering details are also given with the aim of providing a better insight into the behavior of particular lasers. To complete the picture, data relating to laser performances (e.g., oscillating wavelength(s), output power or energy, wavelength tunability, etc.) are also included to suggest laser applications. The following items are generally covered for each laser: Relevant energy levels, excitation mechanisms, characteristics of the laser transition, engineering details of the laser's structure(s), characteristics of the output beam, and applications.

9.2. SOLID-STATE LASERS

The term solid-state laser is generally reserved for lasers having ions introduced as an impurity in an otherwise transparent dielectric-host material (in crystalline or glass form). Thus semiconductor lasers are not usually included in this category, the mechanisms for pumping and for laser action being in fact quite different. These are considered in a separate section.

Ions belonging to one of the series of transition elements of the Periodic Table, in particular rare earth (RE) or transition-metal ions, are generally used as the active impurities. For host crystals, either oxides, e.g., Al_2O_3, or fluorides, e.g., $YLiF_4$ (abbreviated YLF), are most often used.[1] The Al^{3+} site is too small to accommodate RE ions, so it is generally

used for transition-metal ions. A suitable combination of oxides to form synthetic garnets, such as $Y_3Al_5O_{12} = (1/2)(3\,Y_2O_3 + 5\,Al_2O_3)$, are often used and the Al^{3+} site can accommodate transition metal ions while the Y^{3+} site can be used for RE ions. Other oxides include YVO_4 for Nd^{3+} ions and alexandrite for Cr^{3+} ions. Among the fluorides, YLF is used as a host for RE, while $LiSrAlF_6$ (abbreviated LiSAF) or $LiCaAlF_6$ (abbreviated LiCAF) are used for transition metals—most notably for Cr^{3+} ions.

A comparison between oxides and fluorides shows that oxides are harder, with better mechanical and thermo-mechanical (i.e., higher thermal fracture limit) properties. Fluorides, on the other hand, show better thermo-optical properties (i.e., lower thermally induced lensing and birefringence). Glasses from either the silicate (i.e., based on SiO_2) or phosphate (i.e., based on P_2O_5) family have so far been used only for RE ions. Compared to crystals, many glasses have much lower melting temperatures; therefore they are easier and cheaper to fabricate even in large dimensions. On the other hand, glasses have much lower (by approximately an order of magnitude) thermal conductivity, which leads to much worse thermo-mechanical and thermo-optical properties. A comparison between various glasses reveals silicates to have better thermal and mechanical properties, while phosphates show better thermooptical and nonlinear optical properties.

The general electronic structure of a RE is $4f^N5s^25p^65d^06s^2$ as shown for Nd, Er, Yb, Tm, and Ho in Table 9.1, where for comparison the structure of Xe is also indicated. When a RE is inserted into a host material, the two $6s$ electrons and one of the $4f$ electrons are used for ionic binding, so that the RE presents itself as a triply ionized ion (e.g., $N-1=3$ for Nd^{3+}). The remaining $N-1$ electrons can then arrange themselves in different states of the $4f$ shell, resulting in a large number of energy levels. In fact these states are split by three types of interaction, namely, Coulomb interaction among the $4f^{N-1}$ electrons, spin-orbit coupling, and crystal-field interaction. The Coulomb interaction is the strongest of these three, and it splits the $4f$ states into sublevels typically separated by $\sim$10,000 cm^{-1}. Spin-orbit coupling then splits each term into manifolds typically separated by $\sim$3000 cm^{-1}. The

TABLE 9.1. Electronic configurations of some rare earth and transition metals of interest as laser-active impurities

Atom	Electron Configuration
Xenon, Xe[a]	$(Kr)4d^{10}5s^25p^6$
Neodymium, Nd	$(Xe)4f^45d^06s^2$
Holmium, Ho	$(Xe)4f^{11}5d^06s^2$
Erbium, Er	$(Xe)4f^{12}5d^06s^2$
Thulium, Tm	$(Xe)4f^{13}5d^06s^2$
Ytterbium, Yb	$(Xe)4f^{14}5d^06s^2$
Chromium, Cr	$(Ar)3d^54s^1$
Titanium, Ti	$(Ar)3d^24s^2$
Cobalt, Co	$(Ar)3d^74s^2$
Nickel, Ni	$(Ar)3d^84s^2$

[a] For reference, the fundamental configuration of Xe is also shown.

crystal-field interaction produces the weakest perturbation (weakened by the screening effect of $5s^2$ and $5p^6$ orbitals), thus further splitting each manifold into sublevels with an energy separation typically of 200 cm^{-1}.

All relevant absorption and emission features are due to transitions between these $4f$ states ($4f$-$4f$ transitions). Electric dipole transitions within the $4f$ shell are parity-forbidden, so it requires a mixture of wave functions with opposite parity, brought about by the crystal-field interaction, to create nonzero, although still weak, transition probabilities. Thus we generally find long (hundreds of microseconds) radiative lifetimes. Furthermore, due to the screening from the $5s^2$ and $5p^6$ orbitals, electron–phonon coupling is very weak. One thus has sharp transition lines and weak nonradiative decay channels for low ion doping. (Ion-ion interaction can lead to nonradiative decay at high RE ion concentrations, see Fig. 2.13). From the preceding considerations we expect large values of the overall lifetime τ and of the product $\sigma\tau$, where σ is the peak cross section. This implies a low threshold pump power for laser action, since, e.g., for a four-level laser, the threshold pump rate is proportional to $1/\sigma\tau$ [see Eq. (7.3.3)].

Electronic configurations for transition metals of interest in laser action are also shown in Table 9.1. Note that the electronic configuration of the most important active species, i.e., Cr, is given by $(Ar)3d^5 4s^1$, while those of Ti, Co, and Ni can be written in the general form $(Ar)3d^N 4s^2$ (with $N=2$ for Ti, 7 for Co, and 8 for Ni). When a Cr atom is added to an ionic crystal, the one electron belonging to its $4s$ orbital and two $3d$ electrons are used for ionic binding and Cr is found as a triply ionized ion with three electrons left in the $3d$ shell. In titanium, the two $4s$ electrons and one $3d$ electron are used for ionic binding, and Ti is again present as a triply ionized ion with only one electron left in the $3d$ shell. In both Co and Ni, the two $4s$ electrons are used for binding and these elements are present as doubly ionized ions. In all cases, the remaining electrons in the $3d$ orbital can arrange themselves in a large number of states (e.g., 24 for Cr^{3+}), and all absorption and emission features of transition-metal ions arise from $3d$-$3d$ transitions. Lacking the screening that occurs in RE ions, the $3d$ states interact strongly with the crystal field of the host, and, as we see later, this is the fundamental reason for the vibronic character of the corresponding transitions leading to wide absorption and emission bands. Again electric-dipole transitions within the $3d$ shell are parity-forbidden, but, due to the stronger crystal field compared to the RE case, the $3d$-$3d$ transitions are more allowed and thus the lifetimes are significantly shorter (a few microseconds) than those of the $4f$-$4f$ transitions in RE ions. Compared to Nd:YAG, e.g., transition cross sections are somewhat smaller, so that the product $\sigma\tau$ is now typically one order of magnitude smaller.

To conclude this section we observe that ions belonging to the actinide series, notably U^{3+}, were also used in the early days of laser development. (The U^{3+} laser was the second solid-state laser to be developed, i.e., immediately after the ruby laser.) These ions are no longer used, but they deserve a mention here for historic reasons.

9.2.1. Ruby Laser

This was the first type of laser made to operate (T. H. Maiman, June 1960[2,3]), and it continues to be used in some applications.[4] As a naturally occurring precious stone, ruby has been known for at least 2000 years. It consists of a natural crystal of Al_2O_3 (corundum)

in which some of the Al^{3+} ions have been replaced by Cr^{3+} ions. For the laser material, one uses artificial crystals obtained by crystal growth from a molten mixture of Al_2O_3 with a small percentage of Cr_2O_3 (0.05% by weight).[4] Without the addition of Cr_2O_3, the colorless crystal that forms is known as sapphire. Due to the strong green and violet absorption bands of Cr^{3+} ions, it needs only that small addition of Cr_2O_3 to give the crystal a pink color (pink ruby). In the case of gem stones, the Cr^{3+} concentration is about an order of magnitude larger, giving them a strong red color (red ruby).

Energy levels in ruby are due to one of the three electrons of the Cr^{3+} ion, in the $3d$ shell, under the influence of the octahedral field at the Al site in the Al_2O_3 lattice. Corresponding levels of interest for laser action are shown in Fig. 9.1. The notation used to label the levels, which is derived from group theory, is not discussed at any length here. We limit ourselves to pointing out that the superscript to the left of each letter indicates multiplicity of the state, while the letter indicates the particular rotational symmetry of the state. As an example, the ground $^4A_2$ state has multiplicity $(2S+1)=4$, i.e., $S=3/2$, where S is the total spin quantum number of the three $3d$ electrons. This means that the spins of these electrons are all parallel in this case.

Ruby has two main pump bands $^4F_1$ and $^4F_2$; transition peaks from the ground $^4A_2$ level to these bands occur at the wavelengths of 550 nm (green) and 420 nm (violet), respectively (see also Fig. 6.7). The two bands are connected by a very fast (picoseconds) nonradiative decay to both $2A$ and $\bar{E}$ states, which together form the ^2E state. The $2A$ and $\bar{E}$ states are connected to each other by a very rapid nonradiative decay, which leads to rapid thermalization of their populations; this results in the $\bar{E}$ level being the most heavily populated. Since the total spin of the ^2E state is $1/2$, the $^2E \rightarrow {}^4A_2$ transition is spin-forbidden. The relaxation time of both $2A$ and $\bar{E}$ levels to the ground state is thus very long ($\tau \cong 3$ ms), actually one of the longest among all solid-state laser materials.

From the preceding discussion, one sees that the level $\bar{E}$ accumulates the largest fraction of the pump energy; thus it is a good candidate for the upper laser level. In fact laser action usually occurs on the $\bar{E} \rightarrow {}^4A_2$ transition (R_1 line) at the wavelength $\lambda_1 = 694.3$ nm (red). Note that the frequency separation between $2A$ and E levels (~ 29 cm^{-1}) is small compared to kT/h (~ 209 cm^{-1} at $T=300$ K), so that the $2A$ population is comparable to, although slightly smaller than, the $\bar{E}$-level population. Thus, it is also possible to obtain laser action on the $2A \rightarrow {}^4A_2$ transition (R_2 line, $\lambda_1 = 692.8$ nm). Ruby operates as a three-level laser. (Together with Er lasers it represents the most noteworthy example of a three-level laser.) As already discussed in connection with Fig. 2.10, at room temperature the R_1 transition is predominantly homogeneously broadened; the broadening arises from the

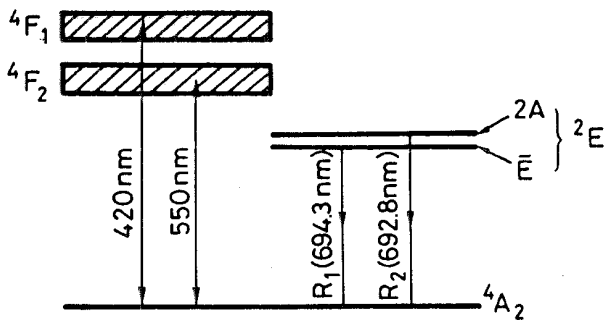

FIG. 9.1. Simplified energy levels of ruby.

interaction of Cr^{3+} ions with lattice phonons. The width of the transition (FWHM) is $\Delta\nu_0 \cong 11\ cm^{-1}$ (330 GHz) at $T = 300$ K. In summary Table 9.2 lists relevant optical and spectroscopic parameters of ruby at room temperature.

Ruby lasers are usually operated in a pulsed regime. For this, the pump configuration in Fig. 6.1, using a medium-pressure (~500 Torr) xenon flashtube, is generally used. Typical rod diameters range from 5–10 mm, with a length from 5–20 cm. Note that a helical flashtube surrounding the active rod was used in the earliest ruby lasers. Since this laser operates on a three-level scheme, threshold pump energy is typically an order of magnitude higher than that of other solid-state lasers operating with four-level schemes (e.g., neodymium lasers). Due to the long upper-state lifetime, ruby lasers lend themselves readily to Q-switched operation. Due to their relatively large laser linewidth, they can also produce short pulses (~5–10 ps) in mode-locked operation. Both active and passive methods can be used for Q-switching and mode locking. When slow saturable absorbers are used for Q-switching, the laser tends to operate in a single transverse and longitudinal mode due to the mode-selecting mechanism discussed in Sect. 8.4.2.4. With fast saturable absorbers (usually solutions of cyanine dyes), simultaneous Q-switched and mode-locked operation occurs (see Fig. 8.28a). Peak powers of a few tens of megawatts for Q-switching, and a few gigawatts when also mode-locked, are typical. Since the gain of the R_2 line is somewhat smaller than for the R_1 line, laser action on the R_2 line can be selected by using for instance the dispersive system in Fig. 7.16b. Ruby lasers can also run cw, transversely pumped by a high-pressure mercury lamp or longitudinally pumped by an Ar ion laser.

Once very popular, ruby lasers are now less widely used, since, due to their higher threshold, they have been superseded by such competitors as Nd:YAG or Nd:glass lasers. In fact, ruby lasers were extensively used in the past for the first mass production of military range finders, an application in which this laser is now completely replaced by other solid-state lasers (Nd:YAG, Nd:glass, Yb:Er:glass). However, ruby lasers are still sometimes used for a number of scientific and technical applications where its shorter wavelength compared to Nd:YAG, e.g., represents an important advantage. For example, in the case of pulsed holography, Nd:YAG lasers cannot be used due to the lack of response, in the infrared, of the high-resolution photographic materials that are used.

TABLE 9.2. Optical and spectroscopic parameters of ruby for room temperature operation

Property	Values and Units
Cr_2O_3 doping	0.05 wt.%
Cr^{3+} concentration	1.58×10^{19} ions/cm^3
Ouput wavelengths	694.3 nm (R_1 line)
	692.9 nm (R_2 line)
Upper laser level lifetime	3 ms
Linewidth of R_1 laser transition	11 cm^{-1}
Stimulated emission cross section σ_e	2.5×10^{-20} cm^2
Absorption cross section σ_a	1.22×10^{-20} cm^2
Refractive index ($\lambda = 694.3$ nm)	$n = 1.763$ ($E \perp c$)
	$n = 1.755$ ($E \parallel c$)

9.2.2. Neodymium Lasers

These are the most popular type of solid-state laser. The host medium is often a crystal of $Y_3Al_5O_{12}$ (called YAG, an acronym for yttrium aluminium garnet) in which some of the Y^{3+} ions are replaced by Nd^{3+} ions. Besides this oxide medium, other host media include some fluoride (e.g., $YLiF_4$) or vanadate (e.g., YVO_4) materials as well as some phosphate or silicate glasses. Typical doping levels in Nd:YAG, e.g., are ~ 1 atomic %. Higher doping generally leads to fluorescence quenching and strained crystals, since the radius of the Nd^{3+} ion is somewhat larger (by $\sim 14\%$) than that of the Y^{3+} ion. Doping levels used in Nd:glass are somewhat higher than the value for Nd:YAG ($\sim 4\%$ of Nd_2O_3 by weight). Undoped host materials are usually transparent; when doped, these generally become pale purple because of the Nd^{3+} absorption bands in the red.

9.2.2.1. Nd:YAG Laser

Figure 9.2 shows a simplified energy level scheme for Nd:YAG. As previously discussed, these levels arise from the three inner-shell $4f$ electrons of the Nd^{3+} ion, which are effectively screened by eight outer electrons ($5s^2$ and $5p^6$). Energy levels are only weakly influenced by the crystal field of YAG, so the Russell–Saunders coupling scheme of atomic physics can be used. Level notation is accordingly based on this scheme, and the symbol characterizing each level has the form $^{2S+1}L_J$, where S is the total spin quantum number, J is the total angular momentum quantum number, and L is the orbital quantum number. Note that the allowed values of L, namely, $L = 0, 1, 2, 3, 4, 5, 6, 7, 8, 9, \ldots$ are expressed, for historic reasons, by uppercase letters $S, P, D, F, G, H, I, L, M, N, \ldots$, respectively. Thus the $^4I_{9/2}$ ground level correspond to a state in which $2S + 1 = 4$ (i.e., $S = 3/2$), $L = 6$, and $J = L - S = 9/2$. Each level is $(2J + 1)$-fold degenerate corresponding to the quantum number m_J running from $-J$ to $+J$ in unit steps. In the octahedral symmetry of the YAG crystal-field, states with the same value of $|m_J|$ have the same energy in the presence of the Stark effect, and each $^{2S+1}L_J$ level is split into $(2J + 1)/2$ doubly degenerate sublevels. Thus the $^4I_{11/2}$ and $^4F_{3/2}$ levels are split into six and two sublevels, respectively (see Fig. 9.2). Note that, since the degeneracy of all sublevels is always the same (i.e., $g = 2$), we can disregard this degeneracy and consider each sublevel in Fig. 9.2 as if it were a single nondegenerate level.

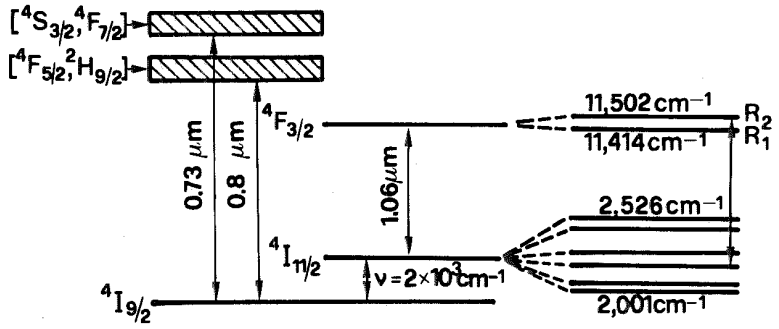

FIG. 9.2. Simplified energy levels of Nd:YAG.

The two main pump bands of Nd:YAG occur at ~730 and 800 nm, respectively, although higher lying absorption bands (see Fig. 6.7) also play an important role, notably for flashlamp pumping. These bands are coupled by a fast nonradiative decay to the $^4F_{3/2}$ level from where decay to the lower I levels occurs (to $^4I_{9/2}$, $^4I_{11/2}$, $^4I_{13/2}$, etc., levels; see Fig. 9.2 and Fig. 2.15). The rate of this decay is much slower ($\tau \cong 230$ μs), however, because this transition, in an isolated ion, is forbidden via the electric dipole interaction (the selection rule for electric-dipole-allowed transitions is $\Delta J = 0$ or ± 1) but becomes weakly allowed due to crystal-field interaction. Note that nonradiative decay is not so important because decay due to ion-ion interactions (see Fig. 2.13b) does not play an important role at the stated Nd ion concentrations. Multiphonon decay is also not so effective due both to the screening of the of $5s^2$ and $5p^6$ states and the large energy gap between $^4F_{3/2}$ and the nearest level below it. This means that level $^4F_{3/2}$ accumulates a large fraction of the pump power, so that it is a good candidate as the upper level for laser action.

From the preceding discussion, one sees that several laser transitions are possible between $^4F_{3/2}$ and several lower lying I levels; of these transitions, $^4F_{3/2} \rightarrow {}^4I_{11/2}$ is the strongest one. Level $^4I_{11/2}$ is then coupled by a fast (hundreds of picoseconds) nonradiative decay to the $^4I_{9/2}$ ground level, so that thermal equilibrium between these two levels is very rapidly established. Since the energy difference between $^4I_{11/2}$ and $^4I_{9/2}$ levels is almost an order of magnitude larger than kT, then, according to Boltzmann statistics, level $^4I_{11/2}$ may, to a good approximation, be considered empty at all times. Thus laser operation on the $^4F_{3/2} \rightarrow {}^4I_{11/2}$ transition corresponds to a four-level scheme. According to the preceding discussion, the $^4F_{3/2}$ level is split by the Stark effect into two sublevels (R_1 and R_2), while the $^4I_{11/2}$ level is split into six sublevels. Laser action usually occurs from the upper R_2 sublevel to a particular sublevel of the $^4I_{11/2}$ level, since this transition has the highest value for the stimulated emission cross section. The transition occurs at $\lambda = 1.064$ μm (near-infrared), which is the most widely used lasing wavelength for Nd:YAG lasers. Note that laser action can also be obtained on the $^4F_{3/2} \rightarrow {}^4I_{13/2}$ transition (see Fig. 2.15; $\lambda = 1.319$ μm is the strongest transition wavelength in this case) provided the multilayer dielectric coatings of the cavity mirrors have high reflectivity at $\lambda = 1.319$ μm and sufficiently low reflectivity at $\lambda = 1.064$ μm (see Fig. 4.9). With diode laser pumping, laser action has also been made to occur efficiently on the $^4F_{3/2} \rightarrow {}^4I_{9/2}$ transition. In this case the transition, at a wavelength $\lambda = 946$ nm (see Fig. 2.15), is to a sublevel of the $^4I_{9/2}$ state, which, despite being a high-lying sublevel, is still appreciably populated according to Boltzmann statistics; the system thus operates as a quasi-three-level laser. In the case of the usual $\lambda = 1.064$-μm transition, and probably for all other cases, the laser transition is homogeneously broadened at room temperature via interaction with lattice phonons. The corresponding width is $\Delta\nu \cong 4.2$ cm^{-1} = 126 GHz at $T = 300$ K (see Fig. 2.10). This makes Nd:YAG a good candidate for mode-locked operation; pulses as short as 5 ps have, indeed, been obtained by passive mode locking (see Example 8.8). The long lifetime of the upper laser level ($\tau \cong 230$ μs) also makes Nd:YAG very suitable for Q-switched operation. Table 9.3 gives a summary of relevant optical and spectroscopic parameters for Nd:YAG at room temperature.

Nd:YAG lasers can operate either cw or pulsed, and can be pumped by either a lamp or an AlGaAs semiconductor laser.[5] For lamp pumping, linear lamps in single-ellipse (Fig. 6.1a), close-coupling (Fig. 6.1b), or multiple-ellipse configurations (Fig. 6.2) are commonly used. Medium pressure (500–1500 Torr) Xe lamps and high-pressure (4–6 atm) Kr lamps

TABLE 9.3. Optical and spectroscopic parameters of Nd:YAG ($\lambda = 1.064$ μm), Nd:YVO_4, Nd:YLF ($\lambda = 1.053$ μm), and Nd:glass (phosphate)

	Nd:YAG $\lambda = 1.064$ μm	Nd:YVO_4 $\lambda = 1.064$ μm	Nd:YLF $\lambda = 1.053$ μm	Nd:glass $\lambda = 1.054$ μm (Phosphate)
Nd doping	1 atom.%	1 atom.%	1 atom.%	3.8% by weight of Nd_2O_3
N_t (10^{20} ions/cm^3)[a]	1.38	1.5	1.3	3.2
τ (μs)[b]	230	98	450	300
$\Delta\nu_0$ (cm^{-1})[c]	4.5	11.3	13	180
σ_e (10^{-19} cm^2)[d]	2.8	7.6	1.9	0.4
Refractive index	$n = 1.82$	$n_o = 1.958$ $n_e = 2.168$	$n_o = 1.4481$ $n_e = 1.4704$	$n = 1.54$

[a] N_t is the concentration of the active ions, [b] τ is the fluorescence lifetime, [c] $\Delta\nu_0$ is the transition linewidth (FWHM), [d] σ_e is the effective stimulated emission cross section. Data refer to room temperature operation.

are used for the pulsed and cw cases, respectively. If a rod is used as the active medium, the rod diameter ranges typically from 3–6 mm, with a length from 5–15 cm. To reduce pump-induced thermal lensing and thermal birefringence, a slab configuration (Fig. 6.3a) is also used. The slope efficiency is about 3% for both cw and pulsed operation; average output powers up to a few kW (1–3 kW) are common. Longitudinally diode-pumped lasers (Fig. 6.11) with cw output powers up to ~15 W and transversely diode-pumped lasers (Figs. 6.14 and 6.15) with cw output powers well above 100 W are now available. The slope efficiency for diode pumping is much higher than for lamp pumping, and may exceed 10%.

Nd:YAG lasers are widely used in a variety of applications, including: (1) Material processing, such as drilling and welding. In drilling applications, the beam of a repetitively pulsed laser is focused on the material (average powers of 50–100 W are commonly used with pulse energy $E = 5$–10 J, pulse duration $\Delta\tau_p = 1$–10 ms, and pulse repetition rate $f = 10$–100 Hz). In welding applications, a repetitively pulsed laser beam is conveyed to the working region through a 0.5–2-mm diameter optical fiber (average power as high as 2 kW are now commonly handled in this way). In this application, high-power Nd:YAG lasers supersede their direct competitors (high-power CO_2 lasers) due to the system flexibility offered by an optical-fiber delivery. (2) Medical applications. In coagulation and tissue evaporation, cw Nd:YAG lasers with powers as high as 50 W are used; the beam is delivered, through an optical fiber inserted into a conventional endoscope, to the internal organs (lungs, stomach, bladder) of the human body. Repetitively Q-switched Nd:YAG lasers are used for photodisruption of transparent membranes of pathological origin, which can appear in the anterior chamber of the eye (e.g., secondary cataract) or for iridectomy. (3) Laser ranging, in particular for laser range-finders and target designators used in a military context which use Q-switched lasers ($E \approx 100$ mJ, $\Delta\tau_p = 5$–20 ns, $f = 1$–20 Hz). (4) Scientific applications. In this case Q-switched lasers with their second-harmonic ($\lambda = 532$ nm), third-harmonic ($\lambda \cong 355$ nm), and fourth-harmonic beams ($\lambda = 266$ nm), as well as mode-locked lasers are commonly used. It should lastly be noted that diode-pumped Nd:YAG lasers with intracavity second-harmonic generation giving a green ($\lambda = 532$ nm) cw output power up to ~10 W are now available. They provide an all-solid-state alternative to the Ar laser for many of its applications.

9.2.2.2. Nd:Glass Laser

As previously mentioned, relevant transitions of the Nd^{3+} ion involve the three electrons of the $4f$ shell, which are screened by eight outer electrons in the $5s$ and $5p$ configuration.[6] Accordingly, the energy levels of Nd:glass are approximately the same as those of Nd:YAG. Thus the strongest laser transition again occurs at about the same wavelength ($\lambda \cong 1.054$ μm for phosphate glass; see Table 9.3). Laser transition linewidths are, however, much larger, due to inhomogeneous broadening arising from local field inhomogeneities typical of a glass medium. In particular, the main $\lambda \cong 1.054$-μm laser transition is much broader (by $\sim$40 times) while the peak cross section is somewhat smaller (by $\sim$7 times) than that of Nd:YAG. A larger bandwidth is of course a desirable feature for mode-locked operation; diode-pumped passively mode-locked Nd:glass lasers have in fact produced femtosecond pulses ($\sim$100 fs). A smaller cross section is a desirable feature for pulsed high-energy systems, since the threshold inversion for the parasitic process of ASE [see Eq. (2.9.4)] is correspondingly increased. Thus more energy per unit volume can be stored in Nd:glass than in Nd:YAG before the onset of ASE (see Example 2.13). Note that, due to its lower melting temperature, glass can be fabricated more easily than YAG, so that active media of much larger dimensions can be produced. Since the pump absorption bands of Nd:glass are also much broader than those of Nd:YAG and Nd^{3+} concentrations are typically twice as great, the pumping efficiency of a lamp-pumped Nd:glass rod is somewhat larger ($\sim$1.6 times) than that of a Nd:YAG rod of the same dimensions (see Table 6.1). Against these advantages of Nd:glass compared to Nd:YAG, we must set the disadvantage of its much lower thermal conductivity. (The thermal conductivity of glass is about ten times smaller than that of Nd:YAG.) This has restricted applications of Nd:glass lasers mainly to pulsed laser systems of rather low repetition rate (<5 Hz), so that thermal problems in the active medium (rod or slab) can be avoided.*

As previously discussed, Nd:glass lasers are often used in applications where a pulsed laser with a low-repetition rate is required, for instance in some military range finders and some scientific Nd lasers. A very important application of Nd:glass is in laser amplifiers in the very high-energy systems used in laser-driven fusion experiments. Systems based on Nd:glass amplifiers have indeed been built in several countries, the largest one being in the United States (Nova laser, Lawrence Livermore National Laboratory); it delivers pulses with an energy of $\sim$100 kJ and peak power of 100 TW ($\Delta\tau_p = 1$ ns). The laser uses a chain of several Nd:glass amplifiers; the largest consists of Nd:glass disks (see Fig. 6.3b) each disk of $\sim$4 cm in thickness and $\sim$75 cm in diameter. A national ignition facility delivering pulses of much higher energy ($\sim$10 MJ, Lawrence Livermore National Laboratory) and a similar system delivering about the same output energy ($\sim$2 MJ, Limeil Center) are presently being built in the United States and France, respectively.

9.2.2.3. Other Crystalline Hosts

Many other crystal materials have been used as hosts for the Nd^{3+} ion, but we limit ourselves here to mentioning $YLiF_4$ (YLF) and YVO_4.

* An exception is the glass fiber laser, where long length and small transverse dimension eliminate the thermal problem and have allowed cw outputs in excess of 30 W.

Compared to YAG, YLF has better thermooptical (pump-induced thermal lensing and thermal birefringence) properties;[7] lamp-pumped Nd:YLF lasers are thus used to obtain TEM_{00}-mode cw beams of better quality and higher output power. The larger linewidth of Nd:YLF compared to Nd:YAG (approximately three times; see Table 9.3) makes Nd:YLF lasers particularly attractive for mode-locked operation with both lamp and diode pumping (see Example 8.8). The mechanical and thermo-mechanical properties of YLF are however worse than those of YAG, which make YLF rods more difficult to handle and easier to break. Note that the 1053-nm emission wavelength of Nd:YLF provides a good match with the peak gain wavelength of Nd:glass:phosphate lasers (see Table 9.3). Mode-locked Nd:YLF lasers are accordingly used as the first stage in the large energy systems used for laser fusion experiments.

Compared to Nd:YAG, $Nd:YVO_4$ has a much larger peak cross section ($\sigma_e \cong 7.6 \times 10^{-19}$ cm^2) and much shorter fluorescence lifetime ($\tau = 98$ μs). The product $\sigma\tau$ is about the same for the two cases, so we expect approximately the same threshold. For a given inversion, however, the gain coefficient of $Nd:YVO_4$ is about three times larger than that of Nd:YAG, which makes $Nd:YVO_4$ lasers less sensitive to cavity losses. Longitudinally diode-pumped $Nd:YVO_4$ of high-cw power ($\sim$15 W) are now commercially available; for this kind of laser, $Nd:YVO_4$ seems to be preferred to Nd:YAG.

9.2.3. Yb:YAG Laser

The Yb:YAG laser is the most noteworthy example of a quasi-three-level laser. Since it oscillates at $\sim$1.03-μm wavelength, it is a direct competitor to the Nd:YAG laser. Since it operates on a quasi-three-level laser scheme, it is usually pumped by semiconductor laser diodes to provide the intense pumping required.[8]

Figure 9.3 shows a simplified scheme of the energy level diagram of Yb:YAG. The level structure is particularly simple here—only one excited manifold $^2F_{5/2}$ is present because Yb^{3+} is one electron short of a full $4f$ shell (see Table 9.1); this shell thus acts as if it contained one electron hole. The two main absorption lines occur at 968 and 941 nm, respectively; the two lines have approximately the same value of peak absorption cross

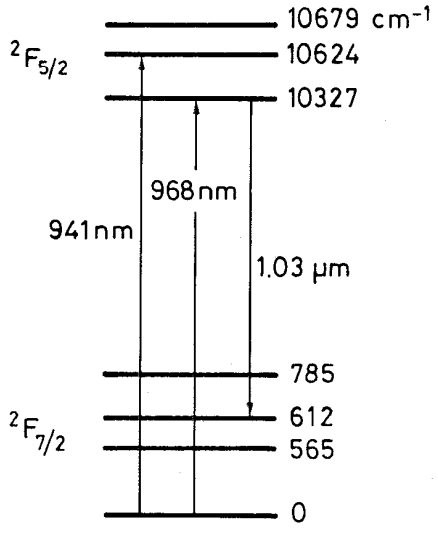

FIG. 9.3. Energy level diagram of Yb:YAG.

section (see Fig. 6.8b). The line at 941 nm is usually preferred for diode pumping due to its larger width. The main gain line occurs at 1.03 μm (quasi-three-level laser). Table 9.4 lists some relevant optical and spectroscopic parameters for Yb:YAG at room temperature. Note the long lifetime $\tau = 1.16$ ms, of essentially radiative origin, which indicates a good storage medium.

Yb:YAG lasers are pumped in a longitudinal pumping configuration using a pump at $\lambda_p = 943$-nm wavelength, usually by InGaAs/GaAs strained quantum well lasers, although they can also be pumped by a Ti:sapphire laser. The optical-to-optical efficiency is very high (~60%), a result mainly due to the high pump quantum efficiency ($\eta_q = h\nu/h\nu_p = \lambda_p/\lambda = 91.5\%$).[9] Average output powers well in excess of 50 W have so far been achieved.[10] Compared to Nd:YAG, the Yb:YAG laser offers the following favorable properties:

1. Very low-quantum defect [$(h\nu_p - h\nu)/h\nu_p \cong 9\%$] and hence very low fractional heating.
2. Long radiative lifetime of the upper state, making Yb:YAG a good medium for Q-switching.
3. High doping levels (due to the simple energy level structure)—6.5 at.% are usually used without incurring fluorescence-quenching due to ion-ion interaction.
4. Broad emission bandwidth (~86 cm^{-1}), indicating suitability for mode-locked operation (subpicosecond pulses have indeed been obtained).
5. Low stimulated-emission cross section allowing high energy to be stored before the onset of ASE.

In contrast to these favorable properties, the main limitation of Yb:YAG comes from the high threshold, a result of its quasi-three-level nature and from its low stimulated-emission cross section. The various features of Yb:YAG discussed above suggest that it may be better suited than Nd:YAG for many applications where a diode-pumped laser at a wavelength around 1 μm is needed.

TABLE 9.4. Optical and spectroscopic parameters at room temperature of the most important quasi-three-level laser materials

Active Medium Parameters	Yb:YAG $\lambda = 1.03$ μm	Nd:YAG $\lambda = 946$ μm	Tm:Ho:YAG $\lambda = 2.091$ μm	Yb:Er:Glass[a] $\lambda = 1.54$ μm (Phosphate)
Doping (atom.%)	6.5 atom.	1.1 atom.		
N_t (10^{20} ions/cm^3)	8.97	1.5	8 (Tm) 0.5 (Ho)	10 (Yb) 1 (Er)
τ (ms)	1.16	0.23	8.5	8
$\Delta\nu_0$ (cm^{-1})	86	9.5	42	120
σ_e (10^{-20} cm^2)	1.8	2.4	0.9	0.8
σ_a (10^{-20} cm^2)	0.12	0.296	0.153	0.8
Refractive index	$n = 1.82$	$n = 1.82$	$n = 1.82$	$n = 1.531$

[a] For Yb:Er:glass, the effective value of the stimulated emission and absorption cross sections are about the same, so the laser can be considered to operate in (almost) a pure three-level scheme.

9.2.4. Er:YAG and Yb:Er:Glass Lasers

Erbium lasers can emit radiation at either $\lambda = 2.94$-μm wavelength (for Er:YAG) or at $\lambda = 1.54$-μm wavelength (for Yb:Er:glass).[11] The former wavelength is particularly interesting for biomedical applications, while the latter wavelength is attractive for application situations where eye safety is important and for optical communications in the third transparency window of optical fibers.

In the case of Er:YAG, the Er^{3+} ion occupies some Y^{3+} ion sites in the lattice; Fig. 9.4a shows relevant energy levels of the laser. Laser oscillation can take place on either the $^4I_{11/2} \rightarrow {}^4I_{13/2}$ transition ($\lambda = 2.94$ μm)[12] or the $^4I_{13/2} \rightarrow {}^4I_{15/2}$ transition ($\lambda \cong 1.64$ μm). Due to their interest for biomedical applications, Er:YAG lasers, oscillating on the $\lambda = 2.94$-μm transition, are the subject of much development. The spectroscopy of Er:YAG indicates that, for flashlamp excitation, the $^4I_{11/2}$ upper laser level is pumped by light absorbed from transitions at wavelengths shorter than 600 nm. For diode laser pumping, diode lasers oscillating at $\lambda = 970$ nm (InGaAs/GaAs strained QW) are used. The lifetime of the upper state ($\sim$0.1 ms) is much shorter than that of the lower state ($\sim$2 ms); therefore the laser is usually operated in a pulsed regime. Despite this unfavorable lifetime ratio the laser can also operate cw under the usual operating conditions, particularly when diode pumped. This occurs because, due to the high Er concentrations used (10–50 at.%), a strong Er^{3+}-Er^{3+} interaction occurs, thus leading to an efficient $^4I_{13/2} \rightarrow {}^4I_{9/2}$ up-conversion transition (see Fig. 2.13c). This process leads to energy recycling from the $^4I_{13/2}$ lower level to the $^4I_{11/2}$ upper-laser level.

In a flash-lamp-pumped configuration, the Er:YAG rod dimensions are typically comparable to those of a flash-lamp-pumped Nd:YAG laser (e.g., 6-mm diameter $\times$ 7.5 cm length); it is usually pumped using either an elliptical cylinder or a close-coupling pumping chamber (Fig. 6.1). Flash-lamp-pumped Er:YAG lasers with output energies up to 1 J and repetition rates up to 10 Hz are commercially available. Due to the very strong water absorption around $\lambda = 2.94$ μm, flash-lamp-pumped Er:YAG lasers are particularly interesting for biomedical applications and, in particular, for plastic surgery. The human body in fact consists of $\sim$70% water and the skin penetration depth of a 2.94-μm wavelength Er:YAG laser is around 5 μm. More recently, diode-pumped Er:YLF lasers oscillating at $\lambda = 2.8$ μm have produced cw operation with good optical-to-optical slope efficiency ($\sim$35%) and sufficiently high output power (>1 W).

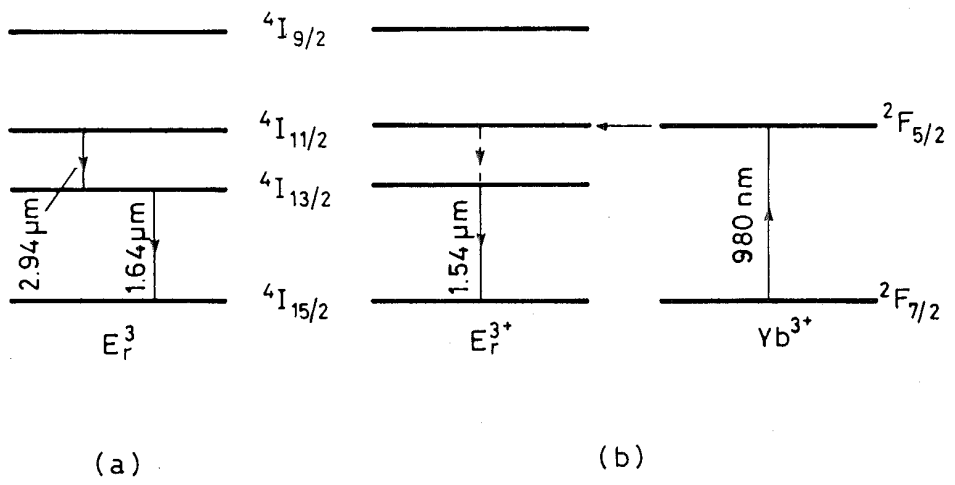

FIG. 9.4. Relevant energy levels of: (a) Er:YAG and (b) Yb:Er:phosphate glass.

Figure 9.4b shows relevant energy levels of the Yb:Er:phosphate-glass laser. The laser can be pumped by either a flashlamp[13] or a cw diode;[14] it usually oscillates on the $^4I_{13/2} \rightarrow {}^4I_{15/2}$ transition ($\lambda = 1.54$ μm). For 1.54-μm Er lasers, the Er concentration must be kept low to avoid the detrimental effect, in this case, of the up-conversion mechanism previously mentioned. For both flashlamp and diode laser pumping, Er absorption coefficients are then too small for efficient laser operation; to increase pump absorption, codoping with Yb^{3+} ions (and Cr^{3+} ions for flashlamp pumping) is used. With diode pumping around the 980-nm wavelength, pump power is mainly absorbed by Yb^{3+} ions ($^2F_{7/2} \rightarrow {}^2F_{5/2}$ transition); excitation is then effectively transferred to the $^4I_{11/2}$ Er level by a Förster-type dipole-dipole interaction (see Sect. 2.6.1). The $^4I_{11/2}$ Er level then decays relatively quickly ($\tau \cong 0.1$ ms), by multiphonon relaxation, to the $^4I_{13/2}$ upper laser level. The lifetime of this level in phosphate glass is particularly long ($\tau \cong 8$ ms), thus making it very suitable for laser action. Note that the peak of the gain spectrum of Er:glass is, only slightly, Stokes shifted to longer wavelengths compared to the peak of the absorption spectrum; both spectra arise, in fact, from several transitions between the $^4I_{13/2}$ and the $^4I_{15/2}$ manifolds. Thus the Yb:Er:glass laser behaves almost like a pure three-level laser. Table 9.4 shows other relevant spectroscopic and optical properties of the Yb:Er:glass laser.

Q-switched flash-lamp-pumped Cr:Yb:Er:glass lasers are used as eye-safe range finders. The 1.5-μm wavelength is in fact particularly safe for the eye.[15] Diode-pumped cw Yb:Er:glass lasers have potential applications in optical communications and for free-space optical measurements where eye safety is of concern.

9.2.5. Tm:Ho:YAG Laser

Figure 9.5 shows relevant energy levels of the Tm:Ho:YAG laser.[16] Both Tm^{3+} and Ho^{3+} ions occupy Y^{3+}-ion sites in the lattice. Typical Tm concentrations are rather high (4–10 at.%), while the concentration of Ho ions is an order of magnitude smaller. In flashlamp pumping, the active medium is also sensitized by Cr^{3+} ions, which are substituted for Al^{3+} ions in the YAG crystal. In this case, the pump energy is absorbed mainly by the $^4A_2 \rightarrow {}^4T_2$ and $^4A_2 \rightarrow {}^4T_1$ transitions* of the Cr^{3+} ions, then efficiently transferred to the $^3F_4$ level of

* According to group theory, the $^4T_2$ and $^4T_1$ notations for the Cr^{3+} ion in an octahedral crystal field, used here, are equivalent to the old $^4F_2$ and $^4F_1$ notations used for ruby (see Fig. 9.1).

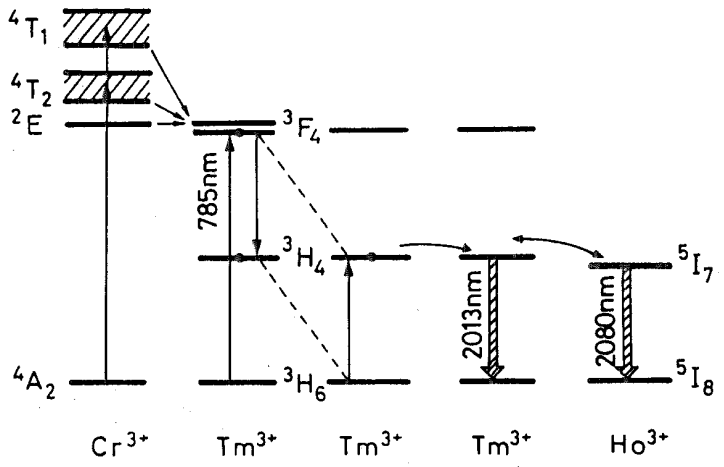

FIG. 9.5. Relevant energy level diagram of Cr:Tm:Ho:YAG system.

the Tm^{3+} ion by a Förster-type ion-ion interaction. For cw diode pumping, the $^3F_4$ level of Tm^{3+} is pumped directly by AlGaAs semiconductor lasers at a 785-nm wavelength, so that codoping with Cr^{3+} ions is not needed. For both flash-lamp and diode-laser pumping, excitation to the $^3F_4$ level of Tm^{3+} ion is then followed by a cross-relaxation process between adjacent ions, of the form $Tm(^3F_4) + Tm(^3H_6) \rightarrow 2Tm(^3H_4)$. This process converts one excited Tm ion in the $^3F_4$ state into two excited Tm ions, both of which are left in the $^3H_4$ state. For the high Tm concentrations used, this cross-relaxation process dominates the $^3F_4$ radiative decay, leading to an overall pump quantum efficiency of nearly 2. A fast spatial migration of the excited energy between Tm ions, again due to Förster-type ion-ion interaction, then occurs until excitation reaches a Tm ion very near a Ho ion. In this case, energy transfer to the $^5I_7$ level of Ho occurs, followed by laser action on the $Ho^{3+}(^5I_7 \rightarrow {}^5I_8)$ transition. Laser action actually occurs between the lowest sublevel of the $^5I_7$ manifold to a sublevel, $\sim 462\ cm^{-1}$ above the ground sublevel, of the $^5I_8$ manifold at $\lambda = 2.08$-μm wavelength (quasi-three-level laser). Without Ho-doping, the crystal can lase on the $^3H_4 \rightarrow {}^3H_6$ Tm transition at $\lambda = 2.02$-μm wavelength.

When flashlamp pumped, the active medium is in the form of a rod of the same typical dimensions as those of the Er:YAG rod considered in Sect. 9.2.4 and again pumped in an elliptical cylinder or close-coupling configuration (see Fig. 6.1). Output energies to 1 J in a ~ 200 μs long pulse and a slope efficiency to 4% with a repetition rate below 10 Hz are typical laser operating figures. This laser may find interesting applications in the biomedical field, since biological tissue also has a strong absorption around 2 μm (although much less strong than at the 2.94-μm wavelength of the Er laser). When diode pumped, a longitudinal pumping configuration, such as that in Fig. 6.11a, is often used. Given the strong absorption coefficient of Tm^{3+} ions at the pump wavelength ($\alpha_p \cong 6\ cm^{-1}$), the thickness of the active medium is now typically 2–3 mm; the medium is generally cooled to low temperatures (−10 to −40°C) to reduce the thermal population of the lower laser level.

Eye-safe coherent laser radar systems using Tm:Ho:YAG lasers are used for remote measurement of wind velocity in the atmosphere. This involves using a single-frequency diode-pumped Tm:Ho laser to injection seed a flashlamp-pumped, Pockels-cell-Q-switched, Cr:Tm:Ho:YAG slave oscillator.

9.2.6. Fiber Lasers

In a fiber laser the active medium is the core of the fiber doped with a rare earth.[17] Most commonly, this is a single-mode fiber made of silica. The pump beam is launched longitudinally along the fiber length and it may be guided by either the core itself, as occurs for the laser mode (a conventional single-mode fiber laser), or by an inner cladding around this core (double-clad fiber laser). Note that, although fiber lasers were first demonstrated in the early days of laser development,[18] they have become of practical interest only in recent years after the advent of suitable diode lasers allowing efficient pumping and of techniques for fabricating doped single-mode silica fibers.

In a conventional single-mode fiber, the transverse dimensions of both pump w_p and laser w_0 beams are comparable to the core radius a (typically $a \cong 2.5$ μm). Thus both w_p and w_0 are 10–50 times smaller than corresponding typical values for a bulk device (see Examples 7.4 and 7.5). From Eqs. (6.3.19) and (6.3.24), for a four-level and a quasi-three-level laser, respectively, the threshold pump power P_{th} is seen to be proportional to

$(w_0^2 + w_p^2)$. Hence, for the same values of laser parameters (e.g., γ, σ_e, η_p, τ for a four-level laser), P_{th} is expected to be smaller in a fiber laser compared to a bulk device by two to three orders of magnitude. Thus, according to Examples 7.4 and 7.5, threshold pump powers well below 1 mW are expected and indeed achieved in fiber lasers. This argument also shows that laser action can be obtained for active media of very low radiative quantum efficiency and hence of very short lifetime τ. On the other hand, the expression for laser slope efficiency for both a four-level and a quasi-three-level laser [the two are identical; see Eqs. (7.3.13) and (7.4.10)] is independent of the upper state lifetime; it depends only on pump efficiency η_p. Thus, even for a transition with a low radiative quantum efficiency, a high laser slope efficiency can be obtained if most of the pump power is absorbed (i.e., $\eta_p \cong 1$). Therefore, transitions that look unpromising in bulk media can still show a high slope efficiency and a low enough threshold in a fiber, when diode-pumped. It should be noted that an interesting effect, occurring at the high pump powers (to $\sim$100 mW; see Sect. 6.3.1) available from single-transverse-mode diode lasers, is ground-state depletion. Consider, for instance, a four-level laser, such as Nd:glass, and let F_p be the pump photon flux (assumed for simplicity to be uniform in the core) and N_g and N_2 be the populations of the ground level and upper-laser level, respectively. In the absence of laser action and under cw conditions, we can simply write the following balance equation

$$\sigma_p F_p N_g = (N_2/\tau) \tag{9.2.1}$$

where σ_p is the pump absorption cross section and τ is the upper state lifetime. Thus, when $N_g = N_2$, one must have $F_p = (I_p/h\nu_p) = (1/\sigma_p\tau)$, where I_p is the pump intensity and $h\nu_p$ is the energy of a pump photon. According to Fig. 6.8a and Table 9.3, for a Nd:silica fiber one has $\sigma_p = 2.8 \times 10^{-20}$ cm^2 and $\tau = 300$ μs. From the previous expression, one obtains $I_p = (h\nu_p/\sigma_p\tau) \cong 25$ kW/cm^2 so that $P_p = I_p A_{core} \cong 0.25$ mW, where A_{core} is the area of the core taken to be $\approx 10^{-7}$ cm^2. Thus, in the example considered, more than half of the ground-state population is raised to the upper laser level at pump powers below 1 mW. Given the ease with which pump-induced depletion of the ground-state population occurs, it follows that typical pump powers can deplete absorption over lengths very much exceeding the small-signal extinction length ($l = 1/\alpha_p$, where α_p is the small-signal absorption coefficient at the pump wavelength). In fact, it can be shown that, if the pump power exceeds this saturation power P_p by a factor x, the pump power penetrates the fiber to a distance roughly x times the extinction length. This circumstance must be taken into account in choosing the optimum fiber length.

Conventional end-pumped single-mode fibers require a diffraction-limited pump source for efficient pumping. So, for diode pumping, only the single-stripe device in Fig. 6.9a meets this requirement; consequently the pump power is limited to $\sim$100 mW ($\sim$1 W in the case of Master Oscillator Power Amplifier diode lasers) and output power is limited correspondingly. High-power diode lasers (see Figs. 6.9b and 6.10) display poor beam quality unsuitable for direct launch into the end of the fiber core. The solution to this problem is provided by *cladding-pumping* and illustrated in Fig. 9.6. The core, which may be monomode, lies within a lower index inner cladding that in turn lies within an outer cladding of a yet lower index. Pump light can be end-launched into the inner cladding with a much less stringent beam quality requirement than into the core. While propagating in the inner cladding, this pump light is progressively absorbed by the core with an effective absorption

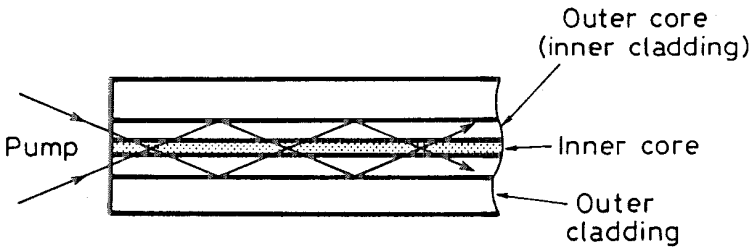

FIG. 9.6. Scheme of cladding pumping.

coefficient smaller than the core's true absorption coefficient by a factor of the order of the ratio of the inner-cladding area to the core area. Thus, for a given core doping, fiber length must be correspondingly increased to allow efficient absorption of pump power. Provided propagation losses of the pump in the inner cladding and of the lasing mode in the core are not excessively increased by an increase in fiber length, then efficient pumping by a multimode diode and efficient monomode lasing can be achieved. Thus the cladding-pumping scheme can provide a very simple means of enhancing the brightness of a (diode) pump source by efficiently converting it to a monomode laser output. Cladding-pumped Nd-doped fibers and Yb-doped fibers with output powers of several watts (4–10 W) are commercially available, and power levels in excess of 30 W have been demonstrated.

As just discussed, the high values of pump intensity available from laser pumping enable a considerable fraction of the ground-state population, in a conventional monomode fiber, to be raised to some upper level of the active ion. Under this condition, a second pump photon of the same or different wavelength can therefore raise this population to a still higher level. From this level, laser action can then take place to a lower level, so that the energy of the emitted photon is actually higher than each pump photon energy (see Fig. 9.7). A laser working on such a scheme where two or more than two pump photons of equal or different wavelength are used, is referred to as an *up-conversion laser.*

While such schemes work with bulk media, they are much more practical with fiber lasers exploiting fiber materials of a special kind. In silica fibers in fact, the main limitations to this up-conversion scheme stem from nonradiative decay of the levels involved, usually occurring by multiphonon deactivation. As explained in Sect. 2.6.1, the probability of such a decay is a very strong function of the number of phonons that must be emitted in the process. In this case the relevant phonon energy is the maximum energy in the phonon spectrum of the host material, since the nonradiative decay rate increases strongly, for a given transition, with increasing values of this energy. For fused silica this energy corresponds to $\sim 1150\ \text{cm}^{-1}$, which results in rapid nonradiative decay for energy gaps less than $\sim 4500\ \text{cm}^{-1}$. A substantial reduction in the rate of nonradiative decay is obtained by using

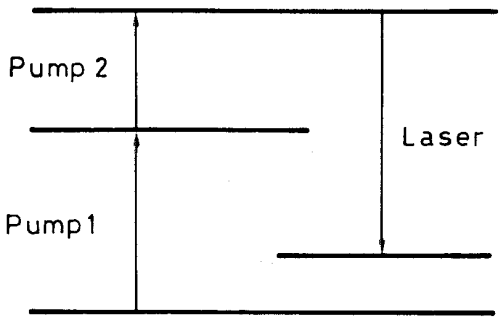

FIG. 9.7. Scheme of an up-conversion laser.

host materials with lower phonon energy. Among the materials that can be fabricated into fibers, the most widely used one consists of a mixture of heavy-metal fluorides, referred to as ZBLAN [an acronym for zirconium, barium, lanthanum, aluminium, and sodium (Na)], which, due to the heavy metals, has a maximum phonon energy of only 590 cm^{-1}. A few years ago, the undoped fiber was available at an advanced stage of development since, due to the correspondingly reduced infrared absorption of heavy-metal fluorides, it was developed as a possible route to ultra-low-loss fibers for communications.

As an example of performance capability, when pumped by three photons of the same wavelength ($\lambda = 1120$–1150 nm), ZBLAN fibers doped with Tm^{3+} have produced a very efficient up-conversion laser in the blue ($\lambda = 480$ nm), giving output powers in excess of 200 mW. When pumped by two photons at ~1010 nm and ~835 nm, ZBLAN fibers doped with Pr^{3+} have produced laser action on several transitions from blue to red ($\lambda = 491$, 520, 605, 635 nm), giving, e.g., as high as ~20 mW output power in the blue. These figures hold promise for a practical all-solid-state blue up-conversion laser source.

9.2.7. Alexandrite Laser

Alexandrite, chromium-doped chrysoberyl, is a crystal of $BeAl_2O_4$ in which Cr^{3+} ions replace some of the Al^{3+} ions (0.04–0.12 at.%).[19] This laser may be considered the archetype of what is now a large class of solid-state lasers, usually referred to as *tunable solid-state lasers*. The emission wavelength of these lasers can in fact be tuned over a wide spectral bandwidth (e.g., $\Delta\lambda \cong 100$ nm around $\lambda = 760$ nm for alexandrite). Tunable solid-state lasers include, among others, Ti:sapphire and Cr:LiSAF, considered in the following sections, as well as Co:MgF_2 ($\Delta\lambda \cong 800$ nm around $\lambda = 1.9$ μm), Cr^{4+}:YAG ($\Delta\lambda \cong 150$ nm around $\lambda = 1.45$ μm), and Cr^{4+}:Forsterite (Cr^{4+}:Mg_2SiO_4, $\Delta\lambda \cong 250$ nm around $\lambda = 1.25$ μm). In this category we can also include color center lasers,[20] which are broadly tunable in the near infrared (at wavelengths from 0.8–4 μm). Once rather popular, color center lasers have declined in popularity and importance due to problems associated with handling and storing the active medium and to the advent of new competitors in the same wavelength range (i.e., other tunable solid-state lasers or parametric oscillators, considered in Chap. 12). For these reasons they are not considered further here.

Energy states of the Cr^{3+} ion in $BeAl_2O_4$ are qualitatively similar to those of Cr^{3+} in other hosts with octahedral crystal field, such as ruby, as already considered. To explain why alexandrite laser is tunable while ruby is not, at least not to the same extent, we refer to a simplified scheme in Fig. 9.8 for energy states as a function of a configuration coordinate of the Cr^{3+} ion (i.e., the distance between this ion and the six surrounding O^{2-} anions of the octahedron; see Fig. 3.3). Figure 9.8 shows that, due to their symmetry, the equilibrium coordinate for both $^4T_2$ and $^4T_1$ states is shifted to a larger value than that of $^4A_2$ and ^2E states.* As in other Cr^{3+}-doped hosts, the decay between the $^4T_2$ and ^2E states is by a fast internal conversion (decay time of less than 1 ps), probably due to the level crossing that occurs between the two states. These two states can therefore be considered in thermal equilibrium at all times; since the energy difference between the lowest vibrational levels of $^4T_2$ and ^2E states in alexandrite ($\Delta E \cong 800$ cm^{-1}) is only a few kT, an appreciable

* As already pointed out, the $^4T_2$ and $^4T_1$ notations for the Cr^{3+} ion, considered here, are equivalent to the old $^4F_2$ and $^4F_1$ notations used for ruby (see Fig. 9.1).

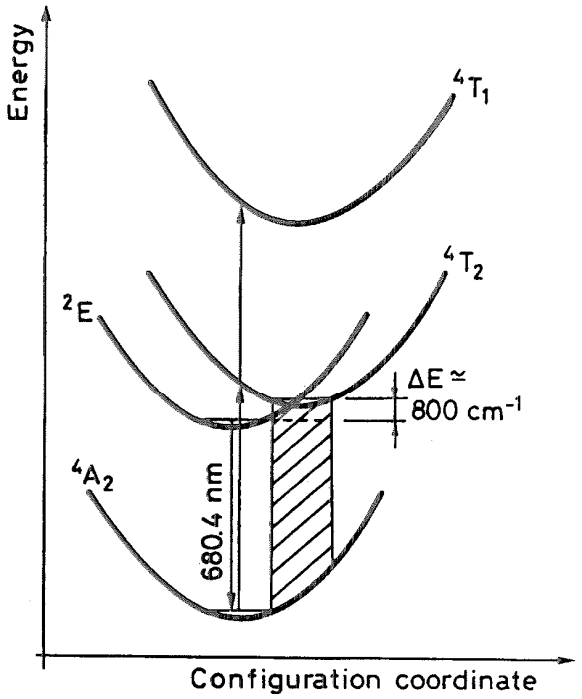

FIG. 9.8. Energy level diagram of alexandrite laser in a configuration coordinate model.

population is present in the vibrational manifold of the $^4T_2$ state when the ^2E state is populated. Invoking the Franck–Condon principle, one sees that vibronic transitions from the $^4T_2$ state end in empty vibrational levels of the $^4A_2$ state, thus becoming the preferred laser transition. Since a very large number of vibrational levels are involved, the resulting emission is in the form of a broad continuous band ($\lambda = 700$–800 nm). Excitation is then terminated by phonon decay to the lowest vibrational level of the $^4A_2$ state. In keeping with the preceding physical description, this type of laser is also referred to as a *phonon-terminated laser* or a *vibronic laser.*

It should be noted that, in ruby laser, laser action takes place between the ^2E and $^4A_2$ states, while phonon-terminated transitions do not occur. This is because the energy difference between the $^4T_2$ (old $^4F_2$) and ^2E states is much larger ($\Delta E \cong 2300$ cm^{-1}) and, hence, there is no appreciable population in the $^4F_2$ level. Note also that, in alexandrite, laser action can occur, as for ruby, on the $^2E \rightarrow {}^4A_2$ transition (compare Fig. 9.8 and Fig. 9.1). In this case, however, alexandrite operates on a three-level scheme, the threshold is much higher, and the emission wavelength occurs at a somewhat different value ($\lambda = 680.4$ nm).

Pumping in alexandrite takes place mostly through its green and blue absorption bands ($^4A_2 \rightarrow {}^4T_2$ and $^4A_2 \rightarrow {}^4T_1$ transitions; see Fig. 9.8), which are very similar to those of ruby. The effective values of the lifetime and stimulated emission cross sections of the $^4T_2$ upper laser state can be roughly calculated by assuming that the upper level consists of two strongly coupled levels with energy spacing of $\Delta E \cong 800$ cm^{-1}. These levels are the lowest vibrational levels of the $^4T_2$ and ^2E states (see Fig. 2.16 and Example 2.11). At $T = 300$ K the upper state lifetime then turns out to be $\tau \cong 200$ μs, which is almost the same as that of Nd:YAG. Note that, although the true lifetime of the $^4T_2$ state is much shorter ($\tau_T \cong 6.6$ μs), the effective lifetime is considerably increased by the presence of the long-lived ^2E state ($\tau_E \cong 1.5$ ms; $^2E \rightarrow {}^4A_2$ is spin-forbidden), which thus acts as a reservoir for the $^4T_2$ state. Due to the coupling of these two states, the effective cross section of the laser transition

($\sigma_e \cong 0.8 \times 10^{-20}$ cm^2) is then considerably smaller than the true value. Note also that both τ and σ_e are temperature dependent because the relative population of the two states depends on temperature. Table 9.5 summarizes some optical and spectroscopic data relevant to the tunable laser transition of alexandrite.

From an engineering point of view, alexandrite lasers are similar to Nd:YAG lasers; in fact alexandrite lasers are usually lamp-pumped in a pumping chamber as in Figs. 6.1 or 6.2. Although they can operate cw, the much smaller cross section than that of, e.g., Nd:YAG makes pulsed operation more practical. The laser can operate in either the free-running regime (output pulse duration ~200 μs) or Q-switched regime (output pulse duration ~50 ns); it is usually pulsed at a relatively high repetition rate (10–100 Hz). Due to the strong increase in the effective emission cross section with temperature, the laser rod is usually held at an elevated temperature (50–70°C). Performances of a pulsed alexandrite laser, in terms of output versus input energy and slope efficiency, are similar to those of Nd:YAG using a rod of the same dimensions. Average powers, up to 100 W at pulse repetition rates of ~250 Hz have been demonstrated. Flash-lamp-pumped alexandrite lasers have proved useful when high average power at $\lambda \cong 700$ nm wavelength is needed (such as in laser annealing of silicon wafers) or tunable radiation is required (as in pollution monitoring).

9.2.8. Titanium Sapphire Laser

The titanium sapphire (Ti:Al_2O_3) laser is the most widely used tunable solid-state laser.[21–23] It can in fact be operated over a broad tuning range ($\Delta\lambda \cong 400$ nm, corresponding to $\Delta\nu_0 \cong 100$ THz), thus providing the largest bandwidth of any laser. To make Ti:sapphire, Ti_2O_3 is doped into a crystal of Al_2O_3 (typical concentrations range between 0.1–0.5% by weight), so that Ti^{3+} ions occupy some of the Al^{3+}-ion sites in the lattice. The Ti^{3+} ion possesses the simplest electronic configuration among transition ions, only one electron being left in the 3*d* shell. The second 3*d* electron and the two 4*s* electrons of the Ti atom (see Table 9.1) are in fact used for ionic binding to oxygen anions. When Ti^{3+} is substituted for an Al^{3+} ion, the Ti ion is situated at the center of an octahedral site whose

TABLE 9.5. Optical and spectroscopic parameters at room temperature of the most important tunable solid-state laser materials

Active Medium Parameters	Alexandrite	Ti:sapphire	Cr:LiSAF	Cr:LiCAF
Doping (at.%)	0.04–0.12	0.1	up to 15	up to 15
N_t (10^{19} ions/cm^3)[a]	1.8–5.4	3.3	10	10
Peak wavelength (nm)	760	790	850	780
Tuning range (nm)	700–820	660–1180	780–1010	720–840
σ_e (10^{-20} cm^2)	0.8	28	4.8	1.3
τ (μs)	260	3.2	67	170
$\Delta\nu_0$ (THz)	53	100	83	64
Refractive indices	$n_a = 1.7367$ $n_b = 1.7421$ $n_c = 1.7346$	$n_o = 1.763$ $n_e = 1.755$	$n_e = 1.4$	$n_e = 1.39$

[a] The density of active ions N_t for both Cr:LiSAF and Cr:LiCAF is given at ~1% molar concentration of CrF_3 in the melt.

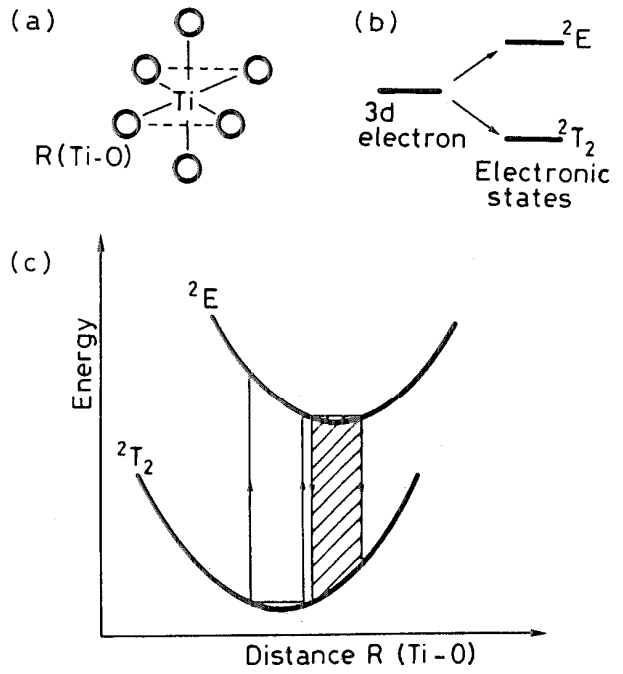

FIG. 9.9. (a) Octahedral configuration of Ti:Al_2O_3, (b) splitting of 3*d* energy states in an octahedral crystal field, and (c) energy states in a configuration coordinate model.

six apexes are occupied by O^{2-} ions (Fig. 9.9a). Assuming for simplicity a field of perfect octahedral symmetry,* the fivefold degenerate (neglecting spin) *d*-electron levels of an isolated Ti^{3+} ion are split, by the crystal field of the six nearest neighbor oxygen anions, into a triply degenerate $^2T_2$ ground state and a doubly degenerate ^2E upper state (Fig. 9.9b). As usual, the notation for these crystals incorporating a transition metal is derived from group theory. When spin is also taken into account ($S=1/2$ for this essentially one-electron system), the two states acquire a multiplicity of $2S+1=2$, as denoted by the superscript to the left of each letter. In a configuration coordinate model, where this coordinate is just the Ti-O separation, the two states are represented as in Fig. 9.9c. Note that the rather strong interaction of the 3*d* electron with the crystal field results in a considerably larger equilibrium distance for the upper state than the lower state. This circumstance is particularly relevant because it produces absorption and fluorescence bands that are wide and widely separated, as shown in Fig. 9.10. The Ti^{3+} ion in an octahedral site has only one excited state (i.e., the ^2E state)—a particularly relevant feature. This eliminates the possibility of excited state absorption (e.g., arising from the $^4T_2 \rightarrow {}^4T_1$ transition in alexandrite), an effect that limits the tuning range and reduces the efficiency of many other transition metal lasers.

Based on the preceding discussion and using the Franck–Condon principle, it follows that laser action takes place from the lowest vibrational level of the ^2E state to some vibrational level of the ground $^2T_2$ state. Table 9.5 lists some relevant optical and spectroscopic properties of this phonon-terminated transition. The upper state lifetime ($\tau \cong 3.2$ μs at $T=300$ K; the radiative lifetime is $\tau_r \cong 3.85$ μs) is much shorter than for alexandrite because, unlike alexandrite, there is no lengthening effect due to a reservoir of population in another excited state. The stimulated emission cross section, on the other hand,

* For a more exact treatment, see Refs. 21 and 22.

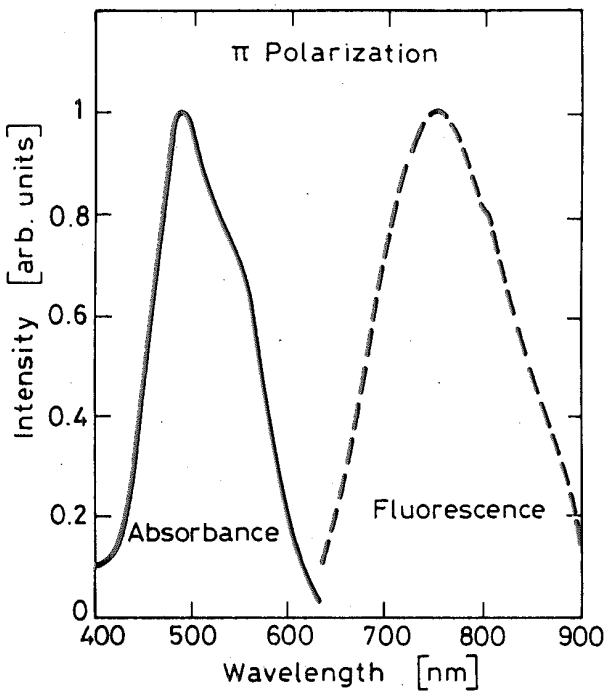

FIG. 9.10. Absorption and fluorescence bands of Ti:sapphire. (By permission from Ref. 55.)

is much (~40 times) larger than in alexandrite; it is comparable to that of Nd:YAG. Note the large bandwidth of the laser transition which is, in fact, the largest among commonly used solid-state lasers.

Usually, cw Ti:sapphire lasers are pumped by the green output of an Ar laser, while, in pulsed operation, frequency-doubled Nd:YAG or Nd:YLF lasers as well as flashlamps are used. Due to the small value of the $\sigma\tau$ product, flashlamp pumping requires very intense lamps; nonetheless flashlamp-pumped Ti:sapphire lasers are commercially available. Argon-pumped cw lasers provide a convenient source of coherent and high-power (>1 W) light, which is tunable over a wide spectral range (700–1000 nm). Perhaps the most important application of Ti:sapphire lasers is generating (see Sect. 8.6.5) and amplifying (see Chap. 12) femtosecond laser pulses. Sophisticated systems based on Ti:sapphire lasers and Ti:sapphire amplifiers, giving pulses of relatively large energy (20 mJ–1 J) with femtosecond duration (20–100 fs) are now operating in several laboratories and also available commercially.

9.2.9. Cr:LiSAF and Cr:LiCAF Lasers

Two of the most recently developed tunable solid-state materials, based on Cr^{3+} as the active species, are Cr^{3+}:$LiSrAlF_6$ (Cr:LiSAF) and Cr^{3+}:$LiCaAlF_6$ (Cr:LiCAF).[24,25] Both materials offer a wide tuning range and the corresponding lasers can be either flashlamp pumped or diode-laser pumped. In both Cr:LiSAF and Cr:LiCAF, Cr^{3+} ions replace some of the Al^{3+} ions in the lattice, and the impurity ion occupies the center of a (distorted) octahedral site surrounded by six fluorine ions. Thus, to a first approximation, the general energy level picture in the configuration coordinate representation, as presented for alexandrite, also holds in this case (see Fig. 9.8). Figure 9.11 shows the corresponding absorption and fluorescence spectra for the electric field parallel or perpendicular to the *c*-axis of the crystal (LiSAF and LiCAF are uniaxial crystals) for Cr:LiSAF. Note that the two

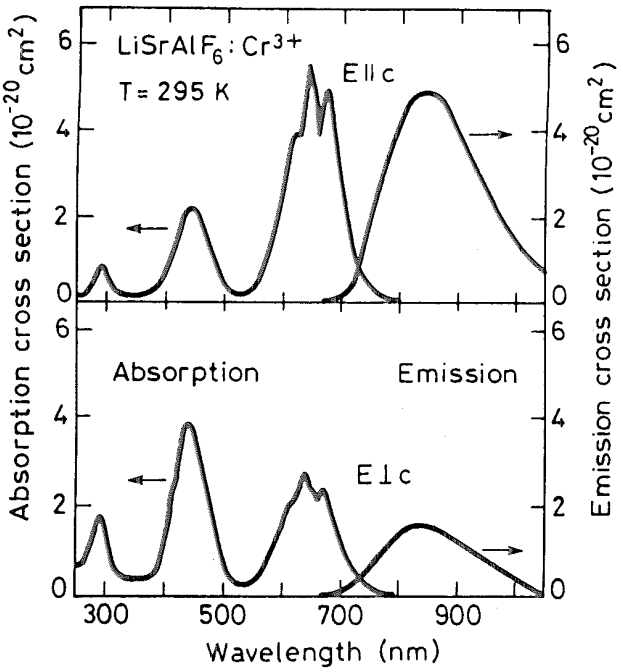

FIG. 9.11. Absorption and fluorescence bands of Cr:LiSAF for polarization parallel and perpendicular to the optical *c*-axis of the crystal. (By permission from Ref. 24.)

main absorption bands centered at 650 nm and 440 nm, respectively, arise from $^4A_2 \rightarrow {}^4T_2$ and $^4A_2 \rightarrow {}^4T_1$ transitions. Note also that the sharp features superimposed on the $^4T_2$ band arise from absorption to the ^2E and $^2T_1$ states. (The latter state is not shown in Fig. 9.8.) Thus the ^2E state is now located within the $^4A_2 \rightarrow {}^4T_2$ absorption band, which implies that the lowest vibrational level of $^4T_2$ must now be located appreciably below the ^2E state. Due to rapid relaxation between the two states, it follows that the most heavily populated state is now $^4T_2$; therefore the ^2E state does not play a role as an energy reservoir, as for alexandrite. This is also evidenced by the fact that the measured lifetime of the $^4T_2$ state is roughly independent of temperature. Table 9.5 lists other relevant optical and spectroscopic parameters of the two laser materials. Among the tunable solid-state laser materials in Table 9.5, Cr:LiSAF exhibits the largest value for the $\sigma\tau$ product. Thus, due to its larger values for both the cross section and $\sigma\tau$ product and its wider tuning range (the tuning range of Cr:LiCAF is limited by excited state absorption), Cr:LiSAF is generally preferred to Cr:LiCAF.

Cr:LiSAF is used as a flashlamp or diode-pumped laser source, providing tunability around 850 nm; the large gain linewidth makes this medium attractive for generating femtosecond pulses. For this application, Kerr lens mode-locked Cr:LiSAF lasers, end pumped by GaInP/AlGaInP QW laser diodes at ~670-nm wavelength in a configuration such as that shown in Fig. 8.31, have been developed. Large flash-lamp-pumped Cr:LiSAF amplifier systems to amplify femtosecond pulses from either a Ti:sapphire or a Cr:LiSAF mode-locked laser have also been developed. Other potential applications of Cr:LiSAF are in tunable systems for pollution monitoring and spectroscopy.

9.3. DYE LASERS

Dye lasers use an active medium consisting of a solution of an organic dye in a liquid solvent, such as ethyl or methyl alcohol, glycerol, or water.[26] Organic dyes constitute a

large class of polyatomic molecules containing long chains of conjugated double bonds [e.g., $(-CH=)_n$)]. Laser dyes usually belong to one of the following classes: (1) Polymethine dyes, which provide laser oscillation in the red or near infrared (0.7–1.5 μm); as an example Fig. 9.12a shows the chemical structure of the dye 3,3′ diethyl thiatricarbocyanine iodide, which oscillates in the infrared (at a peak wavelength $\lambda_p = 810$ nm). (2) Xanthene dyes, whose laser operation is in the visible; as an example Fig. 9.12b shows the chemical structure of the widely used rhodamine 6G dye ($\lambda_p = 590$ nm). (3) Coumarin dyes, which oscillate in the blue-green region (400–500 nm); as an example Fig. 9.12c shows the chemical structure of coumarin 2, which oscillates in the blue ($\lambda_p = 450$ nm).

9.3.1. Photophysical Properties of Organic Dyes

Organic dyes usually show wide absorption and fluorescence bands without sharp features; the fluorescence is Stokes-shifted to longer wavelengths than the absorption, a feature reminiscent of tunable solid-state laser materials considered in preceding sections. As an example Fig. 9.13 shows relevant absorption and emission characteristics of rhodamine 6G in ethanol solution.

To understand the origin of features shown in Fig. 9.13, we must first consider the energy levels of a dye molecule. A simple understanding of these levels is obtained from the so-called free-electron model,[27] which is illustrated here by considering the case of the cyanine dye shown in Fig. 9.14a. The π-electrons of the carbon atoms are then seen to form two planar distributions, one above and one below the plane of the molecule (dotted regions in Fig. 9.14a–b). The π-electrons are assumed to move freely within their planar

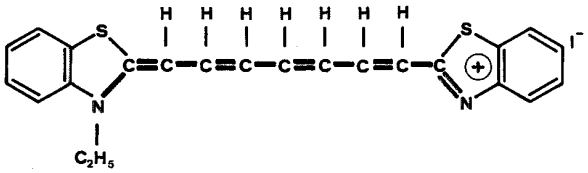

(a)

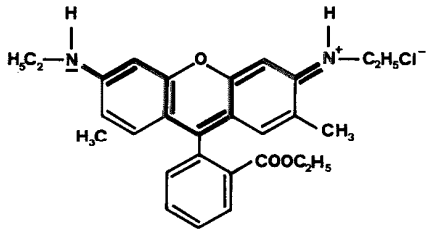

(b)

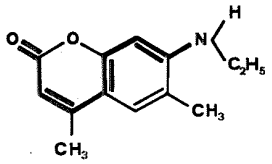

(c)

FIG. 9.12. Chemical structure of some common dyes: (a) 3,3′ diethyl thiatricarbocyanine iodide, (b) rhodamine 6G, and (c) coumarin 2. In each case the chromophoric region of the dye is indicated by heavier lines.

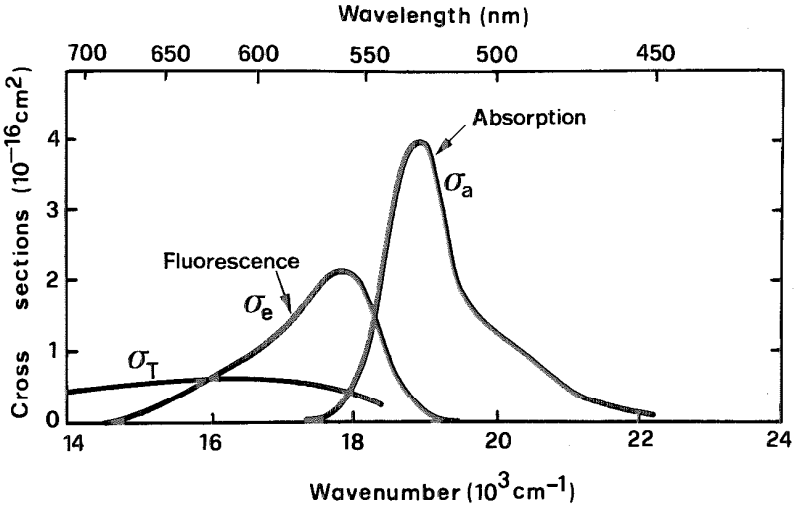

FIG. 9.13. Absorption cross section σ_a, singlet-singlet stimulated emission cross section σ_e, and triplet-triplet absorption cross section σ_T for an ethanol solution of rhodamine 6G.

distributions, limited only by the repulsive potential of the methyl groups at the end of the dye chain; electronic states of the molecule originate from these electrons. To first order, energy levels of the electrons are then simply those of a free electron in a potential well of the form shown in Fig. 9.14c. If this well is approximated by a rectangular one (Fig. 9.14d), the energy levels are known to be given by

$$E_n = \frac{h^2 n^2}{8mL^2} \tag{9.3.1}$$

where n is an integer, m is the electron mass, and L is the length of the well. It should be noted here that stable dye molecules have an even number of electrons in the π-electron

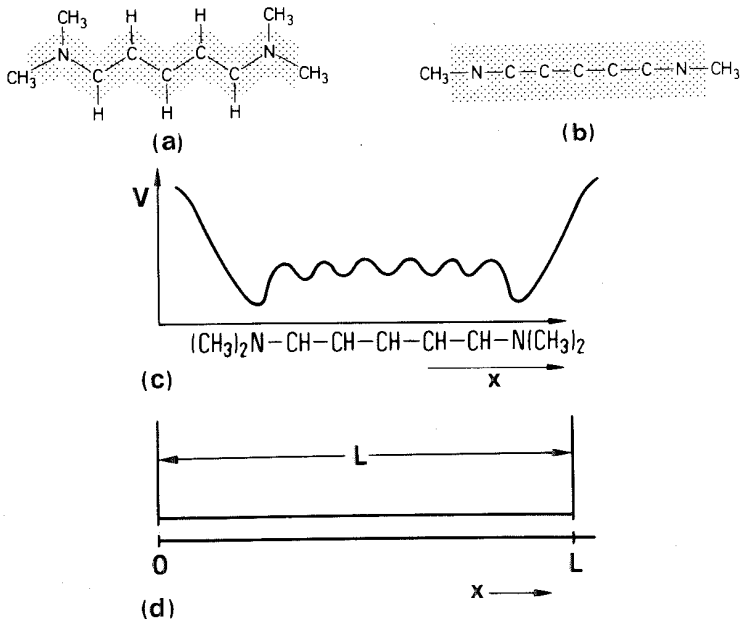

FIG. 9.14. Free electron model for the electronic energy states of a dye molecule. (By permission from Ref. 27.)

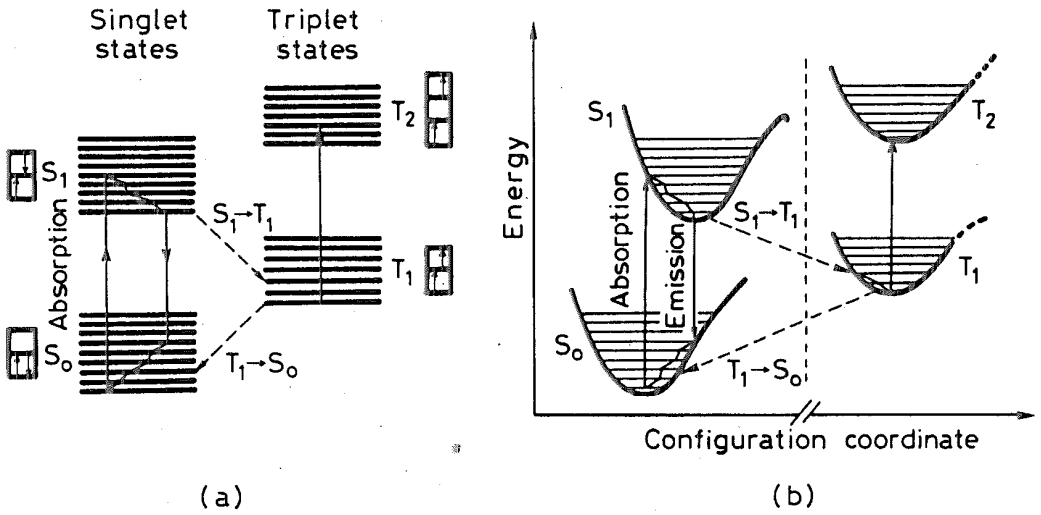

FIG. 9.15. (a) Typical energy levels for a dye in solution. The singlet and triplet states are shown in separate columns. (b) Energy level diagram of a dye in a configuration coordinate representation. (By permission from Ref. 28 with data taken from Ref. 57.)

cloud.* If we then let the number of these electrons be $2N$, the lowest energy state of the molecule corresponds to the situation where these electrons occupy the lowest N energy levels; each level is occupied by two electrons with opposite spin. This molecular state thus has a total spin equal to zero, so it is a singlet state, labeled S_0 in Fig. 9.15. An approximate value for the energy of the uppermost electrons of this state E_N is obtained from Eq. (9.3.1) by letting $n=N$. In Fig. 9.15a the highest occupied level and the next one above it are indicated by two squares, one above the other; the S_0 state thus corresponds to the situation when the lower box is full, having two electrons, and the upper one is empty. The first excited singlet state (labeled S_1 in the figure) corresponds to when one of the two highest lying electrons is promoted without flipping its spin to the next level up. The energy of the uppermost electron of this state E_{N+1} can be roughly calculated from Eq. (9.3.1) by letting $n=N+1$. The difference of energy between the S_1 and S_0 states is thus seen to be equal to $E_{N+1}-E_N$. According to Eq. (9.3.1) this difference can then be shown to decrease with increasing length L of the chain. If the spin if flipped, the total spin is $S=1$ and the resulting state is a triplet state, labeled T_1 in the figure. Excited singlet S_2 and triplet T_2 states result when the electron is promoted to the next higher level, and so on. Note in Fig. 9.15a that the corresponding energy levels are indicated by a close set of horizontal lines representing the inclusion of vibrational energy. In Fig. 9.15b, the energy states and the vibrational levels of a dye molecule are represented as a function of a configuration coordinate (i.e., a coordinate describing one of the many vibrational modes that a long-chain dye molecule has). Note that, due to the large number of vibrational and rotational levels involved and the effective line-broadening mechanisms in liquids, the rotational-vibrational structure is in fact unresolved at room temperature.

We now look at what happens when the molecule is subjected to electromagnetic radiation. First we recall that selection rules require $\Delta S=0$. Hence singlet-singlet as well as triplet-triplet transitions are allowed, while single-triplet transitions are forbidden. Therefore interaction with electromagnetic radiation can raise the molecule from the ground level S_0 to some vibrational levels of the S_1 state, taking into account the Franck–Condon principle (see Fig. 9.15b) or, more precisely, the corresponding Franck–Condon factors (see Sect. 3.1.3).

* Molecular systems with unpaired electrons are known as radicals; these tend to react readily, thus forming a more stable system with paired electrons.

Since the vibrational and rotational structure is unresolved, the absorption spectrum then shows a broad and featureless transition, as in Fig. 9.13 for the case of rhodamine 6G. Dyes have a very large dipole matrix element μ because the π-electrons are free to move over a distance roughly equal to the chain length L and, since L is quite large, it follows that μ is also large ($\mu \approx eL$). It then follows that the absorption cross section σ_a, which is proportional to μ^2, is also large ($\sim 10^{-16}$ cm^2; see Fig. 9.13).

Once in the excited state, the molecule nonradiatively decays in a very short time ($\tau_{nr} \cong 100$ fs due to collisional deactivation) to the lowest vibrational level of the S_1 state (Fig. 9.15).* From there it decays radiatively to some vibrational level of the S_0 state, taking into account again the Franck–Condon principle (Fig. 9.15b). The fluorescent emission then takes the form of a broad and featureless band, Stokes-shifted to the long wavelength side of the absorption band (see Fig. 9.13). Due to the large value of the dipole moment μ, the stimulated emission cross section is also expected to be quite large again ($\sim 10^{-16}$ cm^2; see Fig. 9.13). Having dropped to an excited vibrational level of the ground S_0 state, the molecule then returns to the lowest vibrational state by another very fast (~ 100 fs) nonradiative decay.

It should be noted that, while the molecule is in the lowest level of S_1, it can also decay to the T_1 state. This process is referred to as *intersystem crossing*; although radiatively forbidden, it may occur rather readily from collisions. Similarly, the transition $T_1 \rightarrow S_0$ takes place mainly by near-resonant energy-transfer collisions with species within the solution (e.g., dissolved oxygen) provided these collisions preserve the total spin of the colliding partners, in accordance with the Wigner rule (see Sect. 6.4.1.1). Note that, while the molecule is in the lowest level of T_1, it can also absorb radiation to undergo the $T_1 \rightarrow T_2$ transition, which is optically allowed. Unfortunately this absorption tends to occur in the same wavelength region where stimulated emission occurs (see again for example Fig. 9.13) and it may represent a serious obstacle to laser action.

The three decay processes just considered, occurring from states S_1 and T_1, can be characterized by the following three constants: (1) τ_{sp}, the spontaneous emission lifetime of the S_1 state; (2) k_{ST}, the intersystem crossing rate (s^{-1}) of the $S_1 \rightarrow T_1$ transition; and (3) τ_T, the lifetime of the T_1 state. If we let τ be the overall lifetime of the S_1 state, then, according to Eq. (2.6.18):

$$\frac{1}{\tau} = \frac{1}{\tau_{sp}} + k_{ST} \tag{9.3.2}$$

Due to the large value of the dipole matrix element μ, the radiative lifetime falls in the nanosecond range (e.g., $\tau_{sp} \cong 5$ ns for rhodamine 6G). Since k_{ST}^{-1} is usually much longer (e.g., ~ 100 ns for rhodamine 6G), it follows that most of the molecules decay from the S_1 state by fluorescence. The fluorescence quantum yield (number of photons emitted by fluorescence divided by number of molecules raised to the S_1 state) is therefore nearly unity. In fact, according to Eq. (2.6.22) one has

$$\phi = \frac{\tau}{\tau_{sp}} \tag{9.3.3}$$

* More precisely, thermalization among the many rotational-vibrational levels of this state occurs.

TABLE 9.6. Range of optical and spectroscopic parameters of typical dye laser media

Active Medium Parameter	Values
Wavelengths (nm)	320–1500
Concentration (molar)	10^{-3}–10^{-4}
N_t (10^{19} mol/cm^3)	0.1–1
σ_e (10^{-16} cm^2)	1–4
σ_T (10^{-16} cm^2)	0.5–0.8
$\Delta\lambda$ (nm)	25–50
τ (ns)	2–5
k_{ST}^{-1} (ns)	≈ 100
τ_T (s)	10^{-7}–10^{-3}
Refractive index	1.3–1.4

The triplet lifetime τ_T depends on the dye solution and, particularly, on the amount of dissolved oxygen. The lifetime can range from 10^{-7} s in an oxygen-saturated solution to 10^{-3} s or more in a deoxygenated solution.

As a summary, Table 9.6 lists typical ranges of various relevant optical and spectroscopic parameters of dye laser media.

9.3.2. Characteristics of Dye Lasers

From the preceding discussion we see that these materials have the appropriate characteristics for exhibiting laser action, over the wavelength range of fluorescence, in a four-level laser scheme. In fact rapid nonradiative decay within the excited singlet state S_1 populates the upper laser level very effectively, while rapid nonradiative decay within the ground state is effective in depopulating the lower laser level. It was however quite late in the general development of laser devices before the first dye laser was operated (1966),[29,30] and we now look for some reasons for this.

One problem that presents itself is the very short lifetime τ of the S_1 state, since the required pump power is inversely proportional to τ. Although this is to some extent compensated for by the comparatively large value of the stimulated emission cross section, the product $\sigma\tau$ [for a four-level laser, the threshold pump power is inversely proportional to $\sigma\tau$; see Eqs. (7.3.12) and (6.3.20) for the space-independent and space-dependent model, respectively] is still about three orders of magnitude smaller for, e.g., rhodamine 6G than Nd:YAG. A second problem arises from intersystem crossing. In fact, if τ_T is long compared to k_{ST}^{-1}, then molecules accumulate in the triplet state, resulting in absorption at the laser wavelength due to the triplet-triplet transition. In fact a necessary condition for laser action is that τ_T is less than some particular value that depends on other optical parameters of the dye molecule. To obtain this result, let N_2 and N_T be populations of the upper laser state and the triplet state, respectively. A necessary condition for laser action can then be established by requiring the gain coefficient, due to stimulated emission, to exceed the intrinsic loss, due to triplet-triplet absorption, i.e.

$$\sigma_e N_2 > \sigma_T N_T \tag{9.3.4}$$

where σ_T is the cross section for triplet-triplet absorption; the values for both σ_e and σ_T are taken at the wavelength where laser action is considered. In the steady state, the rate of decay of triplet population N_T/τ_T must equal the rate of increase due to intersystem crossing $k_{ST}N_2$, i.e.:

$$N_T = k_{ST}\tau_T N_2 \tag{9.3.5}$$

Combining Eqs. (9.3.4) and (9.3.5) we obtain

$$\tau_T < \frac{\sigma_e}{\sigma_T k_{ST}} \tag{9.3.6}$$

which is a necessary condition for cw laser action [i.e., equivalent to Eq. (7.3.1) for a simple two-level system]. If this condition is not satisfied, the dye laser can operate only in a pulsed regime. In this case the duration of the pump pulse must be short enough to avoid that an excessive population accumulates in the triplet state. Finally, a third crucial problem stems from the presence of thermal gradients produced in the liquid by the pump. These tend to produce refractive index gradients and hence optical distortions that can prevent laser action.

Dye lasers can be operated pulsed or, when Eq. (9.3.6) is satisfied, also cw. Pulsed laser action is obtained from many different dyes by using one of the following pumping schemes: Fast and intense flashlamps, with pulse duration usually less than ~ 100 μs, or short light pulses from another laser. In both cases, the short pulse duration produces laser action before an appreciable population accumulates in the triplet state and before the onset of refractive index gradients in the liquid.

For flashlamp pumping, linear lamps in an elliptical cylinder pumping chamber (see Fig. 6.1a) are used; the liquid containing the active medium flows through a glass tube placed along the second focal line of the ellipse. To achieve better pumping uniformity and hence more symmetric refractive index gradients, annular flashlamps consisting of two concentric glass tubes, with the dye solution in a central glass tube, are also used.

Nitrogen lasers are sometimes used for pulsed laser pumping; the uv output beam is suitable for pumping many dyes that oscillate in the visible range.* To obtain more energy and higher average power, the more efficient excimer lasers (in particular KrF and XeF) are increasingly used as uv pumps; for dyes with emission wavelength longer than $\sim$550–600 nm, the second harmonic of a Q-switched Nd:YAG laser ($\lambda = 532$ nm) or the green and yellow emissions of a copper vapor laser are increasingly used. For these visible pump lasers, the conversion efficiency from pump laser to dye laser output is higher (30–40%) than that obtained with uv laser pumping ($\sim$10%). Furthermore, dye degradation due to pump light is considerably reduced. For all the cases considered above, involving pulsed laser pumping, a transverse pump configuration (i.e., direction of the pump beam orthogonal to the resonator axis) is generally adopted (Fig. 9.16). The laser pump beam is focused by the lens L, generally a combination of a spherical and cylindrical lens, to a fine line along the axis of the laser cavity. The length of the line focus is made equal to that of the dye cell (a few millimeters), while transverse dimensions are generally less than 1 mm. To tune the output wavelength within the wide emission band of a dye ($\sim$30–50 nm wide), a grazing-

* In this case pump light is usually absorbed by the $S_0 \rightarrow S_2$ transition of the dye, then rapidly transferred to the bottom of the S_1 state.

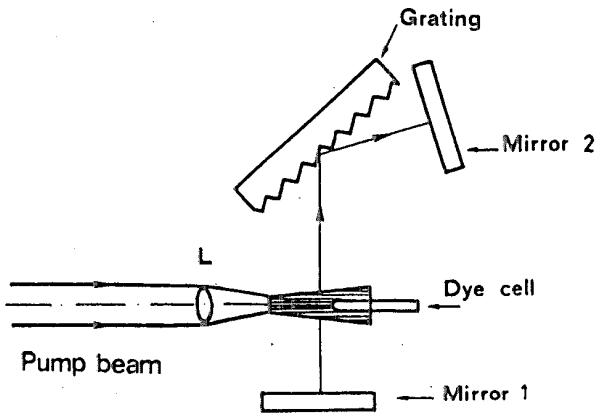

FIG. 9.16. Arrangement for a transversely pumped dye laser. The pumping beam can be a nitrogen, excimer, copper vapor laser, or the second harmonic beam of a Q-switched Nd:YAG laser.

incidence diffraction grating is commonly inserted in the laser cavity (see Fig. 9.16); tuning is achieved by rotating the mirror labeled mirror 2 in the figure. Grazing incidence increases the resolving power of the grating* and hence considerably reduces the bandwidth of the emitted radiation (to ~0.01–0.02 nm). Smaller bandwidths, down to single-mode operation, are obtained by inserting one or more Fabry–Perot etalons, as discussed in Sect. 7.8.2.1.

For continuous laser pumping, Ar^+ lasers (and sometimes also Kr^+ lasers) are often used. To achieve a much lower threshold, as required for cw pumping, the near-longitudinal pumping configuration in Fig. 9.17 is often used. Liquid dye medium in the form of a thin jet stream (~200 μm thickness) flows freely in a plane orthogonal to the plane of the figure and inclined at Brewster's angle relative to the dye laser beam direction. Accordingly, this laser beam is linearly polarized with its electric field in the plane of the figure. Both pump and laser beams have their waist in the jet stream with similar, very small, spot sizes (~10 μm). For laser tuning, a birefringent filter can be inserted within the laser cavity. To achieve single longitudinal mode operation, a birefringent filter and generally two Fabry–Perot etalons in a unidirectional ring cavity are often used (see Fig. 7.25). For femtosecond pulse generation, a colliding pulse mode-locked (CPM) laser configuration is generally used (see

* The resolving power $\nu/\Delta\nu$, where $\Delta\nu$ is the resolved bandwidth, can be shown to just equal the number of lines of the diffraction grating illuminated by the laser beam. At grazing incidence this number increases; thus resolving power also increases.

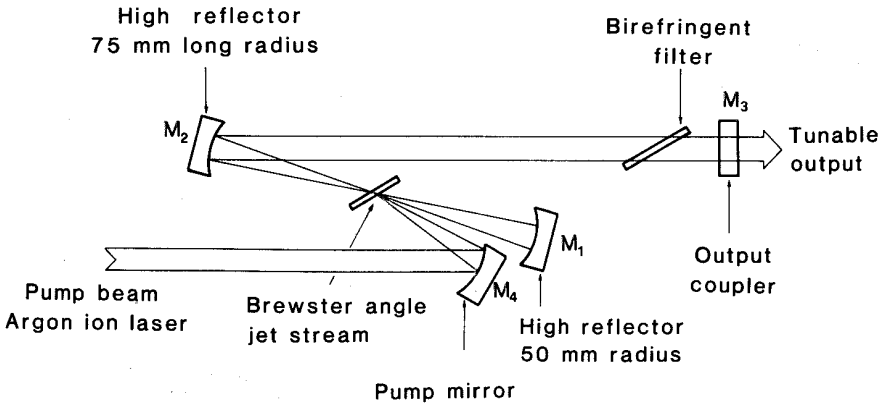

FIG. 9.17. Arrangement for an Ar ion laser-pumped cw dye laser.

Fig. 8.29). To achieve the shortest pulse duration (~25 fs in a solution of rhodamine 6G as active medium with DODCI as a saturable absorber), a prism pair is also inserted within the laser cavity for dispersion control.

By virtue of their wavelength tunability, wide spectral coverage, and the possibility of generating femtosecond laser pulses, organic dye lasers play an important role in many fields. In particular, these lasers are widely used in scientific applications, as either a narrow band, single-mode, tunable source of radiation for high-resolution frequency-domain spectroscopy or as femtosecond pulse generators for high-resolution time-domain investigations. Other applications include the biomedical field (e.g., treating diabetic retinopathy or several dermatological diseases) and laser photochemistry. In particular, repetitively pulsed dye laser systems with many dye lasers, each transversely pumped by a copper vapor laser of ~100 W average power, have been used for laser isotope separation of ^{235}U.

9.4. SEMICONDUCTOR LASERS

Semiconductor lasers represent one of the most important class of lasers in use today, not only because of the large variety of direct applications in which they are involved, but also because they have found a widespread use as pumps for solid-state lasers.[31,32] These lasers will therefore be considered at some length here.

For the active medium, semiconductor lasers require a direct-gap material, so normal elemental semiconductors (e.g., Si or Ge) cannot be used. The majority of semiconductor laser materials are based on a combination of elements in the third group of the Periodic Table (such as Al, Ga, In) and the fifth group (such as N, P, As, Sb) hence referred to as *III–V compounds*. Examples include the well-known GaAs, as well as some ternary (e.g., AlGaAs, InGaAs) and quaternary (e.g., InGaAsP) alloys. The cw laser emission wavelength of these III–V compounds generally ranges from 630–1600 nm. Quite recently, InGaN semiconductor lasers providing cw room-temperature emission in the blue (~410 nm) have been developed; these promise to become the best candidates for semiconductor laser emission in the very important blue-green spectral region. Semiconductor laser materials are not limited to III–V compounds, however. For the blue-green region of the spectrum, we mention the wide-gap semiconductors using a combination between elements of the second group (such as Cd and Zn) and of the sixth group (S, Se) (*II–VI compounds*). For the other end of the e.m. spectrum, we mention semiconductors based on some *IV–VI compounds* such as Pb salts of S, Se, and Te, all oscillating in the mid-infrared (4–29 μm). Due to the small band gap, these last lasers require cryogenic temperatures, however. In the same wavelength range, we thus mention the recent invention of the *quantum cascade* laser,[56] which promises efficient mid-infrared sources without requiring cryogenic temperatures.

9.4.1. Principle of Semiconductor Laser Operation

The operating principle of a semiconductor laser can be explained with the help of Fig. 9.18, which shows the semiconductor valence band V and conduction band C separated by the energy gap E_g. For simplicity we first assume that the semiconductor is held at $T=0$ K. For a nondegenerate semiconductor, the valence band is completely filled with electrons

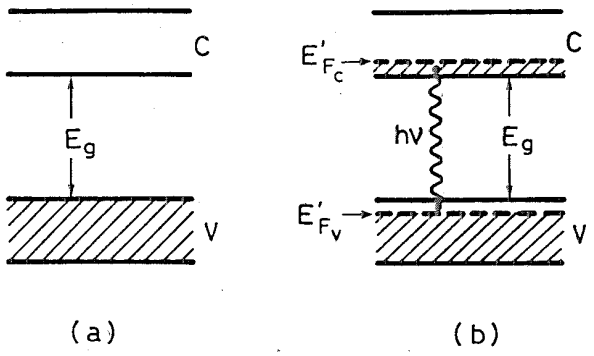

FIG. 9.18. Operation principle of a semiconductor laser.

while the conduction band is completely empty (see Fig. 9.18a; energy states belonging to the hatched area are completely filled by electrons). Suppose now that some electrons are raised from the valence band to the conduction band by a suitable pumping mechanism. After a very short time ($\sim$1 ps), electrons in the conduction band drop to the lowest unoccupied levels of this band; meanwhile any electron near the top of the valence band also drops to the lowest unoccupied levels of this band, thus leaving holes at the top of the valence band (Fig. 9.18b). This situation is described by introducing the quasi-Fermi levels E'_{F_c} for the conduction band and E'_{F_v} for the valence band (see Sect. 3.2.3). For each band, at $T=0$ K, they define the energy below which states are fully occupied by electrons and above which states are empty. Light emission can now occur when an electron in the conduction band falls to the valence band to recombine with a hole. This so-called recombination radiation is the process by which radiation is emitted in light-emitting diodes (LED). Given appropriate, conditions, however, stimulated emission from this recombination radiation, leading to laser action, can occur. In Sect. 3.2.5 we showed that the condition for a photon to be amplified rather than absorbed by the semiconductor is simply given by [see Eq. (3.2.39)]:

$$E_g \leq h\nu \leq E'_{F_c} - E'_{F_v} \tag{9.4.1}$$

In the simple case when $T=0$ K, this condition is readily understood from Fig. 9.18b, since the nonhatched area in the valence band corresponds to empty states, and a conduction band electron can fall only into an empty state in the valence band. However, the detailed treatment of Sect. 3.2.5 shows that Eq. (9.4.1) holds in fact for any temperature, so that, for the range of transition energy $h\nu$ defined by Eq. (9.4.1), gain from stimulated emission exceeds absorption. To achieve the conditon set by Eq. (9.4.1), one must have $E'_{F_c} - E'_{F_v} \geq E_g$. Values for both E'_{F_c} and E'_{F_v} depend on the intensity of the pumping process, i.e., on the density N of electrons raised to the conduction band (see Fig. 3.15). Actually $E'_{F_c} = E'_{F_c}(N)$ increases while $E'_{F_v} = E'_{F_v}(N)$ decreases as N is increased. Thus, to obtain $E'_{F_c} - E'_{F_v} > E_g$, i.e., gain exceeding absorption losses, the electron density N must exceed some critical value established by the condition:

$$E'_{F_c}(N) - E'_{F_v}(N) = E_g \tag{9.4.2}$$

* Equation (9.4.2) is thus equivalent to the condition $N_2 = N_1$ under which a nondegenerate two-level system becomes transparent.

The value of the injected carrier density that satisfies Eq. (9.4.2) is referred to as the carrier density at transparency,* N_{tr}. If the injected carrier density is now larger than N_{tr}, the semiconductor exhibits a net gain; if this active medium is then placed in a suitable cavity, laser action occurs when this net gain suffices to overcome cavity losses. Thus, to obtain laser action, injected carriers must reach some threshold value N_{th} larger than N_{tr} by a sufficient margin to allow net gain to overcome cavity losses.

Semiconductor laser pumping can in principle be achieved and indeed has been achieved in a number of ways, e.g., by using either the beam of another laser or an auxiliary electron beam to excite, transversely or longitudinally, the bulk semiconductor. By far the most convenient way of excitation, however, involves using the semiconductor laser in the form of a diode, with excitation produced by current flowing in the forward direction of the junction.[33]

Laser action in a semiconductor was in fact first observed in 1962 by using a *p-n* junction diode; the observation was made almost simultaneously by four groups,[34–37] three of which were using GaAs. Devices developed during the early stage of semiconductor laser research used the same material for both the *p* and *n* sides of the junction; therefore these are referred to as homojunction lasers. The homojunction laser is now only of historic importance, since it was superseded by the double-heterostructure (DH) laser, whose active medium is sandwiched between *p* and *n* materials that differ from the active material. Homojunction lasers in fact operate cw only at cryogenic temperatures ($T=77$ K); only after the invention of the heterojunction laser was it possible to operate semiconductor lasers cw at room temperature. This development occurred 7 years after the invention of the homojunction laser (1969),[38–40] opening the way to the great variety of applications in which semiconductor lasers are nowadays used. Homojunction semiconductor lasers are, nevertheless, discussed briefly in Sect. 9.4.2, since this discussion helps understanding the great advantages offered by DH lasers.

9.4.2. Homojunction Lasers

In the homojunction laser, the pumping process is achieved in a *p-n* junction where both *p*-type and *n*-type regions, of the same material (e.g., GaAs), are in the form of a degenerate semiconductor. Thus donor and acceptor concentrations are so large ($\approx 10^{18}$ atoms/cm^3) that the Fermi level falls in the valence band for the *p*-type, E_{F_p}, and in the conduction band for the *n*-type, E_{F_n}. If no voltage is applied to the *p-n* junction,

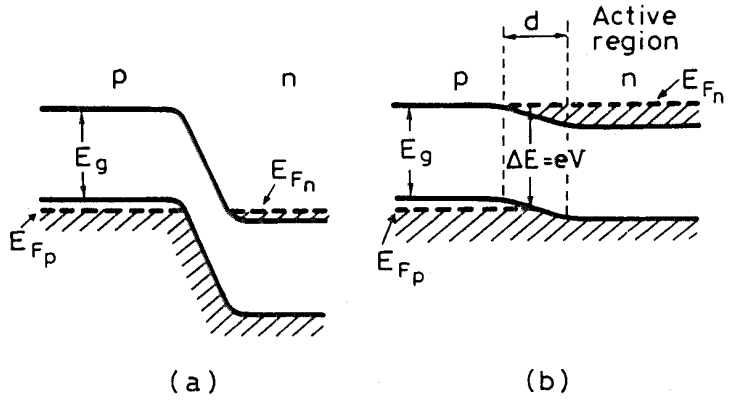

FIG. 9.19. (a) Band structure of a *p-n* junction semiconductor laser with zero voltage, and (b) forward voltage applied to the junction.

the band structure is as shown in Fig. 9.19a, where the two Fermi energies are aligned. Figure 9.19b shows the band structure when a forward-bias voltage V is applied; the two Fermi levels are separated now by $\Delta E = eV$. We see from this figure that, in the junction region, electrons are injected into the conduction band (from the n-type region) while holes are injected into the valence band (from the p-type region). Thus, for appropriate values of the current density, the transparency condition and then the laser threshold condition can be reached. One of the main limitations of this device comes from the very small potential barrier that an electron in the conduction band encounters when it reaches the p-side of the junction. The electron can then penetrate into the p-type material, where it becomes a minority carrier, thus recombining with a hole. The penetration depth d of the electron is then given (according to diffusion theory) by $d = (\sqrt{D\tau})$, where D is the diffusion coefficient and τ is the electron lifetime, as established by electron-hole recombination. In GaAs, one has $D = 10\ \text{cm}^2/\text{s}$ and $\tau \cong 3$ ns, so that $d \approx 1\ \mu$m; this shows that the active region is quite thick, being limited by the diffusion length d rather than the thickness of the depletion layer ($\approx 0.1\ \mu$m).

Figure 9.20 shows a typical configuration of a p-n junction laser; the shaded region corresponds to the active layer. Note that the diode dimensions are very small (some hundreds of microns). To provide feedback for laser action, two parallel end faces are prepared, usually by cleavage, along crystal planes. Often these two surfaces are not provided with reflective coatings; in fact, since the refractive index of a semiconductor is very large (e.g., $n = 3.6$ for GaAs), there is already a sufficiently high reflectivity ($\sim 32\%$ for GaAs) from the Fresnel reflection at the semiconductor-air interface. As mentioned earlier, the thickness of the active region in the direction perpendicular to the junction is $d \approx 1\ \mu$m. Because of diffraction, however, the transverse dimension of the laser beam in this direction ($\approx 5\ \mu$m) is significantly larger than the active region.

A homojunction laser has a very high threshold current density at room temperature ($J_{th} \cong 10^5\ \text{A/cm}^2$) that prevents the laser from operating as cw at room temperature (without suffering destruction in a very short time). There are two main reasons for this high threshold: (1) The thickness of the active region ($d \approx 1\ \mu$m) is quite large, so the threshold current, being proportional to the volume of the active medium, is proportionally high. (2) Due to its comparatively large transverse dimensions, the laser beam extends considerably into the p and n regions, where it is strongly absorbed. Given these reasons, homojunction lasers only operate cw at cryogenic temperatures (typically at liquid nitrogen temperature

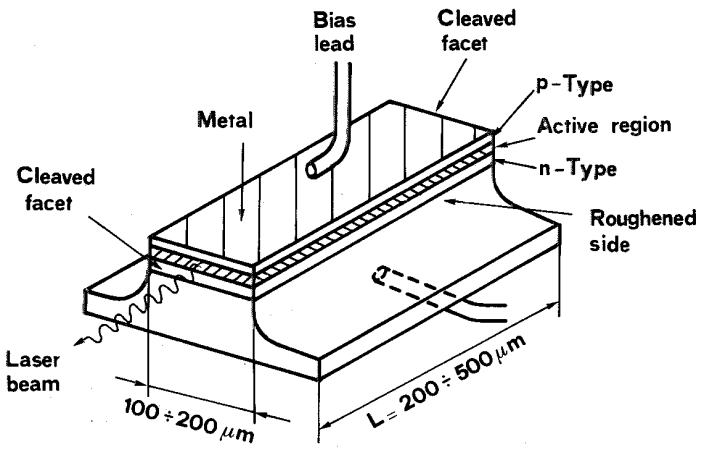

FIG. 9.20. Typical broad-area p-n homojunction laser.

$T = 77$ K). For a given laser transition, in fact, the semiconductor gain, according to Eq. (3.2.37), increases rapidly with decreasing temperature. Contact of the diode with liquid nitrogen also helps providing very efficient cooling.

9.4.3. Double-Heterostructure Lasers

The limitations discussed in Sect. 9.4.2 prevented widespread use of semiconductor lasers until first, single-heterostructure, then, immediately after, double-heterostructure lasers were introduced. We limit our discussion here to the latter structure, since it is the only one now in common use.

Figures 9.21a–b, respectively, show two examples of a double heterostructure, where the active medium is a thin layer (0.1–0.2 μm) of either GaAs or the quaternary alloy InGaAsP. For the two cases considered, p and n sides are made of $Al_{0.3}Ga_{0.7}As$ and InP, respectively. When properly optimized (see Fig. 9.23), the room temperature threshold current density of such a diode structure can be reduced by about two orders of magnitude (i.e., to $\sim 10^3$ A/cm^2) compared to the corresponding homojunction devices, thus making cw room temperature operation feasible. This strong reduction in threshold current density is due to the combined effect of the following three circumstances: (1) The refractive index of the active layer n_1 (e.g., $n_1 = 3.6$ for GaAs) is significantly larger than that, n_2, of the p-side and n-side cladding-layers (e.g., $n_2 = 3.4$ for $Al_{0.3}Ga_{0.7}As$), thus providing a guiding structure (see Fig. 9.22a). This means that the laser beam is now primarily confined to the active layer region, i.e., where the gain exists (*photon confinement*; see Fig. 9.22b). (2) The band gap E_{g_1} of the active layer (e.g., $E_{g_1} \cong 1.5$ eV in GaAs) is significantly smaller than that, E_{g_2} of the cladding layers (e.g., $E_{g_2} \cong 1.8$ eV for $Al_{0.3}Ga_{0.7}As$).* Thus energy barriers form at the two junction planes, thereby effectively confining injected holes and electrons within the active layer (*carrier confinement*; see Fig. 9.22c). For a given current density, hole and electron concentration in the active layer increases, so gain increases. (3) Since E_{g_2} is appreciably larger than E_{g_1}, the laser beam, which has a frequency of $\nu \cong E_{g_1}/h$, is much less strongly absorbed in its wings (see Fig. 9.22b) by the cladding layers; the loss arises in this case only from free carriers (*reduced absorption*).

To form a double heterostructure, thus taking advantage of all its favorable properties, a very important requirement must be fulfilled, namely, the lattice period of the active layer must equal (within $\sim 0.1\%$) that of the cladding layers.† In fact, if this condition is not

* It is a general rule for all III–V compounds that any change in composition producing a change in a given sense, e.g., a *decrease*, in band gap also produces a change in the opposite sense, i.e., an *increase*, in the refractive index.

† All III–V compounds crystallize in the cubic structure.

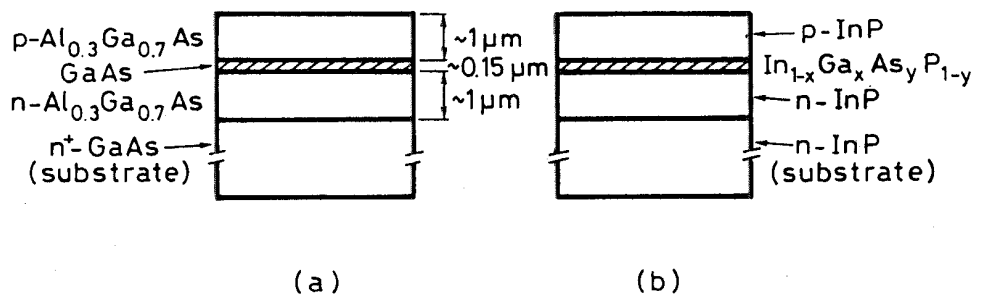

FIG. 9.21. Schematic diagram of a double-heterostructure where the active medium (*hatched area*) consists of (a) GaAs and (b) InGaAsP.

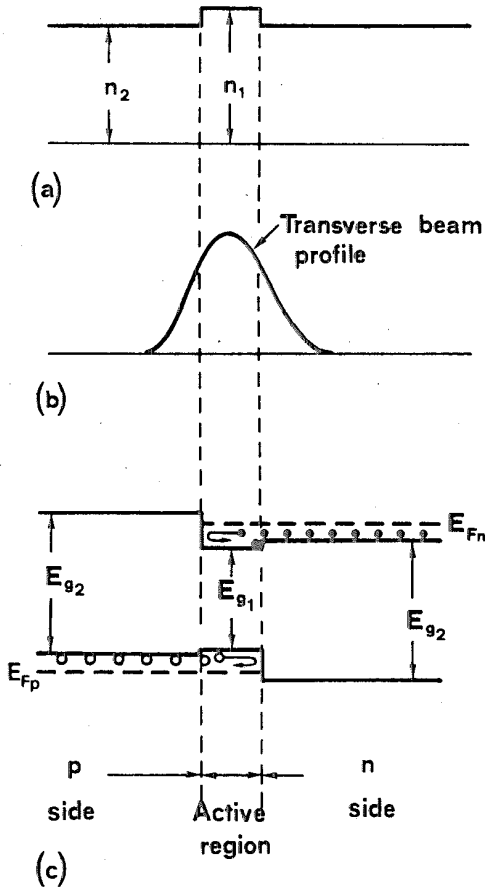

FIG. 9.22. (a) Refractive index profile, (b) transverse beam profile, and (c) band structure (very schematic) of a double-heterostructure diode laser.

fulfilled, the resulting strain at the two interfaces results in misfit dislocations; each dislocation then acts as a rather effective center for electron-hole nonradiative recombination. For the GaAs/AlGaAs structure, the lattice-matching requirement does not constitute a limitation because the lattice periods of GaAs (564 pm) and AlAs (566 pm) are very close in value. (Atomic radii of Ga and Al are in fact almost the same.)

For the quaternary compound $In_{1-x}Ga_xAs_yP_{1-y}$, the alloy can be lattice-matched to InP for a specific y/x ratio, as the following argument shows: Suppose that, starting with InP for the active layer, some fraction x of Ga is added, replacing some In in the lattice (which hence becomes In_{1-x}). Since the Ga radius is *smaller* (by ~ 19 pm) than that of In, the lattice period of the $In_{1-x}Ga_xP$ decreases compared to InP. Suppose now that some fraction y of As (As_y) replaces P (thus becoming P_{1-y}). Since the As radius is now *larger* (by ~ 10 pm) than that of P, this addition tends to increase the lattice period. Therefore, if the y/x ratio of the two substituents has an appropriate value, the two effects cancel each other, thus resulting in $In_{1-x}Ga_xAs_yP_{1-y}$ being lattice-matched to InP. This lattice-matching condition is given by $y \cong 2.2x$. Changing x, while keeping the y/x ratio equal to the lattice-matching value, changes the semiconductor band gap and hence the emission wavelength. In this way, the emission wavelength of $In_{1-x}Ga_xAs_yP_{1-y}$ can be varied from 1150 to 1670 nm for cw room temperature operation, thus encompassing the so-called second ($\sim$1300 nm) and third ($\sim$1550 nm) transmission windows of silica optical fibers.

Figure 9.23 shows experimental and theoretical plots of the threshold current density J_{th} versus thickness d of the active layer, for a DH GaAs laser.[41] Note that, as d decreases, J_{th}

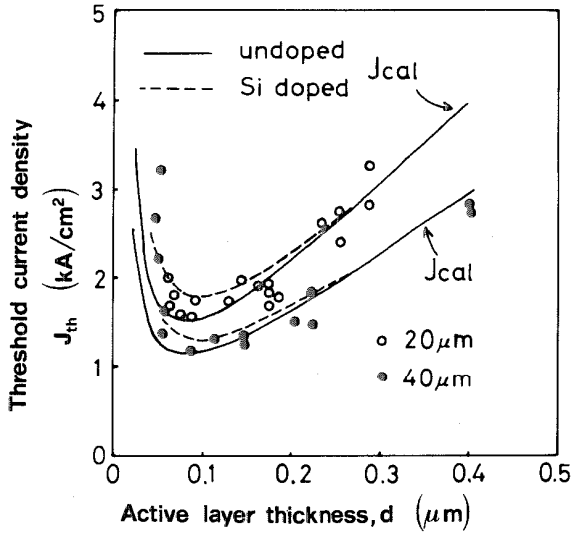

FIG. 9.23. Calculated (*continuous and dashed lines*) and experimental (*open and closed circles*) values of the threshold current density J_{th} versus active layer thickness d for a 300 μm long AlGaAs DH laser. Closed and open circles represent data for a 40-μm and 20-μm stripe width, respectively. Theoretical curves J_{cal} refer to cases of undoped and low Si-doped active layers. (By permission from Ref. 41.)

first decreases, then reaches a minimum value ($J_{th} \cong 1$ kA/cm^2 for $d \cong 0.1$ μm) and thereafter increases. To understand this behavior, we first relate the threshold current density J_{th} to the threshold carrier density N_{th}. We begin by defining R_p as the rate at which electrons (and holes) are injected, for unit volume, into the active layer. We also let η_i, usually referred to as the *internal quantum efficiency*, be the fraction of carriers that recombine radiatively in the layer; the remaining fraction undergoes nonradiative electron-hole recombination primarily at the junction boundaries. We can also view the quantity η_i as the effective fraction of injected carriers and we can consider the remaining fraction as not having been injected into the active region at all. For a given current density J flowing through the junction, R_p is then readily seen to be given by $R_p = \eta_i J/ed$, where e is the electron charge and d is the thickness of the active layer. Under steady-state conditions, a simple balance condition gives the corresponding expression for the carrier density N as $N = R_p\tau_r$, where τ_r is the radiative recombination time (given the previous assumption, all carriers recombine radiatively in the active layer). From the previous two expressions, we get $J = edN/\eta_i\tau_r$ so that at threshold:

$$J_{th} = \left(\frac{ed}{\eta_i\tau_r}\right)N_{th} \tag{9.4.3}$$

With the help of Eq. (9.4.3) we can now qualitatively understand the relevant features of Fig. 9.23. Note in fact that, for sufficiently large values of d, the threshold carrier density N_{th} is almost the same as the transparency density N_{tr} (see Example 9.1); hence it is a constant. Equation (9.4.3) then predicts a linear relation between J_{th} and d as indeed observed in Fig. 9.23 for sufficiently large values of d (larger than $\sim$0.15 μm). However, when the thickness d becomes sufficiently small, the confinement action of the active layer (see Fig. 9.22b) is no longer so effective; therefore the beam extends considerably into the p and n sides of the junction. This situation results in a reduced effective gain and, at the same time, in increased losses in the cladding layers; both effects lead to a strongly increased N_{th}. Thus, for sufficiently small values of d, J_{th} is expected to increase as d decreases.

Example 9.1. *Carrier and current densities at threshold for a DH GaAs laser.* Since the laser field is space-dependent, the threshold condition must be derived, as in previous examples (see e.g., Sect. 6.3.4), by setting the condition that spatially averaged gain must equal spatially averaged losses. Thus in general we write

$$\langle g \rangle L = \langle \alpha_a \rangle L + \langle \alpha_n \rangle L + \langle \alpha_p \rangle L + \gamma_m \tag{9.4.4}$$

where: L is the length of the active medium; g is the gain coefficient; α_a is the scattering loss of the active layer; α_n and α_p are the losses in the n and p sides of the cladding, respectively; γ_m is the mirror loss. The average values in Eq. (9.4.4) are taken over the field intensity distribution so that, for example, the average gain is given by

$$\langle g \rangle = \frac{\int_a g|u|^2 \, dV}{\int_c |u|^2 \, dV} \tag{9.4.5}$$

where $u(x, y, z)$ is the field distribution within the laser cavity, the integral of the numerator is taken over the volume of the active medium, and the integral of the denominator is taken over the whole volume of the cavity. The quantities $\langle g \rangle$ and $\langle g \rangle L$ are usually referred to as the *modal gain coefficient* and the *modal gain*, respectively. Similar expressions hold for the average values on the right-hand side of Eq. (9.4.4); the integral of the numerator is of course always taken over the volume of the material considered. For simplicity we assume that $\alpha_n \cong \alpha_p = \alpha$, and we neglect the spatial variation of the cavity field along the longitudinal z-coordinate (as produced by, e.g., a standing wave pattern) and along the coordinate parallel to the junction. Then, with the help of Eq. (9.4.5) and the corresponding expressions for $\langle \alpha_a \rangle$ and $\langle \alpha_p \rangle$, Eq. (9.4.4) readily gives

$$g\Gamma = \alpha_a \Gamma + \alpha(1 - \Gamma) + [\ln(1/R)/L] \tag{9.4.6}$$

where R is the power reflectivity of the two end mirrors (assumed to be equal for the two mirrors) and:

$$\Gamma = \frac{\int_{-d/2}^{+d/2} |u|^2 \, dx}{\int_{-\infty}^{+\infty} |u|^2 \, dx} \tag{9.4.7}$$

where x is the coordinate in the direction orthogonal to the junction. The quantity Γ represents the fraction of the beam power actually in the active layer; it is usually referred to as the *beam confinement factor*. According to the discussion in Sect. 3.2.5, we can now approximate g as $g = \sigma(N - N_{tr})$, where σ is the differential gain coefficient and N_{tr} is the carrier density at transparency. If we now further assume for simplicity $\alpha_a = \alpha$, then Eq. (9.4.6) simplifies to:

$$\sigma\Gamma(N_{th} - N_{tr}) = \alpha + \left[\frac{\ln(1/R)}{L}\right] = \frac{\gamma}{L} \tag{9.4.8}$$

where N_{th} is the threshold carrier density and $\gamma = \alpha L + \ln(1/R)$ is the total loss per pass. From Eq. (9.4.8) we finally obtain the desired expression for the threshold carrier density as:

$$N_{th} = \left(\frac{\gamma}{\sigma L \Gamma}\right) + N_{tr} \tag{9.4.9}$$

To proceed with the calculation, we must now evaluate the confinement factor Γ. A fairly accurate and simple expression is given by:[42]

$$\Gamma \cong \frac{D^2}{(2+D^2)} \tag{9.4.10}$$

where:

$$D = 2\pi(n_1^2 - n_2^2)^{1/2}\frac{d}{\lambda} \tag{9.4.11}$$

is the normalized thickness of the active layer. (Recall that n_1 and n_2 are the refractive indices of the active medium and cladding layers, respectively.) If we now take $n_1 = 3.6$, $n_2 = 3.4$, and $\lambda = 850$ nm (as appropriate for a GaAs laser) and perform the calculation for $d = 0.1$ μm, we obtain $D \cong 0.875$ and hence $\Gamma \cong 0.28$. To obtain a numerical estimate of the corresponding value of N_{th}, we take the reflectivity of the two end faces equal to that of the uncoated surfaces ($R \cong 32\%$) and assume a loss coefficient $\alpha \cong 10$ cm^{-1} and a cavity length of $L = 300$ μm. We obtain $\gamma = \ln(1/R) + \alpha L \cong 1.44$. If we now take (see Table 3.1) $\sigma = 3.6 \times 10^{-16}$ cm^2 and $N_{tr} = 2 \times 10^{18}$ carriers/cm^3, we obtain from Eq. (9.4.9):

$$N_{th} = (0.48 + 2) \times 10^{18} \text{ carriers/cm}^3 \tag{9.4.12}$$

where, for convenience, the numerical values of the two terms on the right-hand side of Eq. (9.4.9) are shown separately. Equation (9.4.12) thus shows that, in this case i.e. for relatively large values of d and hence of the confinement factor Γ, the first term (i.e., the carrier density required to overcome cavity losses) is a relatively small fraction of N_{tr}.

The threshold current density is now readily obtained by substituting Eq. (9.4.9) into Eq. (9.4.3). We obtain

$$J_{th} = \left(\frac{ed}{\eta_i \tau_r}\right)\left[\left(\frac{\gamma}{\sigma L \Gamma}\right) + N_{tr}\right] \tag{9.4.13}$$

We have seen that, for sufficiently large values of d, N_{tr} is the dominant term in the square brackets in Eq. (9.4.13). In this case J_{th} is expected to be proportional to d, as indeed shown in Fig. 9.23 for d larger than ~ 0.15 μm; most of the threshold pump current, in this case, is just used to reach the semiconductor transparency condition. When d becomes very small, however, the confinement factor also becomes very small [according to Eq. (9.4.10), for very small values of d, $\Gamma \propto d^2$]; the first term in brackets eventually dominates, so J_{th} reaches a point where it increases with decreasing d.

To obtain a numerical evaluation of J_{th} from Eq. (9.4.13), we assume $d = 0.1$ μm, we take $\eta_i \cong 1$, $\tau_r = 4$ ns and use the previously calculated value of N_{th}. We obtain $J_{th} \cong 10^3$ A/cm^2 in reasonable agreement with results in Fig. 9.23.

9.4.4. Quantum Well Lasers

If the thickness of the active layer of a DH laser is greatly reduced to a point where the dimension becomes comparable to the deBroglie wavelength, ($\lambda \cong h/p$), a QW double-heterostructure laser is produced.[43,44] Such lasers exploit the more favorable optical properties of a QW or a multiple QW (MQW) structure compared to those of the

corresponding bulk material (in particular the increased differential gain, see Example 3.12, and decreased dependence of this gain on temperature). These favorable properties are essentially related to the completely different form for the density of states of QW materials compared to bulk materials, arising from quantum confinement in the well direction (see Sect. 3.3). Single QW and also MQW lasers are however seriously affected by the strong reduction in the confinement factor arising from reduced layer thickness. To limit beam size in the QW direction, one must then use a separate confinement structure.

Figure 9.24a shows a particularly simple example of several structures introduced for this purpose. Everything in this figure is to scale except for the bulk GaAs band gap energy, which is reduced for clarity. At the center of the structure is the thin (~ 10 nm) QW (GaAs) and, on both sides of the well, are two thicker (~ 0.1-μm) inner barrier layers of wider band gap and, hence, lower refractive index material ($Al_{0.2}Ga_{0.8}As$). Outside the inner barrier layers are two much thicker (~ 1-μm) cladding layers of still wider band gap material ($Al_{0.6}Ga_{0.4}As$), constituting the p- and n-sides of the diode.

Beam confinement is established by the higher refractive index of inner barrier layers compared to cladding layers, while the contribution to confinement by the very thin QW is negligible. The resulting beam intensity profile for this waveguide configuration is also shown as a dashed line in Fig. 9.24a. The full width between the $1/e^2$ points, in this case, is confined to a comparatively small dimension (~ 0.8 μm). A somewhat similar and widely used structure is shown in Fig. 9.24b, where the index composition of the inner barrier layer ($Al_xGa_{1-x}As$) gradually changes from, e.g., $x = 0.2$ at the QW interface to the value $x = 0.6$ at the interfaces between the two cladding layers, where it matches the index of the cladding layers. This structure is usually referred to as a graded index separated confinement heterostructure (GRINSCH).

It should be noted that, in both structures in Figs. 9.24, carriers are confined by the QW structure, while the beam is confined by the step index or graded index profile in Figs. 9.24a–b, respectively. Note also that, although the thickness of the QW layers is much smaller than the width of the beam, optical confinement results in a sufficiently high confinement factor to now take advantage of the expected reduction of J_{th} due to the strong reduction in the active layer thickness d [see Eqs. (9.4.3) and (9.4.13)]. In fact, as Example 9.2 shows, we can now obtain values of J_{th}

Example 9.2. *Carrier and current densities at threshold for a GaAs/AlGaAs QW laser.* We assume that a functional relation of the form $g = \sigma(N - N_{th})$ still holds approximately for a QW,* so that relations established in Example 9.1 are still applicable. To compare this case with Example 9.1, we take the same values for the loss coefficient α (10 cm^{-1}) and mirror reflectivity R (32%), hence of the total loss γ ($\gamma = 1.44$). We also take the same value for cavity length (300 μm) and carrier density at transparency N_{tr} (2×10^{18} cm^{-3}), while we now take $\sigma \cong 6 \times 10^{-16}$ cm^2 (see Sect. 3.3.5). To calculate the confinement factor, we assume that the field profile can be written as $u \propto \exp[-(x^2/w_\perp^2)]$ where $w_\perp$ is the beam spot size in the direction orthogonal to the junction. From Eq. (9.4.7) we obtain $\Gamma = (d/0.62d_\perp)$, where d is well thickness and $d_\perp = 2w_\perp$, so that, taking $d = 10$ nm and $d_\perp = 1$ μm, we obtain $\Gamma = 1.6 \times 10^{-2}$. From Eq. (9.4.9) we now have $N_{th} = (5 + 2) \times 10^{18}$ cm^{-3}, where numerical values for the two terms on the right-hand side of Eq. (9.4.9) are again separated. We see that, due to the much smaller value for the confinement factor, the first term, i.e., the carrier density required to overcome cavity losses, is now

* This approximation holds with less accuracy for a QW; a plot of g versus N shows a curve that, due to the essentially two-dimensional structure of the density of states, saturates at sufficiently high values of current injection (see Ref. 45).

appreciably larger than the second term N_{tr}. The threshold current density is now readily obtained by substituting the previously calculated value of N_{th} into Eq. (9.4.3). Assuming again that $\eta_i = 1$ and $\tau = 4$ ns, we obtain $J_{th} \cong 280$ A/cm^2, which is about four times smaller than the value calculated for a DH laser. Note that, in this case, since cavity loss primarily determines the value of N_{th}, a reduction of this loss is helpful in further reducing J_{th}. If we now take, for example, $\alpha = 3$ cm^{-1} and $R = 80\%$, we have $\gamma = 0.28$, hence $N_{th} = (2.3 + 2) \times 10^{18}$ cm^{-3} and $J_{th} \cong 170$ A/cm^2.

~4–5 times smaller than those of a DH laser (i.e., ~200 A/cm^2). This threshold reduction thus arises from a combination of the following features: (1) Reduction in threshold as expected from the strong reduction in layer thickness once the problem of beam confinement is partially overcome by a separated confinement structure. (2) Increase (by about a factor of 2) in the differential gain, which occurs in a QW compared to the corresponding bulk material.

Separated confinement structures in Fig. 9.24 may include either a single QW, as shown in the figure, or a MQW structure; in this case the structure consists of a number of alternating layers of narrow and wide band gap materials (see Fig. 9.25). The thickness of each QW is 5 nm, while the thickness of the wide band gap barrier (4 nm) must be enough to prevent quantum tunneling of electrons from one well to the next. Compared to the case for a MQW, the threshold for a single QW tends to increase due to the decreased value of the confinement factor; it tends to decrease due to the decreased value of the effective thickness d of the active medium. For long laser cavities ($L > 300$ μm), one has $N_{th} \cong N_{tr}$; thus the second effect dominates the first one, and a single QW exhibits the lowest threshold. For shorter cavity lengths, however, the threshold of a MQW becomes smaller than that of a single QW; the optimum number of wells depends on the actual value of cavity length.[46]

We saw in Sect. 9.4.3 that, in a DH laser, a precise lattice match between the two heterostructures (within better than 0.1%) must be achieved. For the very small thickness of a QW, however, this matching condition can be considerably relaxed, so that a larger lattice mismatch between the QW and the surrounding wider gap material (up to ~1–3%) can be tolerated without creating excessive misfit dislocations at the boundaries between the two materials. Due to the lattice mismatch, a compressive or tensile strain is produced in the QW

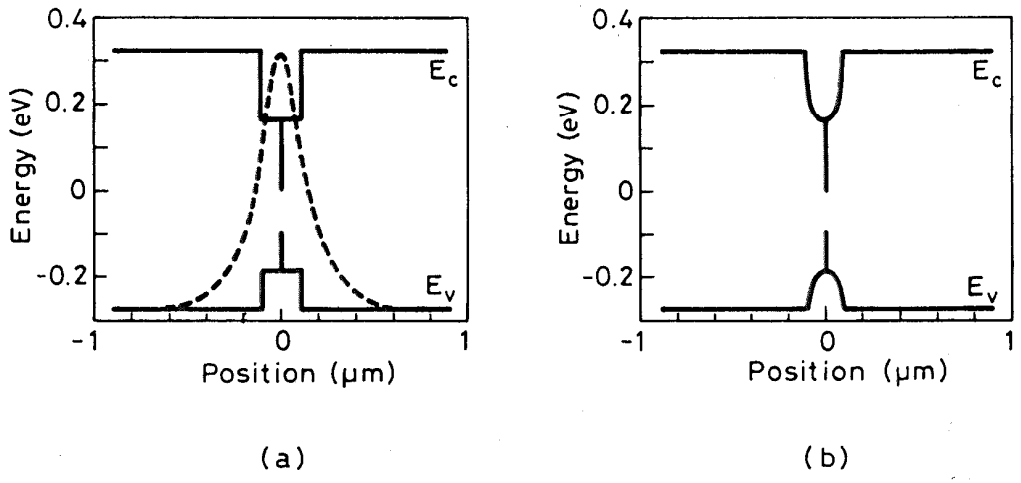

FIG. 9.24. (a) Energy bands of a step index $Al_xGa_{1-x}As$-GaAs separate confinement QW heterostructure. The resulting optical mode intensity profile for this waveguide structure is shown as a dashed line. (By permission from Ref. 43) (b) Energy bands of a graded index $Al_xGa_{1-x}As$-GaAs separate confinement QW heterostructure (GRINSCH).

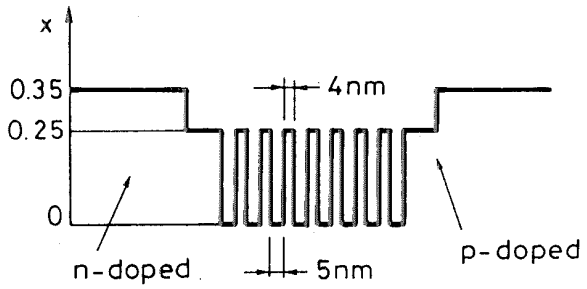

FIG. 9.25. Composition variations in $In_{0.5}Ga_{0.5}P/In_{0.5}(Ga_{0.5-x}Al_x)P$ MQW active layer, where $x = 0.25$ for well barriers and $x = 0.35$ for confinement layers, producing laser emission at 670-nm wavelength.

structure, resulting in a strained QW. Strained QWs present two main advantages: (1) Structures can be grown to produce laser action in wavelength ranges not otherwise covered (e.g., 900–1100 nm for $In_xGa_{1-x}As/GaAs$). (2) Under compressive strain, as discussed in Sect. 3.3.6, the effective mass of the hole in a direction parallel to the junction decreases to a value closer to the effective mass of the electron. This situation lowers the transparency density N_{tr} and increases the differential gain σ compared to an unstrained QW. Thus strained QW lasers allow laser action to be obtained, with very low threshold current density and high efficiency, at wavelengths not previously accessible.

9.4.5. Laser Devices and Performances

Double-heterostructure as well as QW lasers quite often use the so-called stripe geometry configuration in Fig. 9.26, where the active area (*dashed lines*) may be either a double heterostructure or a separated confinement single-QW or MQW structure. We see from both figures that, by introducing a suitable insulating oxide layer, current from the positive electrode is constrained to flow in a stripe of narrow width s ($s = 3$–10 μm). Compared to a broad area device (see Fig. 9.20), this stripe geometry device has the advantage of considerably reducing the area A ($A = Ls$, where L is the semiconductor length) through which current flows. Thus, for a given current density J, the required total current $I = JA$ is correspondingly reduced. Furthermore, since the width of the gain region in the junction plane is also roughly equal to s, this mechanism can be used to confine the beam transverse dimension in the direction parallel to the junction. The corresponding device is

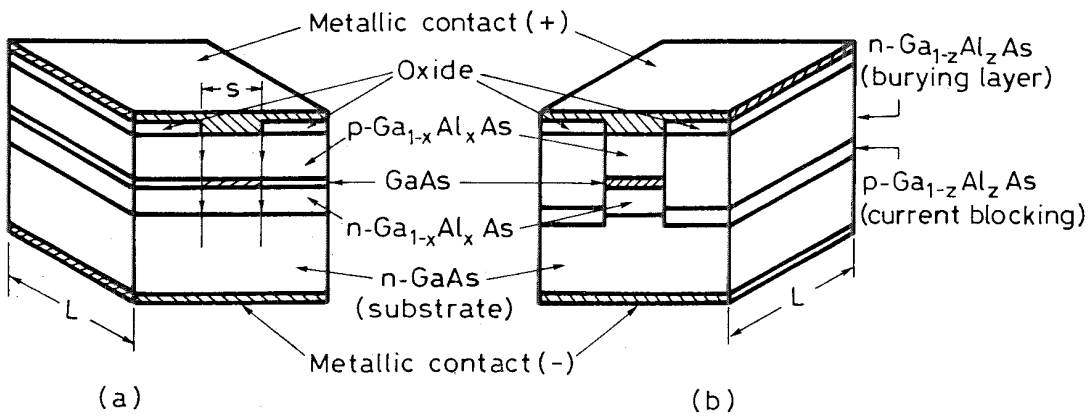

FIG. 9.26. Detail of stripe geometry double-heterostructure semiconductor lasers: (a) gain-guided laser and (b) buried heterostructure index-guided laser.

referred to as a *gain-guided laser* (see Fig. 9.26a). If s is made sufficiently small ($s < 10$ μm), gain confinement restricts the beam to the fundamental transverse mode in the direction parallel to the junction. Orthogonal to the junction, the beam is also confined to the fundamental transverse mode by the index-guiding effect produced by the double heterostructure (see Fig. 9.22) or by the separated confinement structure (see Fig. 9.24). The output beam thus consists of a single-transverse mode of elliptical cross section (~ 1 μm $\times$ 5 μm). The gain-guided structure in Fig. 9.26a has the disadvantage that unpumped regions of the active layer are strongly absorbant, so the beam confinement action from these regions inevitably introduces some loss for the beam. A better solution is to provide lateral confinement by a refractive-index-guiding action within the junction plane, as well (*index-guided lasers*). A possible solution involves surrounding the active layer with semiconductor materials of a lower refractive index, such as in the buried heterostructure laser in Fig. 9.26b. With an index-guided laser, the laser beam suffers less absorption by the laterally confining media. In fact, index-guided structures (e.g., buried or ridge waveguide structures) appear to be increasingly favored in commercial devices.

We now consider some properties of the output beam, namely, output power, beam divergence, and spectral content.

Plots of output power versus input current, at two different temperatures, for a gain-guided DH GaAs semiconductor laser are shown in Fig. 9.27. Note that the threshold current I_{th} at room temperature is less than 100 mA as a result of using the stripe geometry. Threshold currents lower than this (~ 15 mA) are now more typical for both gain-guided and index-guided DH GaAs semiconductor lasers; much lower values (~ 1 mA) are obtained with particular QW devices. [Indeed, assuming $J_{th} = 200$ A/cm^2 (see Example 9.2) $s = 4$ μm, and $L = 150$ μm, one gets $I_{th} = 1.2$ mA.] Figure 9.27 shows a rapid increase in I_{th} with temperature. In most laser diodes, this increase follows the empirical law $I_{th} \propto \exp(T/T_0)$ where T_0 is a characteristic temperature, dependent on the particular diode, whose value is a measure of the quality of the diode. The ratio between threshold values at two temperatures, differing by ΔT, is in fact given by $(I'_{th}/I''_{th}) = \exp(\Delta T/T_0)$. Thus, the

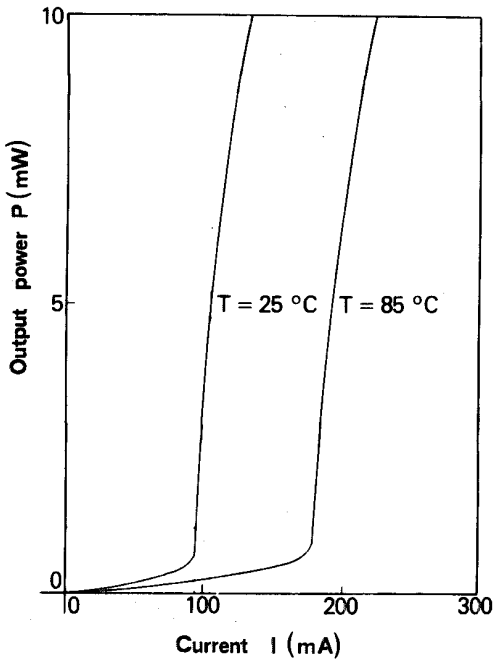

FIG. 9.27. Plot of the output power versus the input current for a DH laser at room temperature and elevated temperature.

greater T_0, the less sensitive I_{th} is to temperature. From Fig. 9.27 we can calculate that $T_0 \cong 91$ K. In DH GaAs lasers T_0 typically ranges from 100–200 K, while T_0 is usually larger (>270 K) for GaAs QW lasers. Thus the increase in the characteristic temperature of QW lasers is another advantage of QW devices; it results from a weaker dependence of quasi-Fermi energies, and hence of differential gain, on temperature (compare Fig. 3.25 and Fig. 3.15). The characteristic temperature for DH InGaAsP/InP lasers is considerably lower than the preceding values (50 K < T_0 < 70 K), probably due to the rapid increase in the nonradiative decay rate (due to Auger processes) in this narrower bandgap material (see Sect. 3.2.6). Note that the output power in Fig. 9.27 is limited to ~10 mW. Higher output powers (typically above 100 mW) can result in beam intensities high enough to damage semiconductor facets. Note also that the slope efficiency of the laser is given by $\eta_s = dP/V\,dI$, where V is the applied voltage. Taking $V \cong 1.8$ V, we obtain $\eta_s = 40\%$. Even higher slope efficiencies than this (up to about 60%) have in fact been reported. Thus semiconductor lasers are currently the most efficient lasers available.

Example 9.3. *Output power and external quantum efficiency of a semiconductor laser.* To calculate the output power, we first observe that, under steady-state conditions, the power emitted by stimulated emission can simply be written as $P_e = (I - I_{th})\eta_i h\nu/e$, where η_i is the internal quantum efficiency, introduced in Sect. 9.4.3, and ν is the frequency of the emitted radiation. Part of this power is dissipated by internal losses (due to scattering and cladding losses), and part is available as output power from the two cavity ends. This power can then be written as:

$$P = \left[\frac{(I - I_{th})\eta_i h\nu}{e}\right]\left(\frac{-\ln R}{\alpha L - \ln R}\right) \tag{9.4.14}$$

where R is the power reflectivity of the two end mirrors, α is the internal loss coefficient, and L is the cavity length. We can now define the external quantum efficiency η_{ex} as the ratio between the increase in emitted photons and the corresponding increase in injected carriers, i.e., $\eta_{ex} = d(P/h\nu)/d(I/e)$. From Eq. (9.4.14) we then obtain:

$$\eta_{ex} = \eta_{in}\left(\frac{-\ln R}{\alpha L - \ln R}\right) \tag{9.4.15}$$

This shows that η_{ex} increases by reducing the cavity length. Note also that, according to previous definitions, the relation between external efficiency and slope efficiency is simply $\eta_{ex} = \eta_s(eV/h\nu)$.

Concerning the divergence properties of the output beam, we observe that, due to the small beam dimension in the direction orthogonal to the junction (~1 μm), the beam is always diffraction-limited in the plane orthogonal to the junction. Furthermore, as already discussed, if the width of the stripe is smaller than some critical value (~10 μm), the beam is also diffraction-limited in the plane parallel to the junction. Now let $d_\perp$ and $d_\parallel$ be the beam dimensions (full width between $1/e$ points of the electric field) in the two directions and let us assume a Gaussian field distribution in both transverse directions. According to Eq. (4.7.19), beam divergences, $\theta_\parallel$ in the plane parallel to the junction and $\theta_\perp$ in the plane orthogonal to the junction, are given by $\theta_\parallel = 2\lambda/\pi d_\parallel$ and $\theta_\perp = 2\lambda/\pi d_\perp$, respectively. For an output beam with an elliptical cross section (e.g., 1 μm × 5 μm), the divergence in the plane orthogonal to the junction is thus larger than that in the plane parallel to the junction. Then the beam ellipticity rotates by 90° at a distance some tens of microns away from the semiconductor exit face (see Fig. 6.9a). As discussed in Sect. 6.3.2.1, optical systems can be developed to compensate for this astigmatic behavior of the beam.

A typical emission spectrum for a diode laser, in which optical feedback is provided by the two end face reflections, is shown in Fig. 9.28. The equally spaced peaks correspond to different longitudinal modes of the Fabry–Perot cavity. Note two points from this figure: (1) The relative spectral bandwidth $\Delta\nu_L/\nu$ is sufficiently small ($\sim 1.1 \times 10^{-3}$) to justify stating, according to Eq. (9.4.1), that emission frequency is roughly equal to E_g/h. (2) The absolute value of this bandwidth ($\Delta\nu_L \cong 400$ GHz in Fig. 9.28) is sufficiently large, however, to be a problem for optical fiber communications, due to the chromatic dispersion of an optical fiber particularly around $\lambda = 1550$ nm. To obtain much smaller linewidths, the best approach is to use either a distributed feedback (DFB) laser or a laser with distributed Bragg reflectors (DBRs). These lasers are briefly considered in the next section.

9.4.6. Distributed Feedback and Distributed Bragg Reflector Lasers

A distributed feedback laser consists of an active medium in which a periodic thickness variation is produced in one of the cladding layers forming part of the heterostructure.[47] Figure 9.29a shows a schematic of a DFB laser oscillating at 1550 nm, where an InGaAsP active layer ($\lambda = 1550$ nm) is sandwiched between two InGaAsP cladding layers ($\lambda = 1300$ nm); one of the two layers shows this periodic thickness variation. Since the refractive index of the InGaAsP cladding layers is larger than that of the InP p- and n-type layers, the electric field of the oscillating mode will see an effective refractive index $n_{eff}(z) = \langle n(x, z)\rangle_x$ that depends on the longitudinal z-coordinate. In the previous expression $\langle\ \rangle_x$ stands for a weighted spatial average taken over the x-coordinate, orthogonal to the junction; the weight is determined by the transverse distribution of the beam intensity $|u(x)|^2$ [see also Eq. (9.4.5)]. We now assume that $n_{eff}(z)$ is a periodic function of z, i.e.:

$$n_{eff}(z) = n_0 + n_1 \sin[(2\pi z/\Lambda) + \varphi] \tag{9.4.16}$$

where Λ is the pitch of the periodic thickness change (see Fig. 9.29a). In accordance with Bragg's ideas about scattering from a periodic array of elements, the forward- and backward-propagating beams of the DFB laser are effectively coupled to each other if the free space wavelength of the radiation is such that

$$\lambda = \lambda_B = 2\langle n_{eff}\rangle\Lambda \tag{9.4.17}$$

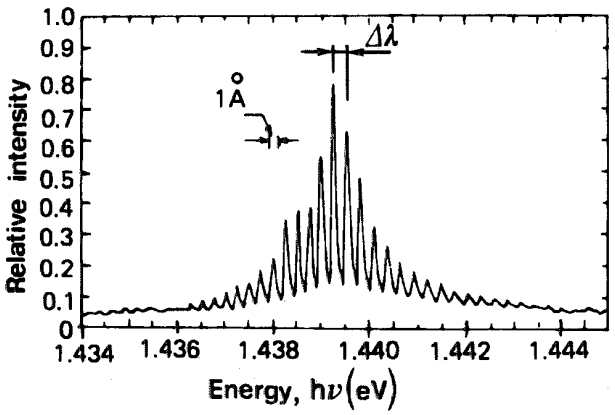

FIG. 9.28. Typical spectral emission of a Fabry–Perot-type DH GaAs semiconductor laser with a cavity length of 250 μm.

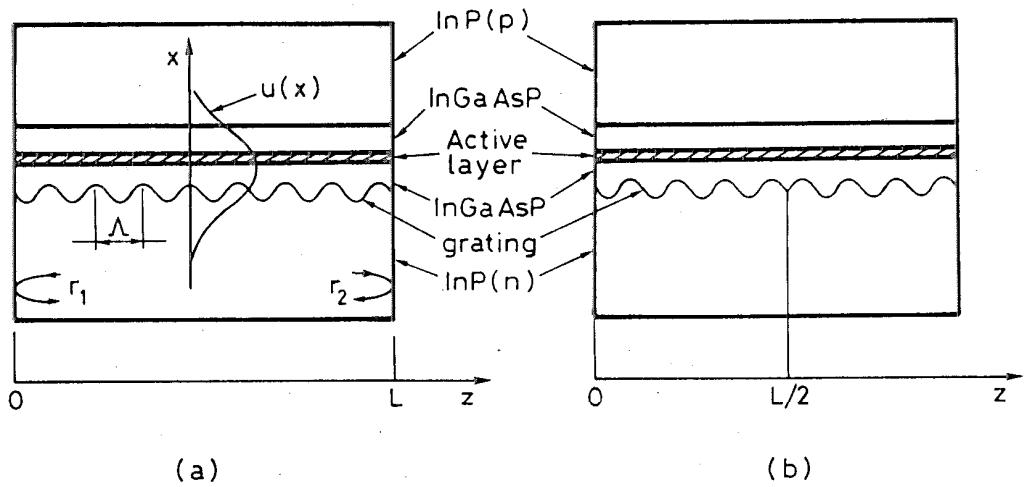

FIG. 9.29. Schematic structure of (a) DFB laser with a uniform grating and (b) $\lambda/4$-shifted DFB laser.

where $\langle n_{eff} \rangle$ is some suitable average value, along the z-coordinate, of n_{eff}, whose value is discussed later. To appreciate the significance of Eq. (9.4.17), we assume that $n_{eff}(z)$ consists of a periodic square-wave function of period Λ. In this case the structure in Fig. 9.29a is equivalent to a periodic sequence of high and low refractive index layers; the thickness of each layer equals $\Lambda/2$. This case is thus rather similar to a periodic sequence of multilayer dielectric mirrors (see Sect. 4.4) and constructive reflection is expected to occur when $(\langle n_{eff} \rangle \Lambda/2) = \lambda/4$. Equation (9.4.17) shows that, for a given pitch Λ, there is only one wavelength, i.e., only one mode satisfying the Bragg condition. Only this mode is expected to oscillate when the appropriate threshold condition is satisfied.

The preceding simple considerations are very approximate and a more precise description of DFB laser behavior would require a detailed analytic treatment. In this analysis, the two oppositely traveling waves are assumed to have an effective gain coefficient, as established by the active medium, and to be coupled by a periodic change in the dielectric constant, i.e., of the refractive index. One also generally assumes some finite values r_1 and r_2 of the electric field reflectivity from the two end faces. We do not go into this analysis here, referring the reader elsewhere for a detailed treatment,[47,48] but discuss only a few important results.

First we consider a rather peculiar result, indicated for the simple case $r_1 = r_2 = 0$ in Fig. 9.30a. There the intensity transmittance T, $T = |E_f(0, L)/E_f(0, 0)|^2$ for, e.g., the forward beam, is plotted against normalized detuning $\delta L = (\beta - \beta_B)L$. In the preceding expressions $E_f(x, z)$ is the electric field of the forward beam, L is the cavity length, $\beta = 2\pi n_0/\lambda$ and $\beta_B = \pi/\Lambda$. The plots shown in the figure are obtained for the value $kL = 2$ of the normalized coupling coefficient k ($k \cong 2\pi n_1/\lambda$) and for several values of the effective gain $\langle g \rangle L$.[49] Figure 9.30a shows that a transmission minimum actually occurs at exact resonance ($\delta = 0$) while several transmission maxima, i.e., several modes, are present, symmetrically located at both sides of exact resonance. Figure 9.31a illustrates the reason for the existence of the first and strongest two resonances; in fact this figure shows the longitudinal variation of the refractive index, the standing wave patterns of the two modes, and the corresponding resonant wavelengths.[49] The mode labeled +1 is then seen to be subjected to an effective, i.e., longitudinally averaged refractive index, $\langle n_{eff} \rangle_1$, that is slightly smaller than that, $\langle n_{eff} \rangle_{-1}$, of mode -1. In both preceding expressions, the spatial average $\langle\ \rangle$ is taken over the longitudinal intensity distribution of the cavity mode. According to the general Bragg

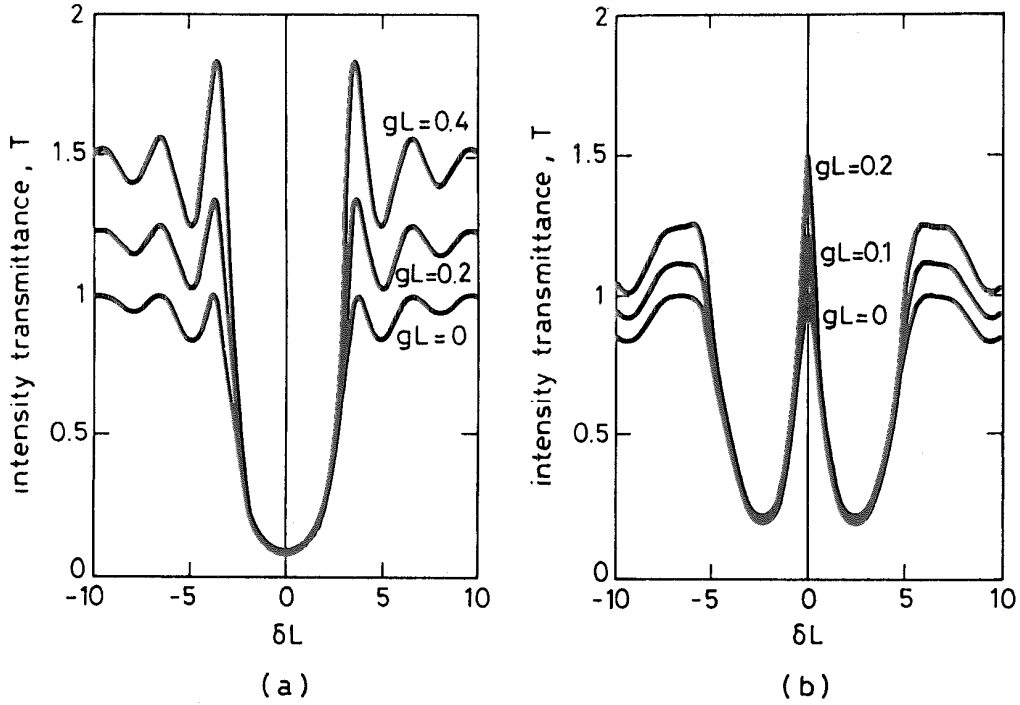

FIG. 9.30. Transmittance T versus normalized detuning δL at several values of the gain gL for zero end face reflectivity and (a) uniform grating, (b) $\lambda/4$-shifted grating. (By permission from Ref. 49.)

condition (9.4.17), the resonant wavelengths of $+1$ and -1 modes are then expected to be slightly smaller and slightly larger than the resonance value $\lambda_B = 2n_0\Lambda$, respectively.

The symmetric situation for DFB modes shown in Fig. 9.30a is obviously not desirable, and several solutions have been considered to ensure that one mode prevails. A commonly used solution makes the device asymmetric by providing end mirror reflectivities, r_1 and r_2, of different values. The best solution, however, appears to be the so-called $\lambda/4$-shifted DFB laser.[50] In this case, the periodic variation in thickness of the inner cladding layer undergoes a shift of $\Lambda/4$ at the center of the active layer (i.e., at $z = L/2$; see Fig. 9.29b). The intensity transmittance T, versus normalized detuning δL, then shows the behavior indicated in Fig. 9.30b, where several plots are made for different values of the gain $\langle g \rangle L$ and for a given value of the normalized coupling constant kL ($kL = 2$). A peak transmission, at exact Bragg resonance $\lambda = \lambda_B$, now occurs. As a further advantage, the difference in transmission between this mode and the two neighboring modes, i.e., mode selectivity, is higher in this case than in the previously considered case of a uniform grating (compare with Fig. 9.30a). The reason for the existence of only one low-loss mode can be understood from Fig. 9.31b, where, due to the $\lambda/4$-shift of the variation in layer thickness, the effective value of the refractive index $n_{eff} = \langle n \rangle_x$ is seen to show a similar shift in its longitudinal variation. The standing wave pattern of the lowest-loss mode is also shown in the figure and the longitudinal spatial average of the effective refractive index $\langle n_{eff} \rangle$ is now seen to equal n_0. The resonance condition is then $(\lambda/2n_0) = \Lambda$, and the wavelength λ of the mode coincides with the Bragg wavelength $\lambda_B = 2n_0\Lambda$.

The fabrication of uniform-grating devices and, even more so, of $\lambda/4$-shifted DFB lasers presents challenging technological problems. In fact, the pitch of the grating Λ typically has to be of submicron dimension [e.g., for a 1550 nm InGaAsP laser, $\langle n_{eff} \rangle \cong 3.4$; from Eq. (9.4.17), $\Lambda \cong 0.23$ μm]. It is therefore difficult to make this pitch uniform along the length of the grating and also constant from one grating to the next.

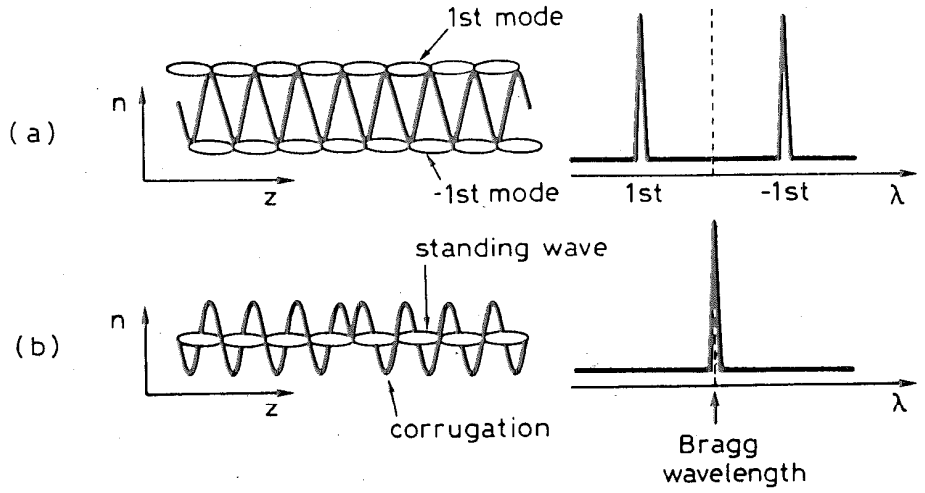

FIG. 9.31. Schematic representation of the refractive index change, mode patterns, and corresponding resonance wavelengths for a DFB laser with a uniform grating and for a DFB laser with a $\lambda/4$-shifted grating. (By permission from Ref. 49.)

In addition to using a DFB laser, another way of ensuring semiconductor laser oscillation on a single line involves the structure shown in Fig. 9.32. In this figure the two cavity ends are made of passive sections where, by appropriate corrugation of a suitable layer, the effective refractive index is modulated with a period Λ in the longitudinal direction. Reflectivity of the two end sections then arises from the constructive interference that occurs in the two sections under the Bragg condition. Since the effect of these sections is somewhat similar to that of a $(\lambda/4)$ multilayer dielectric mirror, maximum reflectivity is expected to occur at the wavelength $\lambda = 2\langle n_{eff}\rangle\Lambda$. Compared to DFB lasers, DBR lasers have the advantage that the grating is fabricated in an area separated from the active layer. This simplifies the fabrication process and makes the DBR structure more suitable for integration with other devices, such as separated sections for laser tuning or modulation. The wavelength selectivity of a DBR laser is, however, less than that of a DFB laser, due to the presence of many Fabry–Perot longitudinal modes, as established by the given length of the active medium. Actually, due to the small value of this length, only one mode usually falls within the high-reflectivity bandwidth of the DBR structure. Temperature variations can, however, produce jumping between adjacent modes and, for this reason, DBR lasers are much less widely used than DFB lasers.

9.4.7. Vertical-Cavity Surface-Emitting Lasers

So far, we have considered semiconductor diode lasers that generate light traveling in a direction parallel to the junction plane and hence emitted from one edge of the device (*edge-emitting lasers*). For several applications that will be discussed in Sect. 9.4.8, semiconductor

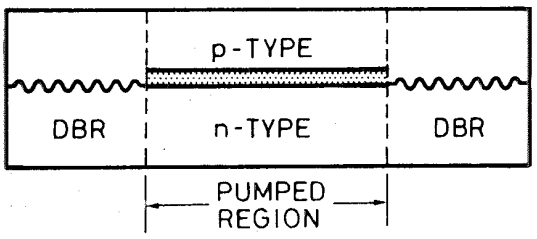

FIG. 9.32. Schematic representation of a DBR semiconductor laser.

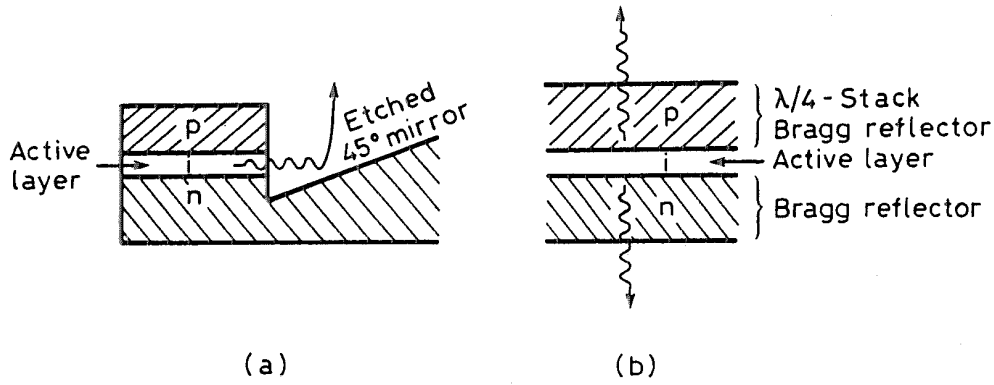

FIG. 9.33. Schematic representation of (a) a surface-emitting laser where the light of an edge-emitting laser is deflected vertically by a 45° mirror and (b) a VCSEL.

lasers emitting normal to the junction plane have been developed. These devices are usually referred to as *surface-emitting lasers*, and are made using one of the following approaches: (1) Use of a conventional edge-emitting geometry where some optical element, e.g., a 45° mirror, deflects the output beam vertically (Fig. 9.33a) (2) Use of highly reflective mirrors to clad the active layer, thus resulting in a vertical cavity that produces an output beam propagating normal to the junction plane (vertical-cavity surface-emitting laser, VCSEL, see Fig. 9.33b). Surface-emitting lasers of the type shown in Fig. 9.33a are not different, conceptually, from a conventional edge-emitting laser. A peculiar characteristic of a VCSEL, on the other hand, is the very short length of the active medium and thus the very small gain involved. However, once this low-gain limitation is overcome by using sufficiently high-reflectivity mirrors, low thresholds can be obtained. These lasers then present some distinct advantages over the corresponding edge-emitting devices, due to the inherently high-packaging density and low-threshold currents that can be achieved. In the discussion that follows, we therefore concentrate on vertical-cavity surface-emitting lasers.[51]

Figure 9.34 shows a schematic view of a VCSEL using three $In_{0.2}Ga_{0.8}As/GaAs$-strained QW layers, each 8 nm thick, as an active medium. The three active layers are sandwiched between two $Ga_{0.5}Al_{0.5}As$ spacers to form an overall thickness of one wavelength. The bottom and top mirrors are then made of a 20.5 pairs of *n*-doped and 16 pairs of *p*-doped quarter-wave GaAs/AlAs stacks, respectively. Due to the relatively high refractive-index change between the two layers (the refractive index is 3.6 for GaAs and 2.9 for AlAs), high reflectivity (~99%) can be achieved for both end mirrors. Due to the short

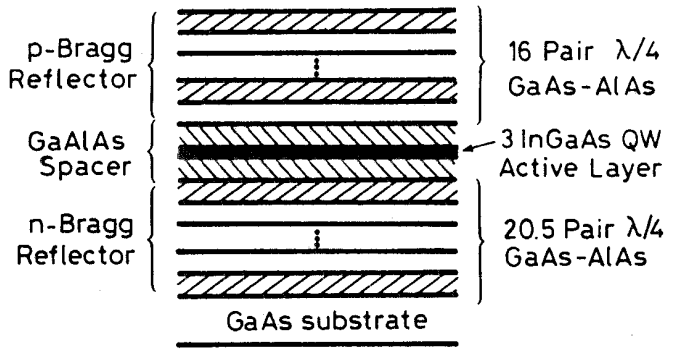

FIG. 9.34. Schematic representation of a bottom-emitting VCSEL design. The top-most GaAs layer is a half-wavelength thick to provide phase matching for the metal contact. (By permission from Ref. 52.)

length of the cavity, scattering and absorption losses in the active layer are very small, so reasonably low threshold-current densities can be obtained ($J_{th} \cong 4$ kA/cm^2). Since the diameter of the circular surface through which current flows is usually made very small ($D = 5$–10 μm), a very low threshold current is obtained (~ 1 mA). Due to this small cross-sectional area of the active region, VCSELs tend to oscillate on a TEM_{00} mode even at currents well above (e.g., twice) the threshold value. Note that, due to the small length of the laser cavity (1–2 μm), consecutive longitudinal modes are widely spaced in wavelength ($\Delta\lambda \cong 100$ nm). Thus, if one mode coincides with the peak reflectivity of each of the quarter-wave stacks, the two adjacent modes fall outside the high-reflectivity band of the mirrors and single-longitudinal-mode oscillation is also obtained.

Fabrication of VCSELs presents some technological difficulties, one of which is making the cavity length so that one longitudinal mode falls exactly at the center of the high-reflectivity band of the mirrors. Once this difficulty, and that related to fabricating so many layers of exactly $\lambda/4$-thickness, are solved, a low threshold can be achieved. If cavity losses are minimized, the slope efficiency of a VCSEL can be as high as that of an edge-emitting device; slope efficiencies up to 50% have, in fact, been demonstrated. The output power emitted by a single VCSEL is rather limited (~ 1 mW) to avoid the onset of thermal problems due to injecting high pump powers into such a small volume of active layer. Arrays of, e.g., 8×8, independently addressable, lasers as well as matrix-addressable arrays have been made.

Example 9.4. *Threshold carrier density and threshold current for a VCSEL.* According to Eq. (9.4.9), assuming a confinement factor $\Gamma \cong 1$, we can write $N_{th} = (\gamma/\sigma l) + N_{tr}$, where l is the thickness of the active layer. Following Example 9.2, we assume the values $N_{tr} = 2 \times 10^{18}$ cm^{-3} and $\sigma \cong 6 \times 10^{-16}$ cm^2 for the transparency carrier density and the differential gain of the strained layer QWs, respectively. The single-pass loss is then given by $\gamma = -\ln R + \alpha_i L$, where R is the power reflectivity of each of the two mirrors, α_i is the internal loss coefficient, and L is the cavity length. If we take $R = 99\%$, $\alpha_i = 20$ cm^{-1} and $L = 2$ μm, we obtain $\gamma = 1.4 \times 10^{-2}$. If we now assume $l = 24$ nm for the overall thickness of the active layers, we obtain $N_{th} \cong 11 \times 10^{18}$ cm^{-3}, which shows that the value of N_{th} is dominated by the loss term $(\gamma/\sigma l)$. From Eq. (9.4.3), taking $\eta_i \cong 1$ and $\tau = 2$ ns, we obtain $J_{th} = 3.84 \times 10^3$ A/cm^2. Assuming a diameter $D = 8$ μm for the active area, the threshold current is given by $I_{th} = (\pi D^2/4) J_{th} \cong 0.44$ mA.

9.4.8. Semiconductor Laser Applications

Semiconductor lasers lend themselves to a wide variety of both low-power and high-power applications, some of which are briefly reviewed here. We first refer to Table 9.7, which lists some characteristics of the most common DH and QW lasers. Since all structures shown are grown on either a GaAs or a InP substrate, the laser material is characterized by the active-layer-substrate combination. In each case, the laser wavelength is largely determined by the composition index of the active layer and, for a QW laser, also by the thickness of this layer. Most recent lasers use separated confinement (e.g., GRINSCH) QW and MQW layers in a gain-guiding, or more often, index-guiding configuration.

In the $Al_xGa_{1-x}As/Al_yGa_{1-y}As$ laser structures, the composition index y of the cladding layers must be larger than that, x, of the active layer. Depending on the value of the later composition index, the emission wavelength usually ranges from 720 to 850 nm. Low-power ($P = 5$–20 mW), single-stripe, devices are widely used in compact disk (CD) players

TABLE 9.7. Some characteristic parameters of the most important semiconductor laser diodes

Material/Substrate	InGaAlP/GaAs	AlGaAs/GaAs	InGaAsP/InP	InGaAs/GaAs
Wavelength (nm)	720–850	1200–1650	900–1100	630–700
Internal loss (cm^{-1})	4–15	5–10	2–10	~10
Threshold current density J_{th} (A/cm^2)	80–700	200–1500	50–400	200–3000
Characteristic temperature T_0 (K)	120–200	50–70	100–200	60–100

and laser printers. Higher power single-stripe lasers, laser arrays, laser bars, and stacks of laser bars (Figs. 6.9 and 6.10) are used to pump solid-state lasers, such as Nd (pump wavelength $\lambda_p \cong 800$ nm) or Tm:Ho ($\lambda_p \cong 790$ nm). Some of these laser systems and the corresponding fields of applications were discussed in Sect. 9.2 and in previous chapters.

In $In_{1-x}Ga_xAs_yP_{1-y}/InP$ lasers, lattice matching is achieved by letting $y \cong 2.2x$, and the oscillation wavelength covers the so-called second (centered at $\lambda = 1310$ nm, corresponding to $x = 0.27$) and third ($\lambda = 1550$ nm center wavelength, corresponding to $x = 0.42$) transmission windows of optical fibers. Thus, these lasers find their widest use in optical communications. Most recent optical communication systems use lasers around 1550-nm wavelength. Due to the relatively large group-delay dispersion of optical fibers around this wavelength, narrow-linewidth ($\Delta\nu_L < 10$ MHz) DFB lasers are now widely used. With these lasers, modulation rates up to a few Gbit/s have been demonstrated by direct modulation of the diode current. Even higher modulation rates (up to a few tens of Gbit/s) have also been demonstrated using external modulators, such as $LiNbO_3$ waveguide modulators. For communication systems operating at even greater bit-rates (from a few hundreds of Gbit/s to the Tbit/s range) wavelength-division-multiplexing (WDM) systems have increasingly been used. For this application, many DFB lasers tuned to distinct wavelengths in the low-loss region (spanning ~13 THz) around 1550-nm wavelength are used. Systems based on WDM thus allow exceptionally-high bit-rate capacity to be achieved.

$In_{1-x}Ga_xAs/GaAs$ strained-layer QW lasers allow oscillation over a wide range (900–1100 nm) at previously inaccessible wavelengths. Lasers with emission around 980-nm wavelength ($x = 0.8$) are of particular interest as pumps for Er-doped fiber amplifiers and lasers as well as for pumping Yb:Er:glass and Yb:YAG lasers. For these applications, output powers up to ~100 mW are available in a diffraction-limited beam (of 1×4 μm area) and up to ~1 W from a broader area (1×30 μm) device. To obtain higher output powers (~40 W or even greater), diode laser arrays and laser bars are also available. Given the favorable laser properties of strained-layer quantum wells, vertical-cavity surface-emitting lasers based on $In_{1-x}Ga_xAs/GaAs$ QW structures have been actively developed. They promise to offer interesting solutions for optical interconnects, optical communications, and optical signal processing.

InGaP/InGaAlP lasers are particularly interesting, since they emit radiation in the visible (red) region of the em spectrum.[53] The $In_{0.5}Ga_{0.5}P/In_{0.5}(Ga_{0.5-x}Al_x)P$ QW or MQW structure (where $x = 0.25$ for well barriers and $x = 0.35$ for confinement layers; see Fig. 9.25), oscillating at 670-nm wavelength, has been especially developed. These lasers are commercially available with sufficient high power (to ~20 mW) and long lifetime to be used for CD players or as substitutes for red-emitting He-Ne lasers in such applications as bar code scanners and general alignment.

The development of semiconductor lasers is by no means limited to the laser categories shown in Table 9.7. On the short wavelength side (blue-green region), the most interest-

ing category now appears to be the III–V nitride-based diode lasers, e.g., the $In_{0.2}Ga_{0.8}N/In_{0.05}Ga_{0.95}N$ MQW structure oscillating in the blue (417 nm).[54] In the same wavelength region, wide-gap II–VI lasers, such as ZnCdSe/ZnSSe QW lasers, have also been demonstrated. After a number of years of intense development, however, these lasers still suffer from a few technological limitations, particularly a rather limited operating lifetime ($\sim$100 h). Although nitride lasers also present similar lifetime problems (less than 100 h), their recent rapid progress suggest that they may become the best candidates for blue-green semiconductor emitters.* Blue-green lasers show potential for, e.g., a new generation of CD players, where, due to the shorter wavelength, substantially higher bit densities can be achieved on the CD. On the long wavelength side, we just mention IV–VI compounds such as the Pb and Sn salts (e.g., PbSSe, PbSnTe, and PbSnSe), oscillating in the middle-far infrared (4–29 μm). These lasers, however, must operate at cryogenic temperatures ($T < 100$ K) to avoid such problems as increased free carrier absorption and increased rate of nonradiative decay arising from the much narrower band gap. Due to the cryogenic requirement, these lasers have found only a limited use (e.g., in spectroscopy). It should be noted, however, that the recent invention of a quantum cascade laser promises efficient mid-infrared sources without requiring cryogenic temperatures.[56]

9.5. CONCLUSIONS

Chapter 9 considers a few of the most notable solid-state, dye, and semiconductor lasers. These lasers use high-density active media and share a few common features. A first feature is that they generally show wide and strong absorption band(s), which indicates that they are generally suitable for optical pumping. This type of pumping is in fact always used for solid-state and dye lasers and sometimes, also, for semiconductor lasers. High absorption coefficients allow lasers with dimensions down to a few microns (microlasers) to be obtained. As a second feature, these media generally show wide fluorescence and hence wide gain bandwidths. This characteristic offers tunability over wide (a few to several nanometers) bandwidths and it also implies that very short pulse durations (femtoseconds) can be obtained in mode-locked operation. A third feature is the large optical-to-optical laser efficiency for solid-state and dye media and the similarly large electrical-to-optical efficiency for semiconductors. Note that laser pumping, involving combination of these three categories of lasers, is increasingly used (e.g., diode-pumped solid-state lasers or solid-state laser-pumped dye lasers), allowing compact and efficient lasers to be achieved. Thus, as a conclusion, high-density laser media appear to present some of the best solutions to requirements for laser radiation in the visible-to-near-infrared range, even at high-power levels.

PROBLEMS

9.1. Make a diagram in which the tuning ranges of all tunable solid-state lasers considered in this chapter are plotted against oscillation wavelength.

9.2. For pollution monitoring, a tunable laser oscillating around 720-nm wavelength is needed. Which kind of solid-state laser would you use?

---

* Note added in proof: Extrapolated lifetimes in excess of 10^4 hours have, quite recently, been demonstrated for nitride-based diode lasers

9.3. For biomedical photocoagulation purposes, using an endoscopic apparatus, a cw laser with power exceeding 50 W must be used. Which laser would you use?

9.4. For material-working applications, a laser with an average power of 2 kW transmitted through a ~1-mm diameter optical fiber is needed. Which laser would you use?

9.5. Consider a 6-mm diameter, 10 cm long Nd:phosphate glass laser rod. Using data from Table 9.3 and the results discussed in Sect. 2.9.2, calculate the maximum inversion and the corresponding maximum value of stored energy allowed if the onset of amplified spontaneous emission is to be avoided. Compare the results obtained to those for a Nd:YAG rod of the same dimensions.

9.6. Referring to the energy level diagram of alexandrite in Fig. 9.8, assume that the $^4T_2$ and the ^2E states are strongly coupled and take $\tau_T = 1.5$ ms and $\tau_E = 6.6$ μs as the lifetimes of the two states, respectively. From the knowledge that the degeneracy of the two states is the same ($g=4$), calculate the effective lifetime of the $^4T_2$ state at $T=300$ K and $T=400$ K. If the true cross section for the $^4T_2 \rightarrow {}^4A_2$ transition is $\sigma \cong 4 \times 10^{-19}$ cm^2, calculate the effective value of the cross section at the two temperatures. Using these results, consider whether the laser threshold increases or decreases when the crystal temperature is raised from 300 to 400 K.

9.7. Consider a Cr:LiSAF laser longitudinally pumped, at 647.1-nm wavelength, by a Kr ion laser. Assume that the linearly polarized beam of the laser is sent along the c-axis of the LiSAF and assume an active medium with 1 at.% Cr^{3+} concentration and a length of $l=4$ mm. Also assume that both pump and mode spot sizes are matched at a value of 60 μm, the output coupler transmission is 1%, and the internal loss per pass is 1%. Using data from Fig. 9.11 and Table 9.5 and neglecting both ground-state and excited-state absorption, calculate the expected threshold pump power.

9.8. Referring to Problem 9.7, how would the expression for threshold pump power, given by Eq. (6.3.19), have to be modified if ground-state absorption, characterized by a loss per pass γ_a, and excited-state absorption, characterized by an excited-state absorption cross section σ_{ESA}, were taken into account? Compare the result to that given in Ref. 25.

9.9. Derive an expression for the threshold pump power of a longitudinally pumped dye laser, taking into account triplet-triplet absorption (assume Gaussian transverse profiles for both pump and mode beams). Compare this expression to that obtained for Cr:LiSAF in the previous problem.

9.10. Using the expression for the threshold pump power obtained in Problem 9.9 and using data from Fig. 9.13, calculate the threshold pump power for an Ar^+-pumped rhodamine 6G (see Fig. 9.17) laser oscillating at 580-nm wavelength. For this calculation, assume an output coupling of 3%, an internal loss per pass of 1%; assume also that 80% of the pump power is absorbed in the dye jet stream; take the lifetime for the first excited singlet state as 5 ns, the intersystem crossing rate as $k_{ST} \cong 10^7$ s^{-1}, and the triplet lifetime as $\tau_T \cong 0.1$ μs. Compare this value of P_{th} to that obtained for Cr:LiSAF in Problem 9.7 and explain the numerical differences.

9.11. At the very small values of the thickness d corresponding to the minimum of J_{th} in Fig. 9.23, the expression for the beam confinement factor Γ of a DH semiconductor laser, given by Eq. (9.4.10), can be approximated by $\Gamma \cong D^2/2$, where D is expressed by Eq. (9.4.11). Using this approximation, calculate the expression for the thickness d_m that minimizes J_{th}. From data given in Example 9.1, calculate the value of d_m and the corresponding value of J_{th}.

9.12. From the expression for the output power of a semiconductor laser given in Example 9.3, derive an expression for the laser slope efficiency. Using data given in Example 9.1, calculate the predicted slope efficiency of a DH GaAs/AlGaAs laser by using an applied voltage of 1.8 V.

9.13. Assume that the beam, at the exit face of a semiconductor laser, is spatially coherent. Assume that the transverse field distributions have Gaussian profiles in the directions parallel and perpendicular to the junction, with spot sizes $w_\parallel$ and $w_\perp$ respectively. Assume also that, for both

field distributions, the location of the beam waists occurs at the exit face. Given these assumptions, derive an expression for the propagation distance at which the beam becomes circular. Taking $w_\perp = 0.5$ μm and $w_\parallel = 2.5$ μm, calculate the value of this distance for $\lambda = 850$ nm.

9.14. Considering that the refractive index of a semiconductor n is a relatively strong function of the wavelength λ, derive an expression for the frequency difference between two consecutive longitudinal modes of a Fabry–Perot semiconductor laser [express this frequency difference in terms of the material group index $n_g = n - \lambda(dn/d\lambda)$].

9.15. The calculations leading to Fig. 9.30a were made assuming $kL = 2$, where k is the coupling constant between forward- and backward-propagating beams in a DFB laser and L is its length. From the definition of k given in Sect. 9.4.6, calculate the value n_1 in Eq. (9.4.16) for $\lambda = 1550$ nm and $L = 600$ μm.

9.16. The two strongest peaks in Fig. 9.30a are seen from the figure to be separated by a normalized frequency difference $\Delta(\delta L) \cong 7.28$. From the definition of the normalized frequency detuning δL given in Sect. 9.4.6, calculate the frequency difference $\Delta\nu$ between the two modes by taking $L = 600$ μm, $n_0 = 3.4$, and $\lambda = 1550$ nm for a InGaAsP DFB laser. Compare this value to the corresponding one obtained for the frequency separation between two consecutive longitudinal modes of a Fabry–Perot semiconductor laser with the same length and wavelength and a group index n_g equal to n_0.

REFERENCES

1. A. A. Kaminskii, *Crystalline Lasers: Physical Processes and Operating Systems* (CRC Press, 1996).
2. T. H. Maiman, Stimulated Optical Radiation in Ruby Masers, *Nature* **187**, 493 (1960).
3. T. H. Maiman, Optical Maser Action in Ruby, *Brit. Commun. Electron.* **7**, 674 (1960).
4. W. Koechner, *Solid-State Laser Engineering*, 4th ed. (Springer Berlin, 1996), Sects. 2.2, 3.6.1.
5. Ref. 4, Sects. 2.3.1., 3.6.3.
6. E. Snitzer and G. C. Young, Glass Lasers, in *Lasers*, vol. 2 (A. K. Levine, ed.) (Marcel Dekker, NY, 1968), Chap. 2.
7. Ref. 4, Sect. 2.3.4.
8. T. Y. Fan, Diode-Pumped Solid-State Lasers, in *Laser Sources and Applications* (A. Miller and D. M. Finlayson, eds.) (Institute of Physics, Bristol, 1996), pp. 163–93.
9. P. Lacovara *et al.*, Room-Temperature Diode-Pumped Yb:YAG Laser, *Opt. Letters* **16**, 1089 (1991).
10. H. Bruesselbach and D. S. Sumida, 69-W-average-power Yb:YAG Laser, *Opt. Letters* **21**, 480 (1996).
11. G. Huber, Solid-State Laser Materials, in *Laser Sources and Applications* (A. Miller and D. M. Finlayson, eds.) (Institute of Physics, Bristol, 1996), pp. 141–62.
12. E. V. Zharikov *et al.*, *Sov. J. Quantum Electron.* **4**, 1039 (1975).
13. S. J. Hamlin, J. D. Myers, and M. J. Myers, High-Repetition Rate Q-Switched Erbium Glass Lasers, in *Eyesafe Lasers: Components, Systems, and Applications* (A. M. Johnson, ed.) *SPIE* **1419**, 100 (1991).
14. S. Taccheo, P. Laporta, S. Longhi, O. Svelto, and C. Svelto, Diode-Pumped Bulk Erbium-Ytterbium Lasers, *Appl. Phys.* **B63**, 425 (1996).
15. D. Sliney and M. Wolbarsht, *Safety with Lasers and Other Optical Sources* (Plenum, NY, 1980).
16. T. Y. Fan, G. Huber, R. L. Byer, and P. Mitzscherlich, Spectroscopy and Diode Laser-Pumped Operation of Tm, Ho:YAG, *IEEE J. Quantum Electron.* **QE-24**, 924 (1988).
17. D. C. Hanna, Fibre Lasers, in *Laser Sources and Applications* (A. Miller and D. M. Finlayson, eds.) (Institute of Physics, Bristol, 1996), pp. 195–208.
18. E. Snitzer, Optical Maser Action on Nd^{3+} in a Barium Crown Glass, *Phys. Rev. Letters* **7**, 444 (1961).
19. J. C. Walling, O. G. Peterson, H. P. Jenssen, R. C. Morris, and E. W. O'Dell, Tunable Alexandrite Lasers, *IEEE J. Quantum Electron.* **QE-16**, 1302 (1980).
20. L. F. Mollenauer, Color Center Lasers, in *Laser Handbook*, vol. 4 (M. L. Stitch and M. Bass, eds.) (North Holland, Amsterdam, 1985), pp. 143–228.
21. P. F. Moulton, Spectroscopy and Laser Characteristics of Ti:Al_2O_3, *J. Opt. Soc. Am. B* **3**, 125 (1986).

22. G. Hüber, Solid-State Laser Materials: Basic Properties and New Developments, in *Solid-State Lasers: New Developments and Applications* (M. Inguscio and R. Wallenstein, eds.) (Plenum, NY, 1993), pp. 67–81.
23. P. Albers, E. Stark, and G. Huber, Continuous-Wave Laser Operation and Quantum Efficiency of Titanium-Doped Sapphire, *J. Opt. Soc. Am. B* **3**, 134 (1986).
24. S. A. Payne, L. L. Chase, L. K. Smith, W. L. Kway, and H. W. Newkirk, Laser Performance of $LiSrAlF_6:Cr^{3+}$, *J. Appl. Phys.* **66**, 1051 (1989).
25. S. A. Payne L. L. Chase, H. W. Newkirk, L. K. Smith, and W. F. Krupke, $LiCaAlF_6:Cr^{3+}$: A Promising New Solid-State Laser Material, *IEEE J. Quantum Electron.* **QE-24**, 2243 (1988).
26. Dye Lasers, 2d ed (F. P. Schäfer, ed.) (Springer-Verlag, Berlin, 1977).
27. H. D. Försterling and H. Kuhn, *Physikalische Chemie in Experimenten, Ein Praktikum* (Verlag Chemie, Weinheim, Germany 1971).
28. J. T. Verdeyen, *Laser Electronics*, 3d ed. (Prentice-Hall, Englewood Cliffs, NJ, 1995), Fig. 10.19.
29. P. P. Sorokin and J. R. Lankard, Stimulated Emission Observed from an Organic Dye, Chloro-Aluminum Phtalocyanine, *IBM J. Res. Dev.* **10**, 162 (1966).
30. F. P. Schäfer, F. P. W. Schmidt, and J. Volze, Organic Dye Solution Laser, *Appl. Phys. Letters* **9**, 306 (1966).
31. *Semiconductor Lasers: Past, Present, Future* (G. P. Agrawal, ed.) (AIP, Woodbury, NY, 1995).
32. G. P. Agrawal and N. K. Dutta, *Long-Wavelength Semiconductor Lasers* (Chapman and Hall, NY, 1986).
33. N. G. Basov, O. N. Krokhin, and Y. M. Popov, Production of Negative Temperature States in *p*-n Junctions of Degenerate Semiconductors, *Journal Exp. Theoret. Physics* **40**, 1320 (1961).
34. R. N. Hall, G. E. Fenner, J. D. Kinhsley, F. H. Dills, and G. Lasher, Coherent Light Emission from GaAs Junctions, *Phys. Rev. Letters* **9**, 366 (1962).
35. M. I. Nathan, W. P. Dumke, G. Burns, F. H. Dills, and G. Lasher, Stimulated Emission of Radiation from GaAs *p-n* Junctions, *Appl. Phys. Letters* **1**, 62 (1962).
36. N. Holonyak, Jr. and S. F. Bevacqua, Coherent (Visible) Light Emission from $Ga(As_{1-x}P_x)$ Junctions, *Appl. Phys. Letters* **1**, 82 (1962).
37. T. M. Quist, R. J. Keyes, W. E. Krag, B. Lax, A. L. McWhorter, R. H. Rediker, and H. J. Zeiger, Semiconductor Maser of GaAs, *Appl. Phys. Letters* **1**, 91 (1962).
38. Z. I. Alferov, V. M. Andreev, V. I. Korolkov, E. L. Portnoi, and D. N. Tretyakov, Coherent Radiation of Epitaxial Heterojunction Structures in the AlAs-GaAs System, *Soviet. Phys. Semicond.* **2**, 1289 (1969).
39. I. Hayashi, M. B. Panish, and P. W. Foy, A Low-Threshold Room-Temperature Injection Laser, *IEEE J. Quantum Electron.* **QE-5**, 211 (1969).
40. H. Kressel and H. Nelson, Close Confinement Gallium Arsenide *p-n* Junction Laser with Reduced Optical Losses at Room Temperature, *RCA Rev.* **30**, 106 (1969).
41. N. Chinone, H. Nakashima, I. Ikushima, and R. Ito, Semiconductor Lasers with a Thin Active Layer (> 0.1 μm) for Optical Communications, *Appl. Opt.* **17**, 311 (1978).
42. D. Botez, Analytical Approximation of the Radiation Confinement Factor for the TE_0 Mode of a Double-Heterojunction Laser, *IEEE J. Quantum Electron.* **QE-14**, 230 (1978).
43. J. J. Coleman, Quantum-Well Heterostructure Lasers, in *Semiconductor Lasers: Past, Present, Future* (G. P. Agrawal, ed.) (AIP, Woodbury, NY, 1995), Fig. 1.6.
44. *Quantum Well Lasers* (Peter S. Zory, ed.) (Academic Press, Boston, 1993).
45. Ref. 32, Figs. 9.8, 9.10.
46. Ref. 44, Chap. 3.
47. H. Kogelnik and C. V. Shank, Stimulated Emission in a Periodic Structure, *Appl. Phys. Letters* **18**, 152 (1971).
48. Ref. 32, Chap. 7.
49. N. Chinone and M. Okai, Distributed Feed-Back Semiconductor Lasers, in *Semiconductor Lasers: Past, Present, Future* (G. P. Agrawal, ed.) (AIP, Woodbury, NY, 1995), Chap. 2, pp. 28–70.
50. H. A. Haus and C. V. Shank, Antisymmetric Taper of Distributed Feedback Lasers, *IEEE J. Quantum Electron.* **QE-12**, 532 (1976).
51. C. J. Chang-Hasnain, Vertical-Cavity Surface-Emitting Lasers, in *Semiconductor Lasers: Past, Present, Future* (G. P. Agrawal, ed.) (AIP, Woodbury, NY, 1995), Chap. 4, pp. 110–44.
52. C. J. Chang-Hasnain, J. P. Harbison, C.-H. Zah, M. W. Maeda, L. T. Florenz, N. G. Stoffel, and T.-P. Lee, Multiple Wavelength Tunable surface-Emitting Laser Array, *IEEE J. Quantum Electron.* **QE-27**, 1368 (1991).
53. G.-I. Hatakoshi, Visible Semiconductor Lasers, in *Semiconductor Lasers: Past, Present, Future* (G. P. Agrawal, ed.) (AIP, Woodbury, NY, 1995), Chap. 6, pp. 181–207.
54. S. Nakamura *et al.*, *Japn. J. Appl. Phys.* **35**, L74 (1994).
55. P. Moulton, New Developments in Solid-State Lasers, *Laser Focus* **14**, 83 (May 1983).
56. J. Faist, F. Capasso, D. L. Sivco, C. Sirtori, A. L. Hutchinson, and A. Y. Cho, *Science* **264**, 553 (1994).
57. M. Bass, T. F. Deutsch, and M. J. Weber, Dye Lasers, in *Lasers*, Vol. 3 (A. K. Levine and A. De Maria, eds.) (Marcel Dekker, NY, 1971) p. 275.

10

Gas, Chemical, Free-Electron, and X-Ray Lasers

10.1. INTRODUCTION

Chapter 10 considers the most important types of lasers involving low-density active media, namely, gas, chemical, and free-electron lasers, in addition to some aspects of x-ray lasers using highly ionized plasmas. The main emphasis, again, is on the physical behavior of the laser and relating this behavior to general concepts developed in the previous chapters. Some engineering details are also presented with the intention of providing a better insight into the behavior of a particular laser. To complete the picture, some data about laser performances (e.g., oscillation wavelength(s), output power or energy, wavelength tunability, etc.) are also included since they are directly related to the potential applications of the given laser.

10.2. GAS LASERS

In general, for gases, energy levels broadening is rather small (on the order of a few GHz or less), since line-broadening mechanisms are weaker than in solids. For gases at the low pressure often used in lasers (a few tens of Torr), in fact, collision-induced broadening is very small, and the linewidth is essentially determined by Doppler broadening. Thus, no broad absorption bands are present in the active medium, so optical pumping by cw or pulsed lamps is not used. Optical pumping would in fact be very inefficient, since the emission spectrum of these lamps is more or less continuous. Therefore gas lasers are usually excited by electrical means, i.e., by passing a sufficiently large current (which may be continuous, at radio-frequency, or pulsed) through the gas. (The principal pumping mechanisms occurring in gas lasers are discussed in Sect. 6.4.) Note that some lasers can also be pumped by mechanisms other than electrical pumping, in particular gas dynamic

expansion, chemical pumping, and optical pumping using another laser (the latter is particularly used for far-infrared lasers).

Once a given species is in its excited state, it can decay to lower states (including the ground state) by four different processes: (1) Collisions between an electron and the excited species, in which the electron takes up the excitation energy as kinetic energy (superelastic collision). (2) Near-resonant collisions between excited species and the same or a different species in the ground state. (3) Collisions with the walls of the container. (4) Spontaneous emission. Regarding this last case, we must always take into account the possibility of radiation trapping, particularly for the, usually very strong, uv or vuv transitions. This process slows down the effective rate of spontaneous emission (see Sect. 2.9.1).

For a given discharge current, these excitation and de-excitation processes lead eventually to some equilibrium distribution of population among the energy levels. Thus, due to the many processes involved, producing a population inversion in a gas is a more complicated matter than, e.g., in a solid-state laser. In general, a population inversion between two given levels occurs when either (or both) of the following circumstances occur: (1) The excitation rate is greater for the upper laser level (level 2) than for the lower laser level (level 1). (2) The decay of level 2 is slower than that of level 1. In this regard, we recall that a necessary condition for cw operation is that the rate of the transition $2 \rightarrow 1$ must be smaller than the decay rate of level 1 [see Eq. (7.3.1)]. If this condition is not satisfied, however, laser action can still occur, under pulsed operation, provided the first condition is satisfied (self-terminating lasers).

10.2.1. Neutral Atom Lasers

These lasers use neutral atoms in either gaseous or vapor form. Neutral atom gas lasers constitute a large class of lasers, including, in particular, most of the noble gases. All these lasers oscillate in the infrared (1–10 μm), apart from the notable exceptions of green and red emission from the He-Ne laser. Metal vapor lasers also constitute a large class of lasers, including, for example, Pb, Cu, Au, Ca, Sr, and Mn. These lasers generally oscillate in the visible; the most important example is the copper vapor laser oscillating on its green (510-nm) and yellow (578.2-nm) transitions. All metal vapor lasers are self-terminating and therefore operate in a pulsed regime.

10.2.1.1. Helium Neon Laser

The He-Ne laser is certainly the most important of the noble gas lasers. Laser action is obtained from transitions of the neon atom, while helium is added to the gas mixture to greatly facilitate the pumping process.[1,2] The laser oscillates on many wavelengths; by far the most popular is $\lambda = 633\,\text{nm}$ (red). Other wavelengths include green (543 nm) and infrared, at $\lambda = 1.15\,\mu\text{m}$ and $\lambda = 3.39\,\mu\text{m}$. The He-Ne laser, oscillating on its $\lambda = 1.15\,\mu\text{m}$ transition, was the first gas laser and the first cw laser to be operated.[3]

Figure 10.1 shows the energy levels of the He-Ne system relevant for laser action. The level notation for He complies with Russell–Saunders coupling; the principal quantum number of the given level is also indicated as the first number. Thus the 1^1S state

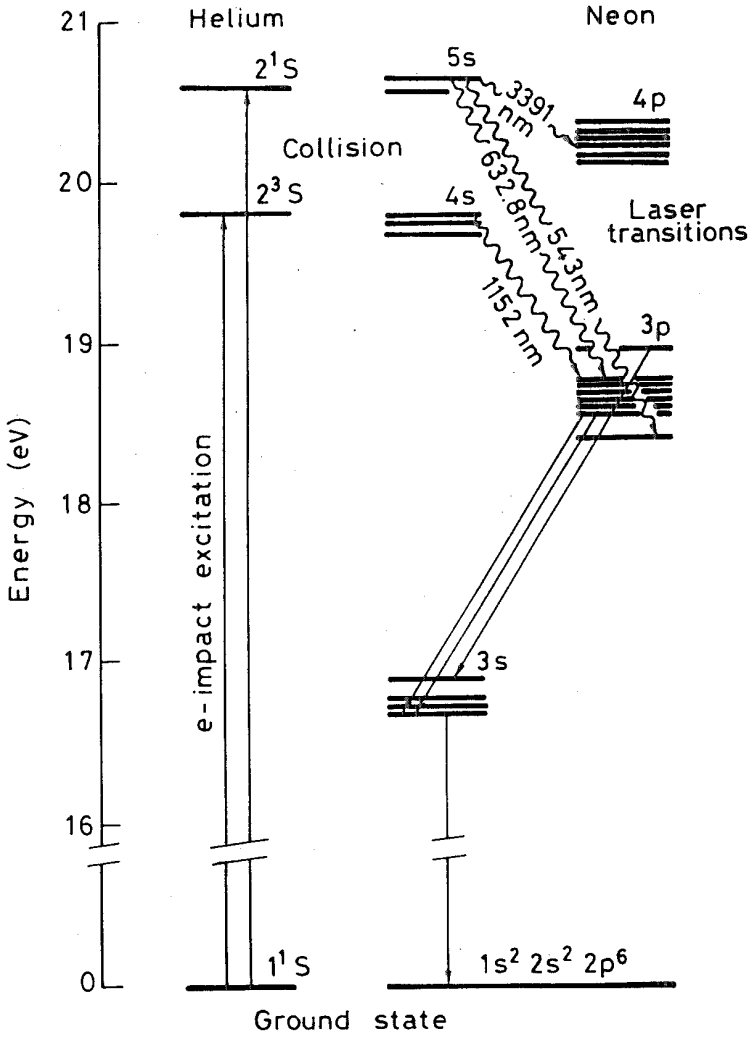

FIG. 10.1. Relevant energy levels of the He-Ne laser.

corresponds to the case when the two electrons of He are in the $1s$ state with opposite spins. The 2^3S and 2^1S states correspond to one of the two electrons being raised to the $2s$ state, with its spin either in the same or opposite direction to that of the other electron, respectively. Neon, on the other hand, has an atomic number of 10 and a number of ways have been used, such as Paschen or Racah notation, to indicate its energy levels. For simplicity, however, we simply indicate here the electron configuration corresponding to each level. Therefore, the ground state is indicated by $1s^2 2s^2 2p^6$, while the excited states in the figure correspond to when one $2p$ electron is raised to excited s states ($3s$, $4s$, and $5s$) or excited p states ($3p$ and $4p$). Note that, due to interaction with the remaining five electrons in the $2p$ orbitals, these s and p states are split into 4 and 10 sublevels, respectively.

It is apparent from Fig. 10.1 that the He levels, 2^3S and 2^1S, are nearly resonant with the Ne $4s$ and $5s$ states. Since the 2^3S and 2^1S levels are metastable ($S \rightarrow S$ transitions are electric-dipole-forbidden, and, furthermore, the $2^3S \rightarrow 2^1S$ transition is also spin-forbidden), He atoms in these states prove very efficient at pumping Ne $4s$ and $5s$ levels by resonant energy transfer. It has been confirmed that this process is dominant in producing population inversion in the He-Ne laser, although direct electron-Ne collisions also contribute to the pumping. Since significant population can then be build-up in the Ne $4s$ and $5s$ states, they prove suitable candidates as upper levels for laser transitions. Taking account

of the selection rules, possible transitions are those to the p states. In addition, the decay time of the s states ($\tau_s \cong 100$ ns) is an order of magnitude longer than the decay time of the p states ($\tau_p \cong 10$ ns). Therefore, condition (7.3.1) for operating as a cw laser is satisfied. Note that electron impact excitation rates, from the ground state to the $3p$ and $4p$ levels, are much smaller than the corresponding rates to the $4s$ and $5s$ levels because smaller values of the cross section are involved. However, direct excitation to the $3p$ and $4p$ levels also plays a relevant role in determining laser performance.

The preceding discussion indicates that we can expect laser action in Ne to occur from $5s$ and $4s$ levels, as upper levels, to $3p$ and $4p$ levels, as lower levels. Figure 10.1 indicates some of the most important laser transitions arising from these levels. For transitions differing widely in wavelength ($\Delta\lambda > 0.2\lambda$), the actual oscillating transition depends on the wavelength at which the peak reflectivity of the multilayer dielectric mirror is centered (see Fig. 4.9). Laser transitions are predominantly broadened by the Doppler effect; for instance, in the red He-Ne laser transition ($\lambda = 633$ nm in vacuum and $\lambda = 632.8$ nm in air), Doppler broadening leads to a linewidth of ~1.5 GHz (see also Example 2.6). By comparison, natural broadening, according to Eq. (2.5.13), is estimated to be $\Delta\nu_{nat} = 1/2\pi\tau \cong 19$ MHz, where $\tau^{-1} = \tau_s^{-1} + \tau_p^{-1}$ and τ_s, τ_p are the lifetimes of the s and p states, respectively. Collision broadening contributes even less than natural broadening. (For example, for pure Ne, one has $\Delta\nu_c \cong 0.6$ MHz at the pressure of $p \cong 0.5$ torr, see Example 2.2.) Table 10.1 summarizes some spectroscopic properties of the 633-nm laser transition.

Figure 10.2 shows the basic design of a He-Ne laser. The discharge is produced between a ring anode and a large tubular cathode, which can thus withstand collisions from positive ions. The discharge is confined to a capillary for most of the tube length, so high inversion is achieved only where the capillary is present. The large volume of gas, available in the tube surrounding the capillary, acts as a reservoir to replenish the He-Ne mixture in the capillary. When a polarized output is needed, a Brewster angle plate is also inserted inside the laser tube. The laser mirrors are directly sealed at the two tube ends. The most commonly used resonator configuration is nearly hemispherical, since it is easy to adjust, very stable against misalignment, and readily gives TEM_{00} mode operation. The only disadvantage of this configuration is that it does not fully use the volume of the plasma discharge, since the mode spot size is much smaller at the plane mirror than at the concave mirror. If, however, the left-hand mirror in Fig. 10.2 is chosen as the plane mirror, the region

TABLE 10.1. Spectroscopic properties of laser transitions and gas mixture composition in some relevant atomic and ionic gas lasers

Laser Type	He-Ne	Copper Vapor	Argon Ion	He-Cd
Laser wavelength (nm)	633	510.5	514.5	441.6
Cross section (10^{-14} cm^2)	30	9	25	9
Upper state lifetime (ns)	150	500	6	700
Lower state lifetime (ns)	10	$\approx 10^4$	~1	1
Transition linewidth (GHz)	1.5	2.5	3.5	1
Partial pressures of gas mixture (Torr)	4 (He) 0.8 (Ne)	40 (He) 0.1-1 (Cu)	0.1 (Ar)	10 (He) 0.1 (Cd)

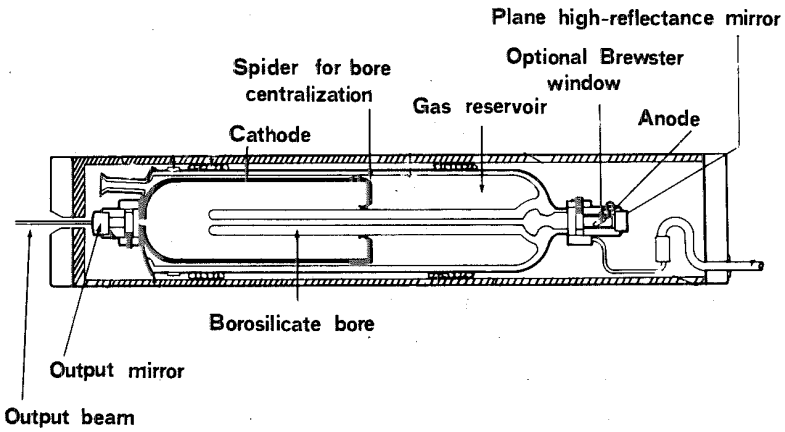

FIG. 10.2. Internal design of a hard-sealed helium neon laser. (Courtesy of Melles–Griot).

of smaller spot size, for the near-hemispherical TEM_{00} mode, is outside the capillary, i.e., in a low-inversion region.

One of the most characteristic features of a He-Ne laser is that the output power does not increase monotonically with the discharge current, but reaches a maximum and thereafter decreases. For this reason, commercially available He-Ne lasers are provided with a power supply designed to give only the optimum current. The fact that there is an optimum value of current, i.e., of current density J within the capillary, is because (at least for 633-nm and 3.39-μm transitions), at high current densities, de-excitation of the He (2^3S and 2^1S) metastable states takes place not only by collision at the walls but also by superelastic collision processes such as:

$$\mathrm{He}(2^1S) + e \rightarrow \mathrm{He}(1^1S) + e \tag{10.2.1}$$

Since the rate of this process is proportional to electron density N_e, and hence to J, the overall rate of de-excitation can be written as $k_2 + k_3J$. In this expression k_2 is a constant that represents de-excitation due to collisions with the walls and k_3J, where k_3 is also a constant, represents the superelastic collision rate of process (10.2.1). The excitation rate can be expressed as k_1J, where k_1 is again a constant. Under steady-state conditions, we can then write $N_tk_1J = (k_2 + k_3J)N^*$, where N_t is the ground-state He-atom population and N^* is the excited (2^1S) state population. The equilibrium 2^1S population is then given by

$$N^* = N_t\left(\frac{k_1J}{k_2 + k_3J}\right) \tag{10.2.2}$$

which saturates at high current densities. Since the steady-state population of the $5s$ state of Ne is established by near-resonant energy transfer from the He 2^1S state, the population of the upper $5s$ laser level also shows a similar saturation behavior as J increases (see Fig. 10.3). In the absence of laser action, the population of the lower laser level ($3p$ or $4p$) is produced by direct pumping from ground-state Ne atoms and radiative cascading from higher levels; experimentally, it is found to increase linearly with J (see Fig. 10.3). Therefore, as the discharge current is increased, the population difference, and hence the output power, rises to some optimum value and thereafter falls.

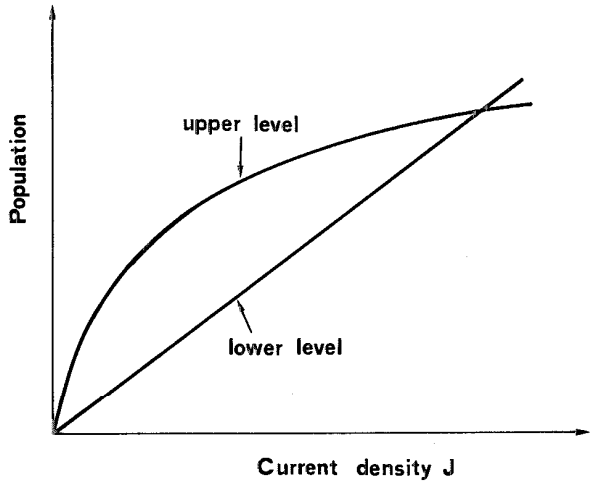

FIG. 10.3. Schematic dependence on current density of upper level and lower level populations in a He-Ne laser.

Besides the optimum value of current density, the He-Ne laser has optimum values for other operational parameters, namely:

- Product of total gas pressure p and capillary diameter D ($pD = 3.6$–$4\,\text{Torr} \times \text{mm}$); this optimum value of the pD product arises because the electron temperature must be optimized (see Sect. 6.4.5).
- Ratio of the partial pressures of He and Ne (~5:1 at $\lambda = 632.8\,\text{nm}$ and ~9:1 at $\lambda = 1.15\,\mu\text{m}$).
- Capillary diameter ($D \cong 2\,\text{mm}$); for a constant value of pD, i.e., for a given electron temperature, all electron collision excitation processes scale simply as the number of atoms available for excitation. Since both upper and lower laser levels are ultimately populated by electron collision processes, their populations, and hence also laser gain, are proportional to p, i.e., to D^{-1} at constant pD. Diffraction losses of the laser cavity, on the other hand, increase as D is decreased; a value of the capillary diameter that optimizes the net gain (gain minus diffraction losses) is therefore expected.

According to the behavior in Fig. 10.3, He-Ne lasers are typically low-power devices. (Under optimized conditions, the available output power at the 633-nm transition may range from 1 to 10 mW, for tube lengths ranging from 20–50 cm, while the output power on the green transition is typically an order of magnitude less.) The efficiency of a He-Ne laser, on any of its laser transitions, is always very low ($< 10^{-3}$); a major cause of low efficiency is the low quantum efficiency. In fact, from Fig. 10.1, we readily see that each elementary pumping cycle requires an energy of ~20 eV while laser photon energy is less than 2 eV. The narrow gain linewidth is an advantage when single longitudinal mode is required. In fact, if the cavity length is short enough ($L < 15$–$20\,\text{cm}$), single-longitudinal-mode oscillation is readily achieved when the cavity length is tuned (by a piezo-electric translator) to bring a cavity mode into coincidence with the peak of the gain line (see Sect. 7.8.2.1). Single-mode He-Ne lasers can then be frequency stabilized to a high degree [$(\Delta\nu/\nu) = 10^{-11}$–$10^{-12}$] against a frequency reference (such as a high-finesse Fabry–Perot interferometer or, for absolute stabilization, against, e.g., an $^{129}I_2$ absorption line for the 633-nm transition).

He-Ne lasers oscillating on the red transition are widely used for many applications requiring a low-power visible beam (such as alignment or bar code scanners). Most store

checkouts use red He-Ne lasers to read information encoded in a product's bar code; for some of these applications, however, He-Ne lasers face now strong competition from red-emitting semiconductor lasers, which are smaller and more efficient. Given the greater visibility of a green beam, green-emitting He-Ne lasers are increasingly used for alignment and cell cytometry. In the latter application, individual cells (e.g., red blood cells), stained by suitable fluorochromes, are rapidly flowed through a capillary onto which an He-Ne laser is focused; the fluorochromes are characterized by subsequent scattering or fluorescent emission. Single-mode He-Ne lasers are also often used in metrological applications (e.g., very precise, interferometric, distance measurements) and holography.

10.2.1.2. Copper Vapor Laser

Figure 10.4 shows relevant energy levels of the copper vapor laser, where Russell–Saunders notation is again used.[4] The $^2S_{1/2}$ ground state of Cu corresponds to the electron configuration $3d^{10}4s^1$, while the excited $^2P_{1/2}$ and $^2P_{3/2}$ levels correspond to the outer $4s$ electron being promoted to the next higher $4p$ orbital. The $^2D_{3/2}$ and $^2D_{5/2}$ levels arise from the electron configuration $3d^9 4s^2$ in which an electron is promoted from the $3d$ to the $4s$ orbital.

The relative values of the corresponding cross sections are such that the rate of electron impact excitation to the P states is greater than that to the D states; thus the P states are preferentially excited by electron impact. The $^2P \rightarrow {}^2S_{1/2}$ transition is strongly electric-dipole allowed (selection rules for optically allowed transitions require $\Delta J = 0$ or ± 1), so the corresponding absorption cross section is quite large. At the temperature used for Cu lasers ($T = 1500°C$), the vapor pressure is sufficiently high (~0.1 torr), however, that the $^2P \rightarrow {}^2S_{1/2}$ transition is completely trapped. Thus, the only effective decay route of the ^2P state is through the ^2D states; the corresponding decay time is rather long (~0.5 μs) since the transition is only weakly allowed.

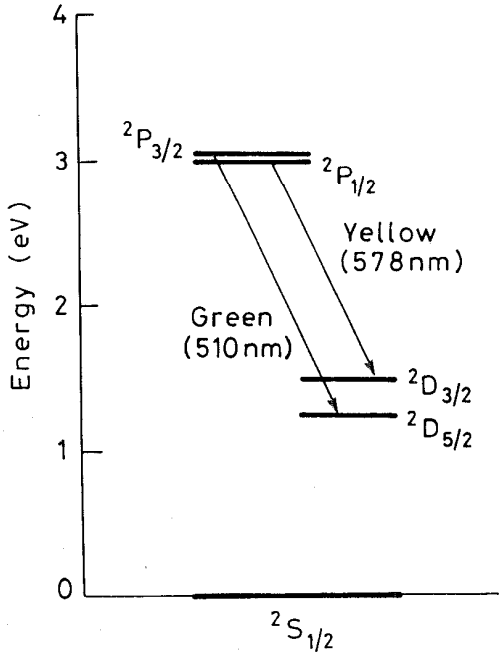

FIG. 10.4. Energy levels of copper atoms relevant to laser operation.

It then follows that, since the ^2P states can accumulate a large population, they are good candidates for upper laser levels. Thus laser action in Cu can occur on both the $^2P_{3/2} \rightarrow {}^2D_{5/2}$ (green) and $^2P_{1/2} \rightarrow {}^2D_{3/2}$ (yellow) transitions. Note that the $^2D \rightarrow {}^2S$ transition is electric-dipole forbidden and the lifetime of the ^2D state is very long (a few tens of microseconds). It then follows that the laser transition is self-terminating, so the laser can operate only on a pulsed basis, with pulse duration on the order of or shorter than the lifetime of the ^2P state. One should also note that the $^2D \rightarrow {}^2S$ decay occurs mainly via superelastic collisions, involving cold electrons that remain after the pump pulse; the corresponding decay rate sets an upper limit to the repetition rate of the laser. Table 10.1 indicates relevant spectroscopic properties of the copper vapor green transition as an example.

Metal vapor laser construction is based on the arrangement schematically shown in Figure 10.5, where the vapor is contained in an alumina tube which is thermally isolated in a vacuum chamber. The necessary high temperature is usually maintained by power dissipated in the tube due to repetitively-pulsed pumping current. The anode and cathode, in the form of ring electrodes, are placed at the ends of the alumina tube. A 25–50 Torr neon buffer gas provides enough electron density, after passage of the discharge pulse, to allow for de-excitation of the lower ^2D state by superelastic collisions. The neon gas is also helpful in reducing the diffusion length of the Cu vapor, thus preventing metal vapor deposition on the (cold) end windows. More recently, the so-called copper-HyBrID lasers were introduced, which use HBr in the discharge. Since, in this case, CuBr molecules are formed in the discharge region and these molecules are much more volatile than Cu atoms, lower temperatures are required in the gas discharge.

Copper vapor lasers are commercially available with average output powers in excess of 100 W, short pulse durations (30–50 ns), high-repetition rates (up to ~10 kHz), and relatively high efficiency (~1%). The latter is the result of both the high quantum efficiency of the copper laser (~55%; see Fig. 10.4) and the high electron-impact cross section of the $^2S \rightarrow {}^2P$ transition. Even higher output powers (~200 W) and higher efficiencies (~3%) were recently obtained with copper-hybrid lasers.

Copper vapor lasers are used in some industrial applications (such as high-speed photography, resistor trimming, and, more recently, micromachining) and as a pump for dye

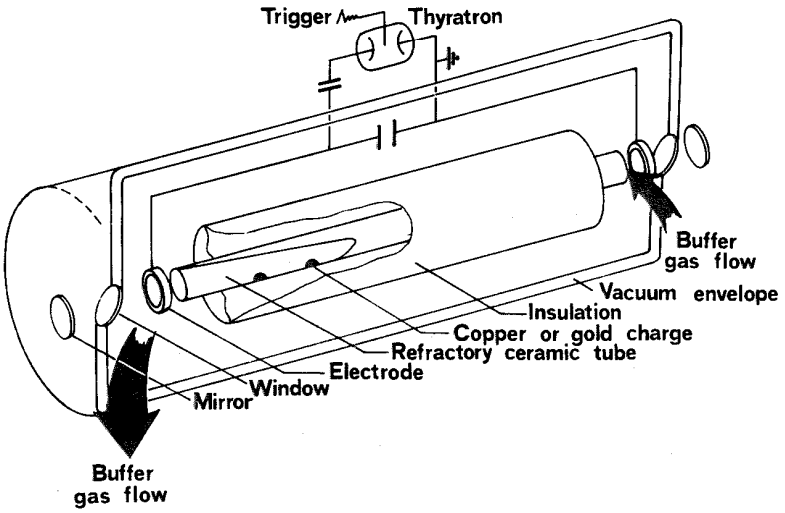

FIG. 10.5. Schematic construction of a Cu vapor laser. (Courtesy of Oxford Lasers, Ltd.)

lasers. In particular, in high-speed flash photography, the short-pulse (tens of nanoseconds) and high-repetition rate (10–20 kHz) are exploited in stroboscopic illumination of various, rapidly moving, objects (e.g., a bullet in flight). A large facility based on copper-laser-pumped dye lasers (using many copper lasers, each with an average power to 100 W) is currently used in a pilot plant, in the United States, for ^{235}U isotope separation.

10.2.2. Ion Lasers

In an ionized atom, the energy levels scale is expanded in comparison with neutral atoms. In this case, in fact, an electron in the outermost orbital(s) experiences the field due to the positive charge Ze of the nucleus (Z is the atomic number and e the electronic charge) screened by the negative charge $(Z-2)e$ of the remaining electrons. Assuming for simplicity that the screening is complete, the net effective charge is then $2e$, rather than simply e for the corresponding neutral atom. This energy scale expansion means that ion lasers typically operate in the visible or ultraviolet regions. As in the case of neutral atom lasers, ion lasers can be divided into two categories: (1) *Ion gas lasers*, involving most of the noble gases; the most notable example is the Ar^+ laser, considered in Sect. 10.2.2.1, and the Kr^+ laser. Both lasers oscillate on many transitions; the most common are green and blue (514.5 nm and 488 nm, respectively) for the Ar^+ laser and red (647.1 nm) for the Kr^+ laser. (2) *Metal-ion vapor lasers*, involving many metals (Sn, Pb, Zn, Cd, and Se); the most notable example is the He-Cd laser, discussed in Sect. 10.2.2.2, and the He-Se laser.

10.2.2.1. Argon Laser

Figure 10.6 shows a simplified scheme for relevant energy levels in an argon laser.[5,6] The Ar^+ ground state is obtained by removing one electron from the six electrons in the $3p$ outer shell of Ar. The excited $4s$ and $4p$ states are then obtained by promoting one of the remaining $3p^5$ electrons to the $4s$ or $4p$ state, respectively. As a consequence of interacting with the other $3p^4$ electrons, both the $4s$ and $4p$ levels, indicated as single levels in Fig. 10.6, actually consist of many sublevels.

The Ar ion is excited in a two-step process involving collisions with two distinct electrons. The first collision ionizes Ar, i.e., raises it to the Ar^+ ground state, while the second collision excites the Ar ion. Since the lifetime of the $4p$ level ($\sim 10^{-8}$ s, set by the $4p \rightarrow 4s$ radiative transition) is about 10 times longer than the radiative lifetime of the $4s \rightarrow 3p^5$ transition, excited Ar ions accumulate predominantly in the $4p$ level. This means that the $4p$ level can be used as the upper laser level for the $4p \rightarrow 4s$ laser transition and, according to Eq. (7.3.1), cw laser action can be achieved. Note that excitation of the Ar ion can lead to ions in the $4p$ state by three distinct processes (see Fig. 10.6): (a) Direct excitation to the $4p$ level starting from the Ar^+ ground level; (b) excitation to higher lying states followed by radiative decay to the $4p$ level; (c) excitation to metastable levels followed by a third collision, leading to excitation to the $4p$ state. Considering, for simplicity, only the first two processes, one sees that the pumping process to the upper state is expected to be proportional to the square of the discharge current density. In fact, since the

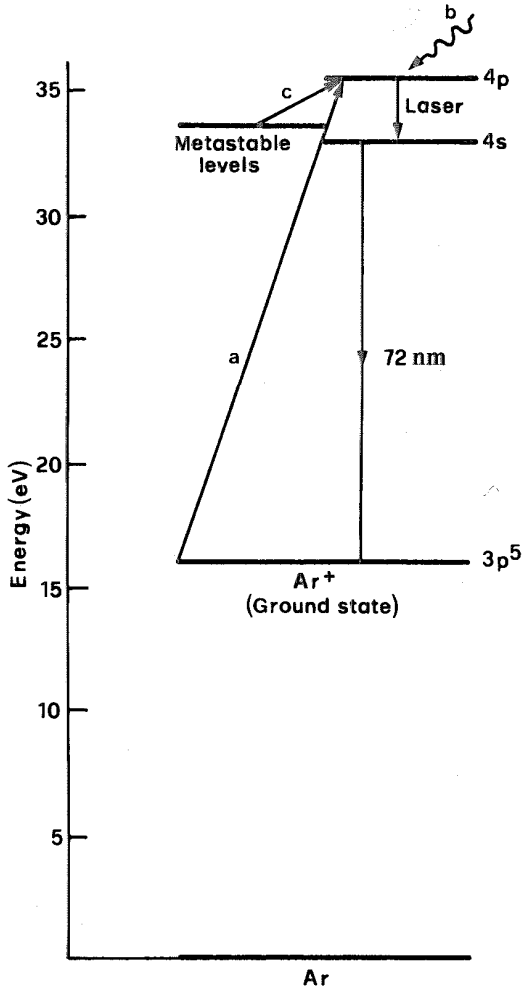

FIG. 10.6. Energy levels of Ar relevant for laser action.

first two processes involve a two-step electron collision, the rate of upper state excitation, $(dN_2/dt)_p$, is expected to take the form

$$\left(\frac{dN_2}{dt}\right)_p \propto N_e N_i \cong N_e^2 \tag{10.2.3}$$

where N_e and N_i are the electron and ion density in the plasma, respectively ($N_e \cong N_i$ in the positive column of the plasma). Since the electric field of the discharge is independent of the discharge current, the drift velocity v_{drift} is also independent of the discharge current. From the standard equation $J = ev_{drift}N_e$ one then sees that the electron density N_e is proportional to the discharge current density and, from Eq. (10.2.3), it follows that $(dN_2/dt)_p \propto J^2$. Laser pumping thus increases rapidly with current density, so high-current densities ($\sim$1 kA/cm^2) are required if the, inherently inefficient, two-step processes are to pump enough ions into the upper state. This may explain why the first operation of an Ar^+ laser occurred 3 years after the first He-Ne laser.[7]

From the preceding discussion we expect laser action, in an Ar laser, to occur on the $4p \rightarrow 4s$ transition. Since both the $4s$ and $4p$ levels actually consist of many sublevels, the argon laser oscillates on many lines; the most intense are in the green ($\lambda = 514.5$ nm) and blue ($\lambda = 488$ nm). From spectral measurements of the spontaneously emitted light, the

Doppler linewidth $\Delta\nu_0^*$ of, e.g., the green transition, is found to be ~ 3.5 GHz. From Eq. (2.5.18), this implies an ion temperature of $T \cong 3000$ K. The ions are therefore very hot, a result of ion acceleration by the electric field of the discharge. Table 10.1 summarizes relevant spectroscopic properties of the Ar ion green laser transition.

Figure 10.7 shows a schematic diagram of a high-power (> 1 W) argon laser. Both the plasma current and the laser beam are confined by metal disks (of tungsten) inserted into a larger bore tube of ceramic material (BeO). This, thermally conductive and resistant, metal-ceramic combination is necessary to ensure good thermal conductivity of the tube and, at the same time, to reduce erosion problems arising from the high ion temperature. The diameter of the central holes in the disks is kept small (~2 mm) to confine oscillation to a TEM_{00} mode (long radius of curvature mirrors are commonly used for the resonator) and to reduce the total current required.

A problem arises in argon lasers from the cataphoresis of argon ions. Due to the high-current density, in fact, a substantial migration of Ar ions occurs toward the cathode, where they are neutralized on combining with electrons emitted by the cathode surface.* Thus neutral atoms tend to accumulate at this electrode, with a corresponding reduction in Ar pressure, in the discharge capillary, below its optimum value. To overcome this problem, off-center holes are also made in the disk to provide return paths for the atoms from cathode to anode, by diffusion. The holes are arranged so that no current flows along this return path because longer path lengths are involved compared to that of the central path.

The inner ceramic tube is water cooled to remove the large amount of heat that it is inevitably dissipated in the tube (some kW/m). Note also that a static magnetic field is also applied in the discharge region, parallel to the tube axis, by a solenoid. With this arrangement, the Lorentz force makes electrons rotate around the tube axis, thus reducing the rate of electron diffusion to the walls. This increases the number of free electrons at the center of the tube, thereby increasing the pump rate. This may explain the observed increase in output power when a magnetic field is applied. By confining charges toward the center of the tube, the magnetic field also alleviates the problem of wall damage (mostly occurring at holes in the tungsten disks). Note that, for high-power lasers (>1 W), laser mirrors are mounted externally to the laser tube to reduce degradation of mirror coatings due to the intense vuv radiation emitted by the plasma.

* Referring to Sect. 6.4.4., we recall that direct electron-ion recombination cannot occur in the discharge volume, since the process cannot simultaneously satisfy both energy and momentum conservation. Electron-ion recombination can therefore occur only in the presence of a third partner, e.g., at the tube walls or at the cathode surface.

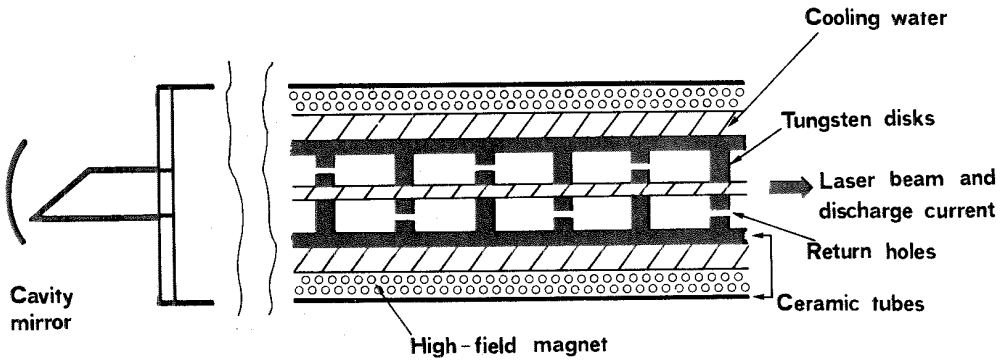

FIG. 10.7. Schematic diagram of a high-power water-cooled Ar^+ laser tube.

For lower power lasers (<1 W), the laser tube is often simply made of a block of ceramic (BeO) provided with a central hole for the discharge current. In this case, no magnetic field is applied, the tube is air cooled, and the mirrors are directly sealed to the ends of the tube as in a He-Ne laser.

Water-cooled argon lasers are commercially available with power ranging from 1 to 20 W, operating on both blue and green transitions simultaneously or, by using the configuration in Fig. 7.16b, operating on a single transition. Air-cooled argon lasers, of lower power (~100 mW) and much simpler design, are also commercially available. In both cases, once above threshold, output increases rapidly with current density ($\propto J^2$), since, in contrast to the behavior of He-Ne lasers, no saturation of the upper-state population occurs. Laser efficiency is however very low ($<10^{-3}$), because the laser quantum efficiency is rather low (~7.5%; see Fig. 10.6) and electron impact excitation involves many levels that are not effectively coupled to the upper laser level. Argon lasers are often operated in a mode-locked regime using an acousto-optic modulator. In this case, fairly short mode-locked laser pulses (~150 ps) are achievable by virtue of the relatively large transition linewidth (~3.5 GHz), which is inhomogeneously broadened.

Argon lasers are widely used in ophthalmology (particularly to treat diabetic retinopathy) and in the field of laser entertainment (laser light shows). Argon lasers are also widely used to study light-matter interaction (particularly in mode-locked operation) and also as a pump for solid-state lasers (particularly Ti:sapphire) and dye lasers. In many of these applications, argon lasers are now superseded by cw diode-pumped Nd:YVO_4 lasers, in which a green beam, $\lambda = 532$ nm, is produced by intracavity second harmonic generation. Lower power Ar lasers are extensively used in high-speed laser printers and cell cytometry.

10.2.2.2. He-Cd Laser

Figure 10.8 shows the energy levels in the He-Cd system that are relevant for laser action, where, again, level labeling follows Russell–Saunders notation. Pumping of Cd^+ upper laser levels ($^2D_{3/2}$ and $^2D_{5/2}$) is achieved with the help of He in the Penning ionization process. This process can be written in the general form

$$A^* + B \rightarrow A + B^+ + e \tag{10.2.4}$$

where the ion B^+ may or may not be left in an excited state. Of course, the process occurs only if the excitation energy of the excited species A^* is greater than or equal to the ionization energy of species B (plus the excitation energy of B^+, if the ion is left in an excited state). Note that, unlike near-resonant energy transfer, Penning ionization is a nonresonant process; any surplus energy is, in fact, released as kinetic energy of the ejected electron. In the case of the He-Cd system, the 2^1S and 2^3S metastable states of He act as the species A^* in Eq. (10.2.4); upon collision, this excitation energy is given up to ionize the Cd atom and excite the Cd^+ ion. Although the process is not resonant, it has been found that the rate of excitation to the D states is about three times larger than that to the P states.*

* According to, e.g., Eq. (2.6.2), the rate of excitation k_{A^*B} of the general process (10.2.4) can be defined by the relation $(dN/dt)_{AB^+} = k_{A^*B} N_{A^*} N_B$, where $(dN/dt)_{AB^+}$ is the number of species A and B^+ produced, per unit volume per unit time, and N_{A^*} and N_B are the concentrations of the colliding partners.

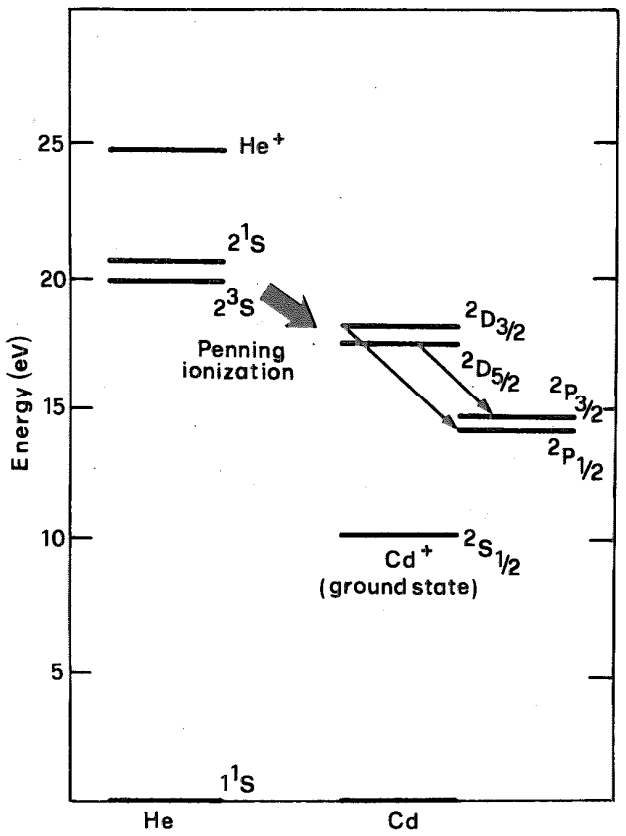

FIG. 10.8. Relevant energy levels in the He-Cd laser.

More importantly, however, the lifetime of the D states ($\sim 0.1\,\mu$s) is much longer than the lifetime of the P states (~ 1 ns). Population inversion between the D and P states can therefore be readily produced, so cw laser action can be achieved. Indeed, in accordance with the selection rule $\Delta J = 0, \pm 1$, laser action is obtained on the $^2D_{3/2} \rightarrow {}^2P_{1/2}$ ($\lambda = 325$ nm, uv) and the $^2D_{5/2} \rightarrow {}^2P_{3/2}$ ($\lambda = 416$ nm, blue) lines. The Cd^+ ion then drops to its $^2S_{1/2}$ ground state by radiative decay.

A typical construction for the He-Cd laser is in the form of a tube, terminated by two Brewster's angle windows, with the two laser mirrors mounted separated from the tube. In one possible arrangement, the tube, which is filled with helium, also has a small reservoir containing the Cd metal, located near the anode. The reservoir is raised to a high enough temperature ($\sim 250\,^\circ$C) to produce the desired vapor pressure of Cd atoms in the tube. The discharge itself then produces enough heat to prevent vapor condensation on the tube walls along the discharge region. Due to ion cataphoresis, however, ions migrate to the cathode where they recombine with electrons emitted by the cathode. Neutral Cd atoms then condense around the cathode region, where there is no discharge and the temperature is low. The net result is a continuous flow of metal vapor from the anode to the cathode. Therefore, a sufficient supply of Cd (~ 1 g per 1000 h) must be provided for long-term laser operation.

He-Cd lasers can give output powers of 50–100 mW, which places these lasers in an intermediate position between red He-Ne lasers (a few milliwatts) and Ar^+ lasers (a few watts). Thus, He-Cd lasers are used for many applications where a blue or uv beam of moderate power is required (e.g., high-speed laser printers, holography, cell cytometry, fluorescence analysis of biological specimens).

10.2.3. Molecular Gas Lasers

These lasers exploit transitions between the energy levels of a molecule. Depending on the type of transition involved, molecular gas lasers belong to one of the following categories: (1) *Vibrational-rotational lasers*, which use transitions between vibrational levels of the same electronic state (the ground state), so the energy difference between levels falls in the middle-to far-infrared (2.5–300 μm). By far the most important example of this category is the CO_2 laser oscillating at either 10.6 or 9.6 μm. Other noteworthy examples are the CO laser ($\lambda \cong 5\,\mu$m) and the HF chemical laser ($\lambda \cong 2.7-3.3\,\mu$m). (2) *Vibronic lasers*, which use transitions between vibrational levels of different electronic states. In this case the oscillation wavelength generally falls in the uv region. The most notable example of this laser category is the nitrogen laser ($\lambda = 337$ nm). A special class of lasers, that can be included here is the excimer laser. These lasers involve transitions between different electronic states of special molecules (excimers) with corresponding emission wavelengths generally in the uv. Excimer lasers, however, involve not only transitions between bound states (bound-bound transitions) but also, and actually more often, transitions between a bound upper state and a repulsive ground state (bound-free transitions). It is more appropriate therefore to treat these lasers as a category of their own. (3) *Pure rotational lasers*, which use transitions between different rotational levels of the same vibrational state (usually an excited vibrational level of the ground electronic state). The corresponding wavelength falls in the far infrared (25 μm–1 mm). Since pure rotational lasers are relatively less important than other laser types, we do not discuss them in the sections that follow. We point out here that laser action is more difficult to achieve with this type of laser, since the relaxation between rotational levels is generally very rapid. Therefore, these lasers are usually pumped optically, using the output of another laser as the pump (commonly a CO_2 laser). Optical pumping excites the given molecule (e.g., CH_3F, $\lambda = 496\,\mu$m) to a rotational level belonging to some vibrational state above the ground level. Laser action then takes place between rotational levels of this upper vibrational state.

10.2.3.1. CO_2 Laser

As the active medium, these lasers use a suitable mixture of CO_2, N_2, and He. Oscillation takes place between two vibrational levels of the CO_2 molecule, while N_2 and He greatly improve the efficiency of laser action. The CO_2 laser is actually one of the most powerful lasers (output powers of more than 100 kW have been demonstrated from a CO_2 gas-dynamic laser) and one of the most efficient (15–20% slope efficiency).[8,9]

Figure 10.9 shows the relevant vibrational energy levels for the electronic ground states of the CO_2 and N_2 molecules. The N_2 molecule, being diatomic, has only one vibrational mode; its lowest two energy levels ($v = 0, v = 1$) are indicated in the figure. Energy levels for CO_2 are more complicated, since CO_2 is a linear triatomic molecule. In this case there are three nondegenerate modes of vibration (Figure 10.10): Symmetric stretching, bending, and asymmetric stretching. The oscillation behavior and corresponding energy levels are therefore described by means of three quantum numbers n_1, n_2, and n_3, which give the number of quanta in each vibrational mode. This means that, apart from zero-point energy, the energy of the level is given by $E = n_1 h\nu_1 + n_2 h\nu_2 + n_3 h\nu_3$, where ν_1, ν_2 and ν_3 are the

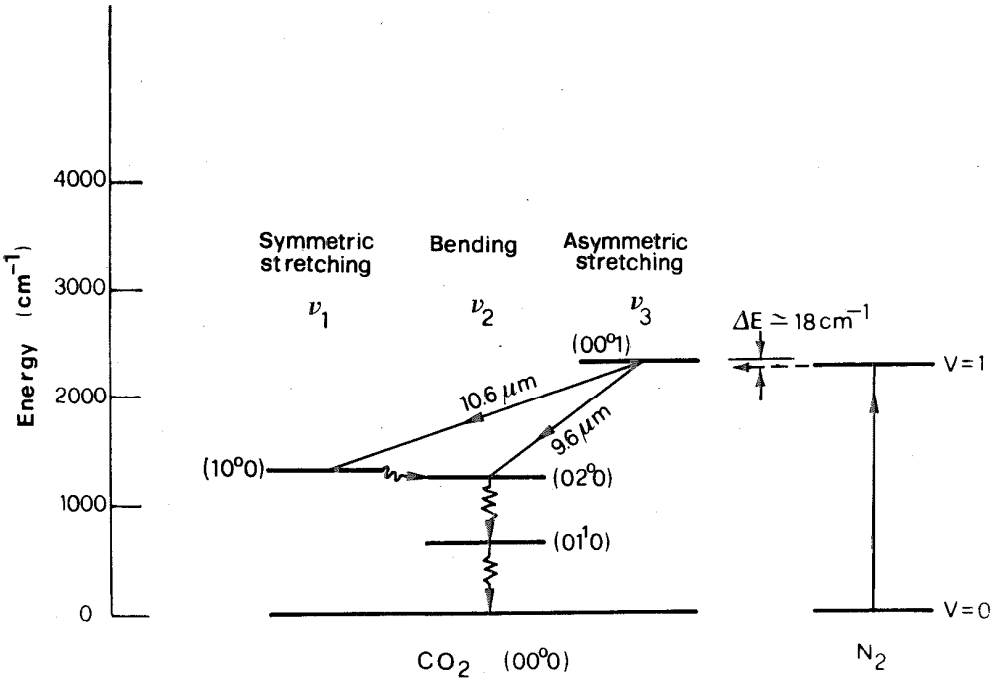

FIG. 10.9. The lowest vibrational levels of the ground electronic state of a CO_2 molecule and an N_2 molecule. (For simplicity, rotational levels are not shown.)

resonance frequencies of the three modes. For example, the 01^10 level* corresponds to an oscillation where there is one vibrational quantum in mode 2. Since mode 2 has the smallest force constant of the three modes (the vibrational motion is transverse), this level has the lowest energy. Laser action occurs between the 00^01 and 10^00 levels ($\lambda \cong 10.6\,\mu m$), although it is also possible to obtain oscillation between 00^01 and 02^00 ($\lambda \cong 9.6\,\mu m$).

Pumping the upper 00^01 laser level is efficiently achieved by the following processes: (1) Direct Electron Collisions. The main direct collision considered is obviously as follows: $e + CO_2(000) \rightarrow e + CO_2(001)$. The electron collision cross section for this process is very large and appreciably larger than those for excitation to both the 100 and 020 level—probably because the transition $000 \rightarrow 001$ is optically allowed whereas, for instance, the transition $000 \rightarrow 100$ is not. Note also that direct electron impact can also lead to excitation of upper $(0, 0, n)$ vibrational levels of the CO_2 molecule. However, the CO_2 molecule

* The superscript (denoted by l) on the bending quantum number arises because the bending vibration is in this case doubly degenerate. In fact, it can occur in both the plane of Fig. 10.10 and in the orthogonal plane. A bending vibration therefore consists of a suitable combination of these two vibrations. More precisely, $l\hbar$ gives the angular momentum of this vibration about the axis of the CO_2 molecule. For example, in the 02^00 state ($l = 0$), the two degenerate vibrations combine to give an angular momentum $l\hbar = 0$.

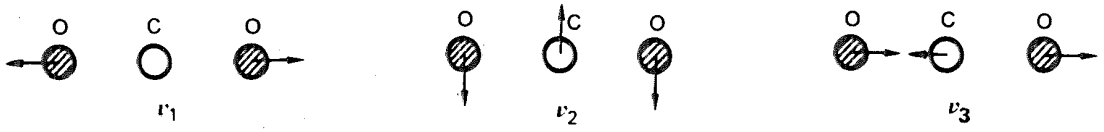

FIG. 10.10. Three fundamental vibration modes for a CO_2 molecule: (ν_1) symmetric stretching, (ν_2) bending, (ν_3) asymmetric stretching.

rapidly relaxes from these upper states to the (001) state by near-resonant collisions of the type:*

$$CO_2(0, 0, n) + CO_2(0, 0, 0) \rightarrow CO_2(0, 0, n-1) + CO_2(0, 0, 1) \tag{10.2.5}$$

This process tends to degrade all excited molecules to the (0, 0, 1) state. Note that, since most molecules in a CO_2 laser mixture are in fact in the ground state, collision of an excited with an unexcited molecule constitutes the most likely collisional event. (2) Resonant Energy Transfer from N_2 Molecule. This process is also very efficient due to the small energy difference between excited levels of the two molecules ($\Delta E = 18\,\text{cm}^{-1}$). In addition, the excitation of N_2 from the ground level to the $v = 1$ level is a very efficient process, and the $v = 1$ is metastable. Transition $1 \rightarrow 0$ is in fact electric-dipole-forbidden since, by virtue of its symmetry, a N-N molecule, using the same isotope for the two nitrogen atoms, cannot have a net electric dipole moment. The higher vibrational levels of N_2 are also closely resonant ($\Delta E < kT$) with the corresponding CO_2 levels (up to 00^05), and transitions between excited levels, $00n$, and the 001 level of the CO_2 molecule occur rapidly through the process indicated in Eq. (10.2.5).

The next point to consider is the decay of both upper and lower laser levels. Note that, although transitions $00^01 \rightarrow 10^00, 00^01 \rightarrow 02^00, 10^00 \rightarrow 01^00$, and $02^00 \rightarrow 01^00$ are optically allowed, the corresponding decay times τ_{sp}, for spontaneous emission, are very long ($\tau_{sp} \propto 1/v^3$). The decay of these various levels is therefore determined essentially by collisions. Accordingly, the decay time τ_s of the upper laser level can be obtained from a formula of the type

$$\left(\frac{1}{\tau_s}\right) = \sum a_i p_i \tag{10.2.6}$$

where p_i are partial pressures and a_i are rate constants corresponding to gases in the discharge. Taking for example the case of a total pressure of 15 Torr (in a 1:1:8 CO_2:N_2:He partial-pressure ratio), one finds that the upper level has a lifetime $\tau_s \cong 0.4$ ms. Concerning the relaxation of the lower level, we begin by noting that the transition $100 \rightarrow 020$ is very rapid and it occurs even in an isolated molecule. In fact, the energy difference between the two levels is much smaller than kT. Furthermore, a coupling between the two states is present (Fermi resonance) because a bending vibration tends to induce a change of distance between the two oxygen atoms (i.e., to induce a symmetric stretching). Levels 10^00 and 02^00 are then effectively coupled to the 01^10 level by the two near-resonant collision processes involving CO_2 molecules in the ground state (VV relaxation), as follows:

$$CO_2(10^00) + CO_2(00^00) \rightarrow CO_2(01^10) + CO_2(01^10) + \Delta E \tag{10.2.7a}$$

$$CO_2(02^00) + CO_2(00^00) \rightarrow CO_2(01^10) + CO_2(01^10) + \Delta E' \tag{10.2.7b}$$

* Relaxation processes in which vibrational energy is given up as vibrational energy of another like or unlike molecule are usually referred to as *VV relaxations*.

The two processes have a very high probability, since ΔE and $\Delta E'$ are much smaller than kT. It follows, therefore, that the three levels 10^00, 02^00, and 01^10 reach the thermal equilibrium in a very short time.

We are now left with the decay from the 01^10 to the ground level 00^00. If this decay were slow, it would lead to an accumulation of molecules in the 01^10 level during laser action. This would in turn produce an accumulation in the 10^00 and 02^00 levels since these are in thermal equilibrium with the 01^10 level. Thus the decay process would slow down on all three levels, i.e., the $(01^10) \rightarrow (00^00)$ transition would constitute a bottleneck in the overall decay process. It is therefore important to consider the lifetime of the 01^10 level. Note that, since the transition $01^10 \rightarrow 00^00$ is the least energetic transition in any of the molecules in the discharge, relaxation from the 01^10 level can occur only by transferring this vibrational energy to translational energy of the colliding partners (*VT relaxation*). According to the theory of elastic collisions, energy is most likely to be transferred to lighter atoms, i.e., to helium in this case. This means that the lifetime is again given by an expression of the general form of Eq. (10.2.6), where the coefficient a_i, for He, is much larger than that of the other species. For the same partial pressures considered in this example, one obtains a lifetime of about 20 μs. It follows from the preceding discussion that this is also the value of the lifetime of the lower laser level. Therefore, due to the much larger value of the upper state lifetime, population accumulates in the upper laser level, so the condition for cw laser action is also fulfilled. Note that He has another valuable effect: Due to its high thermal conductivity, He helps keeping the CO_2 cool by conducting heat to the walls of the container. A low translational temperature for CO_2 is necessary to avoid populating the lower laser level by thermal excitation; energy separation between levels is in fact comparable to kT.

To summarize most preceding discussions, we can say that nitrogen helps producing a large population in the upper laser level while helium helps removing population from the lower laser level.

From the preceding considerations we see that laser action in a CO_2 laser may occur either on the $(00^01) \rightarrow (10^00)$ ($\lambda = 10.6$ μm) transition or on the $(00^01) \rightarrow (02^00)$ transition ($\lambda = 9.6$ μm). Since the first of these transitions has a greater cross section and both transitions share the same upper level, the $(00^01) \rightarrow (10^00)$ transition usually oscillates. To obtain oscillation on the 9.6-μm line, some appropriate frequency-selective device is placed in the cavity to suppress laser action on the line with highest grain. (The system in Fig. 7.16a is often used.)

So far we have ignored the fact that both upper and lower laser levels consist of many closely spaced rotational levels. Accordingly, laser emission may occur on several equally spaced rotational-vibrational transitions belonging to either P or R branches (see Fig. 3.7), with the P branch exhibiting the largest gain. To complete our discussion we must also consider that, as a consequence of the Boltzmann distribution between rotational levels, the $J' = 21$ rotational level of the upper 00^01 state is the most heavily populated (see Fig. 10.11).* Laser oscillation then occurs on the rotational vibrational transition with the largest gain i.e., originating from the most heavily populated level. This happens because, in a CO_2 laser, the thermalization rate among rotational levels ($\sim 10^7$ s^{-1} Torr^{-1}) is faster than the rate of decrease in population (due to stimulated emission) of the rotational level from which

* By reason of symmetry, only levels with odd values of J are occupied in a CO_2 molecule.

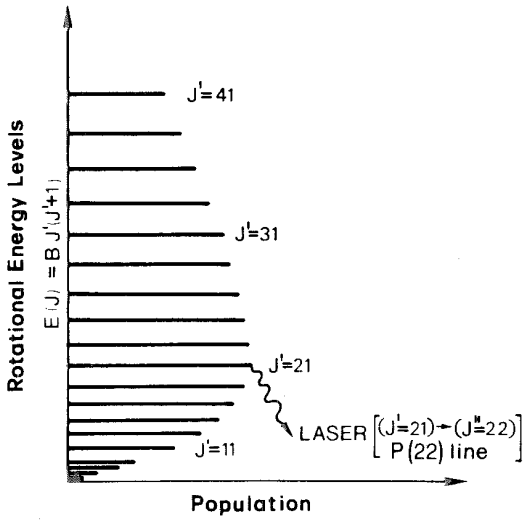

FIG. 10.11. Relative population of rotational levels in the upper laser level of CO_2.

laser emission occurs. Therefore, the entire population of rotational levels contributes to laser action on the rotational level with the highest gain. Consequently, and as a conclusion to this discussion, laser action in a CO_2 laser normally occurs on the $P(22)$ [i.e., $(J' = 21) \rightarrow (J'' = 22)$] line of the $(00^01) \rightarrow (10^00)$ transitions. Other lines of the same transition as well as lines belonging to the $(00^01) \rightarrow (02^00)$ transition (the separation between rotational lines in a CO_2 laser is about $2\,cm^{-1}$) can be selected with, e.g., the scheme in Fig. 7.16a.

A major contribution to laser linewidth in a CO_2 laser comes from the Doppler effect. Compared with, e.g., a visible gas laser, the corresponding value of the Doppler linewidth is however rather small (about 50 MHz) due to the low frequency ν_0 of the laser transition (see Example 3.2). Collision broadening is, however, not negligible (see Example 3.3), and it actually becomes the dominant line-broadening mechanism for CO_2 lasers operating at high pressures ($p > 100$ Torr).

Based on their constructional design, CO_2 lasers fall into the following categories: Lasers with slow axial flow, sealed-off lasers, waveguide lasers, lasers with fast axial flow, diffusion-cooled lasers, transverse-flow lasers, transversely excited atmospheric pressure (TEA) lasers, and gas dynamic lasers. We do not consider the gas dynamic laser here, since its operating principle was described in Sect. 6.1. Before considering the other categories, we point out that, although these lasers differ from one another as far as many of their operating parameters are concerned (e.g., output power), they all share a very important characteristic feature, namely, high slope efficiency (15–25%). This high efficiency results from the high laser quantum efficiency (~40%; see Fig. 10.9) and the highly efficient pumping processes that occur in a CO_2 laser at the optimum electron temperature of the discharge (see Fig. 6.28).

(a) Lasers with Slow Axial Flow. Operation of the first CO_2 laser was achieved in a laser of this type (C. K. N. Patel, 1964[10]). The gas mixture is flowed slowly along the laser tube (see Fig. 10.12) simply to remove dissociation products, in particular CO, that otherwise would contaminate the laser. Heat removal is provided by radial heat diffusion to the tube walls (usually made of glass), which are cooled externally by a suitable coolant (usually water). An internal mirror arrangement is often used, and, in the design of Fig. 10.12, one of the metal mounts holding the cavity mirrors must be held at a high voltage.

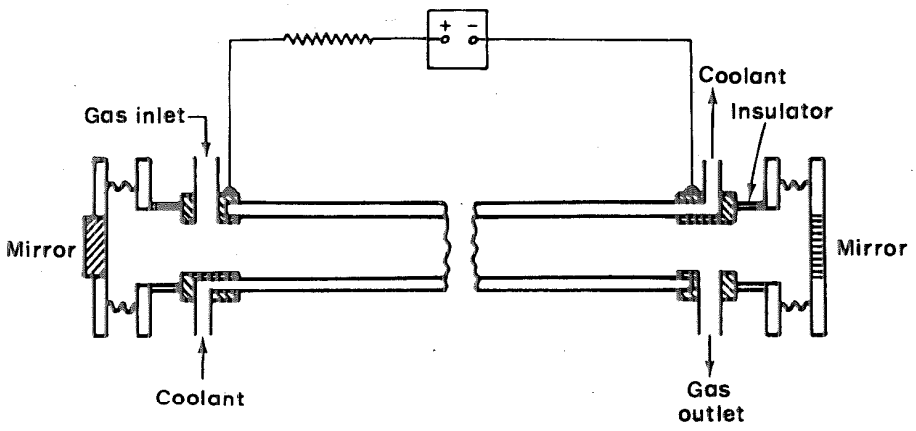

FIG. 10.12. Schematic diagram of a CO_2 laser with longitudinal gas flow.

One of the main limitations of this laser arises from the maximum laser output power, per unit length of the discharge (50–60 W/m), which can be obtained, independently of tube diameter. In fact, from Eq. (6.4.24), we find that the number of molecules pumped into the upper laser level per unit volume and unit time can be written as

$$\left(\frac{dN_2}{dt}\right)_p = N_t \frac{J}{e}\left(\frac{\langle v\sigma\rangle}{v_{drift}}\right) \tag{10.2.8}$$

where: J is the current density; σ is a suitable electron impact cross section, which takes into account both direct and energy transfer excitations; N_t is the total CO_2 ground-state population. For pump rates well above threshold, output power P is proportional to $(dN_2/dt)_p$ and the volume of the active medium V_a. From Eq. (10.2.8) we can therefore write

$$P \propto JN_tV_a \propto JpD^2l \tag{10.2.9}$$

where D is the diameter of the active medium, l its length, and p the gas pressure. Under optimum operating conditions we now have the following: (1) The product pD must be constant ($\sim$22.5 Torr × cm, e.g., 15 Torr for $D = 1.5$ cm) to keep the discharge at the optimum electron temperature. (2) Due to the thermal limitations imposed by the requirement of heat conduction to the tube walls, an optimum value of the current density exists, and this value is inversely proportional to the tube diameter D. The existence of an optimum value of J is understood when we observe that excessive current density leads to excessive heating of the mixture (even with an efficiency of 20%, some 80% of the electrical power is dissipated in the discharge as heat), with resulting thermal population in lower laser levels. The fact that the optimum value of J is inversely proportional to D is understood when we realize that, as diameter is increased, generated heat has more difficulty in escaping to the walls. From this discussion we conclude that, under optimum conditions, both J and p are inversely proportional to D; hence, from Eq. (10.2.9), the optimum value of P is found to be only proportional to the tube length l. CO_2 lasers with slow axial flow and relatively low power (50–100 W) are widely used for laser surgery, resistor trimming, cutting ceramic plates for the electronics industry, and welding thin metal sheets (<1 mm).

(b) Sealed-off Lasers. If the flow of the gas mixture is stopped in the arrangement shown in Fig. 10.12, laser action ceases in a few minutes. This arises because chemical

reaction products formed in the discharge (CO in particular) are no longer removed but instead are adsorbed on the walls of the tube or react with the electrodes, thus upsetting the CO_2–CO–O_2 equilibrium. Ultimately, this leads to dissociation of a large fraction of CO_2 molecules in the gas mixture. For a non-circulating sealed-off laser, some kind of catalyst must be present in the gas tube to promote regeneration of CO_2 from CO. A simple way of achieving this involves adding a small amount of H_2O (1%) to the gas mixture. This leads to CO_2 regeneration, probably through the reaction

$$CO^* + OH \rightarrow CO_2^* + H \tag{10.2.10}$$

involving vibrationally excited CO and CO_2 molecules. The relatively small amount of water vapor required, may be added in the form of hydrogen and oxygen gas. Actually, since oxygen is produced during the dissociation of CO_2, only hydrogen needs be added. Another way of inducing the recombination reaction uses a hot (300°C) Ni cathode, which acts as a catalyst. With these techniques, lifetimes for sealed-off tubes in excess of 10,000 hours have been demonstrated.

Sealed-off lasers have produced output powers per unit length of ~60 W/m, i.e., comparable to those of longitudinal flow lasers. Low-power (~1 W) sealed-off lasers of short length (and hence operating on a single mode) are often used as local oscillators in optical heterodyne experiments. Sealed-off CO_2 lasers of somewhat higher power (~10 W) are attractive for laser microsurgery and micromachining.

(c) Capillary Waveguide Lasers. If the diameter of the laser tube in Fig. 10.12 is reduced to around a few millimeters (2–4 mm), a situation is reached where laser radiation is guided by the inner walls of the tube. Such waveguide CO_2 lasers have a low diffraction loss. Tubes of BeO or SiO_2 were found to give the best performance. Due to the small bore diameter of a waveguide CO_2 laser, the pressure of the gas mixture must be considerably increased (100–200 Torr); with this increase in pressure, the laser gain per unit length is correspondingly increased. Thus, one can manufacture short CO_2 lasers ($L < 50$ cm) without facing the difficult requirement of reducing cavity losses; however, the power available per unit length of the discharge suffers the same limitation discussed earlier for the slow axial flow laser (~50 W/m). Therefore, waveguide CO_2 lasers are particularly useful when short and compact CO_2 lasers of low power ($P < 30$ W) are needed (e.g., for laser microsurgery).

To fully exploit their compactness, these lasers usually operate as sealed-off devices. The laser configuration may resemble that in Fig. 10.12, where discharge current flows longitudinally along the laser tube, or that in Fig. 10.13, where the current (usually provided by an rf source) flows transversely across the tube. Since $\mathscr{E}/p$ must be constant, then, for a given value of discharge electric field $\mathscr{E}$, the transverse pumping configuration offers a significant advantage over longitudinal pumping due to its much reduced (one to two orders of magnitude) electrode voltage. Radiofrequency ($\nu \cong 30$ MHz) excitation presents many advantages,[11] the most important of which are perhaps: (1) Avoiding permanent anodes and cathodes, which eliminates the associated plasmo-chemical problems at the cathode. (2) Creating a stable discharge with the help of simple nondissipative elements (e.g., a dielectric slab) in series in the discharge circuit (see, e.g., Fig. 6.21). As a result of these various advantages, rf discharge lasers are increasingly being used not only for waveguide lasers but also for fast axial flow lasers and transverse flow lasers, which we consider next. The laser

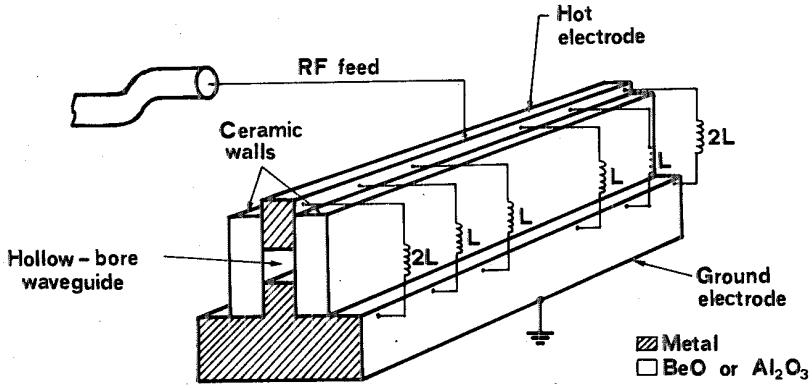

FIG. 10.13. Schematic diagram of an rf-excited waveguide CO_2 laser.

tube of a waveguide CO_2 laser is either not cooled or, for the highest power units, cooled by forced air.

(d) Lasers with Fast Axial Flow. To overcome the output power limitation of a CO_2 laser with slow axial flow, as discussed with the help of Eqs. (10.2.8) and (10.2.9), a possible solution, and a very interesting one, involves flowing the gas mixture through the tube at a very-high supersonic speed (about 50 m/s). In this case the heat is removed simply by removing the hot mixture from the discharge region; the mixture is then cooled outside the tube by a suitable heat exchanger and then returned to the discharge region, as shown in Fig. 10.14. A dc longitudinal discharge or, more frequently, an rf transverse discharge across the glass tube (see Fig. 6.21) can be used to provide excitation of each of the two laser tubes indicated in the figure. When operated in this way, there is no optimum for the current density, so the power actually increases linearly with J, resulting in much higher output powers per unit discharge length (~1 kW/m or even greater). Besides being cooled, the mixture is also passed, outside the laser tube, over a suitable catalyst to let CO recombine with O_2 and thus achieve the required regeneration of CO_2 molecules. (Some O_2 is already present in the mixture due to dissociation of the CO_2 in the discharge region.) In this way either completely sealed-off operation can be achieved or at least replenishment requirements for the mixture are kept to a minimal level. Fast axial flow CO_2 lasers with high power (1–3 kW) are now commonly used for many material working applications, in particular for cutting metals (with a thickness of up to a few millimeters).

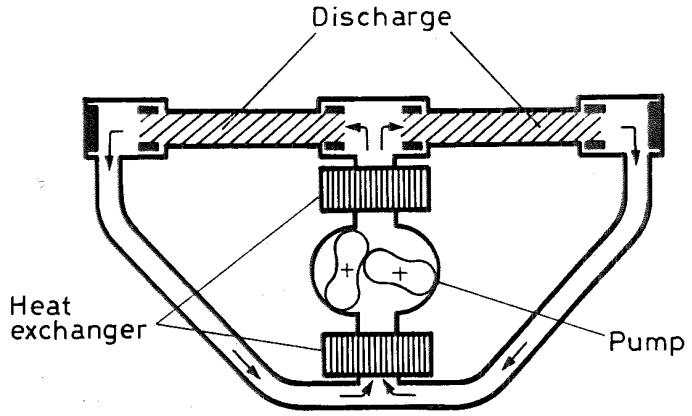

FIG. 10.14. Schematic diagram of a fast axial flow CO_2 laser.

(e) Diffusion-Cooled Lasers. An alternative approach to circumventing the power limitation of a slow axial flow laser is to use a transverse discharge with electrodes spacing d much smaller than the electrode width W (slab geometry, see Fig. 10.15a). In this case, the gas mixture is very effectively cooled by one-dimensional heat flow toward the electrodes, which are water cooled. The laser output power scales, in this case, as $P_{out} = (CWl)/d$, where C is a constant ($C \cong 50\,\mathrm{W/m}$) and l is the electrode length.[12] Thus, for a given electrode spacing, output power scales as the electrode area Wl rather than electrode length, as in, e.g., CO_2 lasers with slow axial flow [see Eq. (10.2.9)]. For sufficiently small electrode spacing, large powers per unit electrode area can then be obtained [e.g., $(P_{out}/Wl) \cong 20\,\mathrm{kW/m^2}$ for $d = 3\,\mathrm{mm}$]. Instead of the slab-geometry configuration in Fig. 10.15a, the annular-geometry configuration in Fig. 10.15b can also be used; the latter configuration is technically more complicated but allows more compact devices to be achieved.

It should be stressed that the preceding results hold if the electrode width is appreciably larger (by approximately an order of magnitude) than the electrode spacing. To produce a good-quality discharge and an output beam with good divergence properties, from a gain medium with such a pronounced elongation, poses some difficult problems. Stable and spatially uniform discharges can however be obtained by exploiting the advantages of rf excitation. For electrode spacings on the order of a few millimeters, on the other hand, the laser beam is guided in the direction normal to the electrode surface, and propagates freely in the direction parallel to this surface. To obtain output beams with good quality, hybrid resonators, which are stable in a direction perpendicular to the electrodes and unstable parallel to the electrodes, have been developed.[13]

Compact, diffusion-cooled slab-geometry CO_2 lasers with output powers of $\sim 2.5\,\mathrm{kW}$ are now commercially available with the potential for a large impact in material working applications.

(f) Transverse-Flow Lasers. Another way of circumventing the power limitations of a slow axial flow laser involves flowing the gas mixture perpendicular to the discharge (Fig. 10.16). If the flow is fast enough, then, as in the case of fast axial flow lasers, heat is removed by convection rather than diffusion to the walls. Saturation of output power versus discharge current does not occur then, and, as in the case of fast axial flow, very high output powers per unit discharge length can be obtained (a few kW/m; see also Fig. 7.7). The optimum total pressure ($\sim$100 Torr) is now typically an order of magnitude greater than that of large-bore longitudinal-flow systems. The increase in total pressure p requires a corresponding increase in the electric field $\mathscr{E}$ in the discharge. In fact, for optimum operating

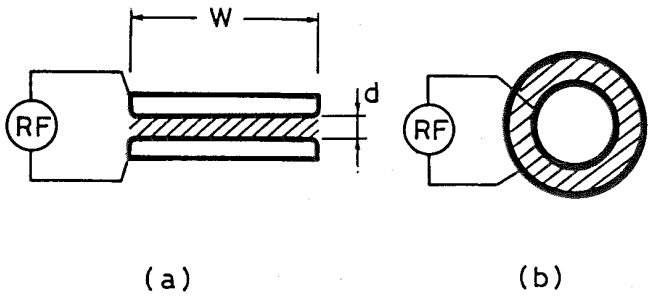

FIG. 10.15. Schematic diagram of a diffusion-cooled CO_2 laser using either (a) slab geometry or (b) an annular-geometry configuration.

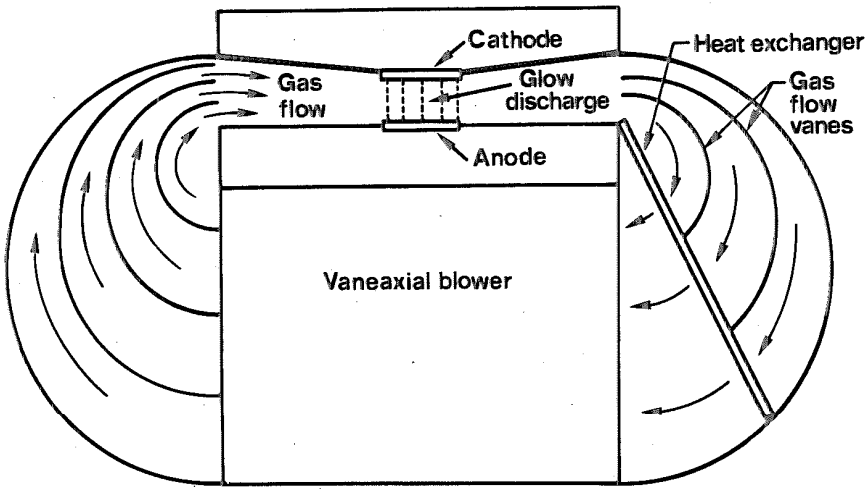

FIG. 10.16. Schematic diagram for a transverse-flow CO_2 laser.

conditions, the ratio $\mathscr{E}/p$ must remain approximately the same for all these cases, since this ratio determines the temperature of the discharge electrons [see Eq. (6.4.22)]. With this high value of electric field, a longitudinal-discharge arrangement, such as in Fig. 10.12, is impractical, since it requires very high voltages (100–500 kV for a 1-m discharge). For this reason, the discharge is usually applied perpendicular to the resonator axis (lasers with transverse electric field, i.e., TE lasers).

TE CO_2 lasers with fast transverse flow and high-output power (1–20 kW) are used in a great variety of metal-working applications (welding, surface hardening, surface metal alloying). Compared to fast axial flow lasers, these lasers are simpler devices given the reduced flow-speed requirement for transverse flow. However, the beam quality of fast axial flow lasers is considerably better, due to the cylindrical symmetry of their discharge current distribution, and this makes them particularly important for cutting applications.

(g) Transversely Excited, Atmospheric Pressure, Lasers. In a cw TE CO_2 laser, it is not easy to increase the operating pressure above ~100 Torr. Above this pressure and at the current densities normally used, glow discharge instabilities set in and cause the formation of arcs within the discharge volume. To overcome this difficulty, the voltage can be applied to the transverse electrodes in the form of a pulse. If the pulse duration is sufficiently short (a fraction of a microsecond), discharge instabilities have no time to develop, so the operating pressure can be increased up to and above atmospheric pressure. These lasers are therefore referred to as transversely excited at atmospheric pressure (TEA). These lasers produce a pulsed output and are capable of large output energies per unit discharge volume (10–50 J/liter). To avoid arc formation, some form of ionization (*preionization*) is also applied; the preionization pulse just precedes the main voltage pulse that produces gas excitation.

Figure 10.17 shows a configuration often used, where ionization is produced by the strong uv emission of a row of sparks running parallel to the tube length. The deep uv emission of these sparks produces the required ionization by both photoionization of gas constituents and uv-induced electron emission from the electrodes (*uv-preionization*). Other preionization techniques include using pulsed *e*-beam guns (*e-beam preionization*) and ionization by the corona effect (*corona preionization*). Once ionization within the whole volume of the laser discharge is produced, the fast switch (a hydrogen thyratron or a spark

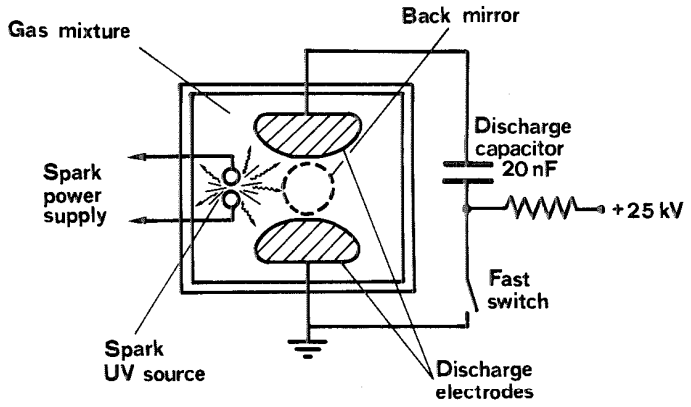

FIG. 10.17. Schematic diagram (*viewed along the laser axis*) of a CO_2 TEA laser. The laser uses uv radiation from several spark sources placed along the tube direction to provide gas preionization.

gap) is closed, so the main discharge pulse is passed through the discharge electrodes. Since the transverse dimensions of the laser discharge are usually large (a few centimeters), the two end mirrors are often chosen to give an unstable resonator configuration (positive-branch unstable confocal resonator; see Fig. 5.18b). For low-pulse repetition rates (~1 Hz), it is unnecessary to flow the gas mixture. For higher repetition rates, the gas mixture is flowed transversely to the resonator axis and cooled by a suitable heat exchanger; repetition rates up to a few kilohertz have been achieved in this way. Another interesting characteristic of these lasers is their relatively broad linewidth (~4 GHz at $p = 1$ atm, due to collision broadening). Thus optical pulses with less than 1-ns duration can be produced with mode-locked TEA lasers.

Transverse-flow CO_2 TEA lasers of relatively high repetition rate (~50 Hz) and relatively high average output power ($\langle P_{out} \rangle \cong 300$ W) are commercially available. Besides being used in scientific applications, these lasers find a number of industrial uses for material working applications where the pulsed nature of the beam presents some advantage (e.g., pulsed laser marking or pulsed ablation of plastic materials).

10.2.3.2. CO Laser

The second example of a gas laser using vibrational-rotational transitions that we will briefly consider is that of the CO laser. This laser has attracted considerable interest on account of its shorter wavelength ($\lambda \cong 5$ μm) than the CO_2 laser, combined with high efficiencies and high power. Output powers in excess of 100 kW and efficiencies in excess of 60% have been demonstrated;[14] however, to achieve this sort of performance, the gas mixture must be kept at cryogenic temperature (77–100 K). Laser action, in the 5-μm region, arises from several rotational-vibrational transitions [e.g., from $v'(11) \rightarrow v(10)$ to $v'(7) \rightarrow v(6)$ at $T = 77$ K] of the highly excited CO molecule.

Pumping of the CO vibrational levels is achieved by electron-impact excitation. Like the isoelectronic N_2 molecule, the CO molecule has an unusually large cross section for electron-impact excitation of its vibrational levels. Thus, nearly 90% of the electron energy in a discharge can be converted into vibrational energy of CO molecules. Another important feature of the CO molecule is that VV relaxation proceeds at a much faster rate than VT relaxation (which is unusually low). As a consequence of this, a non-Boltzmann population

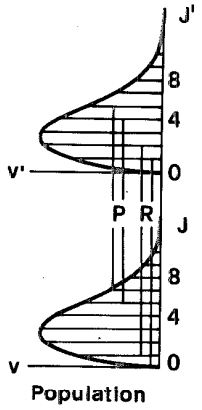

FIG. 10.18. Partial inversion between two vibrational transitions (v and v') with the same total population.

build-up in higher vibrational levels, by a process known as *anharmonic pumping*, plays a very important role.* Although this phenomenon does not allow total inversion in the vibrational population of a CO molecule, a situation known as *partial inversion* may occur. This is illustrated in Fig. 10.18 which indicates the rotational populations of two neighboring vibrational states. Although the total population for the two vibrational states is equal in the figure, an inversion exists for the two P transitions $[(J' = 5) \rightarrow (J = 6), (J' = 4) \rightarrow (J = 5)]$ and also for the two R-branch transitions indicated in the figure.

Under conditions of partial inversion, laser action can take place and a new phenomenon, called cascading, can then play an important role. Laser action, in fact, depopulates a rotational level of the upper state and populates a rotational level of the lower vibrational state. The latter level then accumulates enough population to result in population inversion with respect to a rotational level of a still lower vibrational state. At the same time, the rotational level of the upper state may become sufficiently depopulated to result in population inversion with respect to a rotational level of a still higher vibrational state. This cascading process, coupled with the very-low VT rate, results in most of the vibrational energy being extracted as laser output energy. Combined with the very high excitation efficiency, this accounts for the high efficiency of CO lasers. The low-temperature requirement arises from the need for very efficient anharmonic pumping. In fact, the overpopulation in high vibrational levels, compared to the Boltzman distribution, and hence the degree of partial inversion, increase rapidly with decreasing translational temperature.

As for CO_2 lasers, CO lasers have been operated with longitudinal flow, e-beam preionized pulsed TE, and gasdynamic excitation. The requirement of cryogenic temperatures has, so far, limited the commercial development of CO lasers. Recently, however, high-power ($P > 1$ kW) CO lasers, operating at room temperature while retaining a reasonably high slope efficiency (~10%), have been introduced commercially. These

* Anharmonic pumping arises from a collision of the type $CO(v = n) + CO(v = m) \rightarrow CO(v = n + 1) + CO(v = m - 1)$ with $n > m$. Because of anharmonicity (a phenomenon shown by all molecular oscillators), the separation between vibrational levels becomes smaller for levels higher up in the vibrational ladder (see also Fig. 3.1). This means that in a collision process of the type indicated above, with $n > m$, the total vibrational energy of the two CO molecules, after collision, is somewhat smaller than before collision. The collision process therefore has a greater probability of proceeding in this direction than the reverse direction. This means that the hottest CO molecule $[CO(v = n)]$ can ascend the vibrational ladder; this leads to a non-Boltzmann distribution of the population among the vibrational levels.

lasers are now under active consideration as a practical source for material-working applications.

10.2.3.3. Nitrogen Laser

As a particularly relevant example of vibronic lasers, we consider the N_2 laser.[15] This laser has its most important oscillation at $\lambda = 337$ nm (uv) and belongs to the category of self-terminating lasers.

Figure 10.19 shows the relevant energy level scheme for the N_2 molecule. Laser action takes place in the so-called second positive system, i.e., in the transition from the $C^3\Pi_u$ state (henceforth called the C state) to the $B^3\Pi_g$ state (B state).* Excitation of the C state is believed to arise from electron-impact collisions with ground-state N_2 molecules. Since both C and B states are triplet states, transitions from the ground state are spin-forbidden. On the basis of the Franck–Condon principle, we can however expect the excitation cross section due to em wave interaction, and hence due to the electron impact, to the $v = 0$ level of the C state, to be larger than that to the $v = 0$ level of the B state. The potential minimum of the B state is in fact shifted (relative to the ground state) to a larger internuclear separation than that of the C state. The lifetime (radiative) of the C state is 40 ns, while the lifetime of the B state is 10 μs. Clearly the laser cannot operate cw, since Eq. (7.3.1) is not satisfied. The laser can however be excited on a pulsed basis provided the electrical pulse is appreciably shorter than 40 ns. Laser action takes place predominantly on several rotational lines of the $v''(0) \rightarrow v'(0)$ transition ($\lambda = 337.1$ nm) because this transition exhibits the largest stimulated emission cross section. Oscillation on the $v''(1) \rightarrow v'(0)$ ($\lambda = 357.7$ nm) and the $v''(0) \rightarrow v'(1)$ ($\lambda = 315.9$ nm) transitions also occurs, although with lower intensity. Table 10.2 summarizes some spectroscopic data for the N_2 laser.

* Under different operating conditions, laser action can also take place in the near infrared (0.74–1.2 μm) in the first positive system involving the $B^3\Pi_g \rightarrow A^3\Sigma_u^+$ transition.

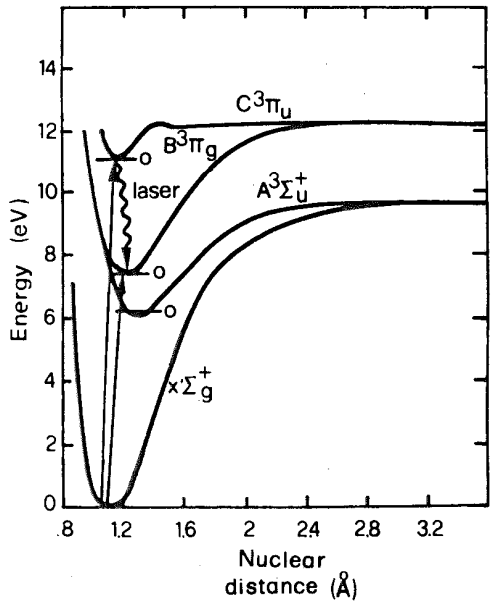

FIG. 10.19. Energy states of the N_2 molecule. For simplicity, only the lowest vibrational level ($v = 0$) is shown for each electronic state.

TABLE 10.2 Spectroscopic properties of uv laser transitions and gas mixture composition in nitrogen and KrF lasers

Laser Type	N_2	(KrF)*
Laser wavelength (nm)	337.1	248
Cross section (10^{-14} cm^2)	40	0.05
Upper state lifetime (ns)	40	10
Lower state lifetime (ns)	10 μs	
Transition linewidth (THz)	0.25	3
Partial pressure of gas mixture (mbar)	40 (N_2)	120 (Kr)
	960 (He)	6 (F_2)
		2400 (He)

Given the high pressure of the gas mixture (~40 mbar of N_2 and 960 mbar of He) and the corresponding high electric field (~10 kV/cm), a TEA configuration (as in Fig. 10.17) is normally used for a nitrogen laser. To obtain the required rapid current pulse (5–10 ns), the discharge circuit must have as low an inductance as possible. Due to the high gain of this self-terminating transition, oscillation occurs in the form of ASE, so the laser can be operated even without mirrors. Usually, however, a single mirror is placed at one end of the laser, since this reduces the threshold gain and hence the threshold electrical energy for ASE emission (see Sect. 2.9.2). The mirror also ensures a unidirectional output and reduces the beam divergence. With this type of laser, it is possible to obtain laser pulses of high peak power (~1 MW) and short duration (~10 ns) at high repetition rates (to ~100 Hz). Nitrogen lasers, with nitrogen pressure up to atmospheric pressure and without helium, have also been developed. In this case, the problem of arcing is alleviated by further reducing (to ~1 ns) the duration of the voltage pulse. The increased gain per unit length, due to the higher N_2 pressure, and the fast discharge imply that this type of laser is usually operated without mirrors. The length can be kept very short (10–50 cm) and, as a consequence, output pulses of short time duration can be obtained (~100 ps with 100-kW peak power). Nitrogen lasers of both long (~10 ns) and short (~100 ps) pulse duration are still used as pumps for dye lasers, since most dyes absorb strongly in the uv.

10.2.3.4. Excimer Lasers

These lasers represent an interesting and important class of molecular laser involving transitions between different electronic states of special molecules referred to as excimers.[17] Consider a diatomic molecule A_2 with potential energy curves as in Fig. 10.20, for ground and excited states, respectively. Since the ground state is repulsive, the molecule cannot exist in this state; i.e., the species exists only in the monomer form A in the ground state. However, since the potential energy curve shows a minimum for the excited state, the species is bound in this state; i.e., it exists in dimer form. Such a molecule A_2^* is called an *excimer*, a contraction of the words excited dimer. Suppose that a large fraction of excimers are somehow produced in the given volume of the medium. Under appropriate conditions, laser action can then occur on the transition between the upper (bound) state and the lower (free) state (bound-free transition). This is referred to as an excimer laser; a classical example is the Ne_2^* laser, the first excimer laser to be operated ($\lambda = 170$ nm).[16]

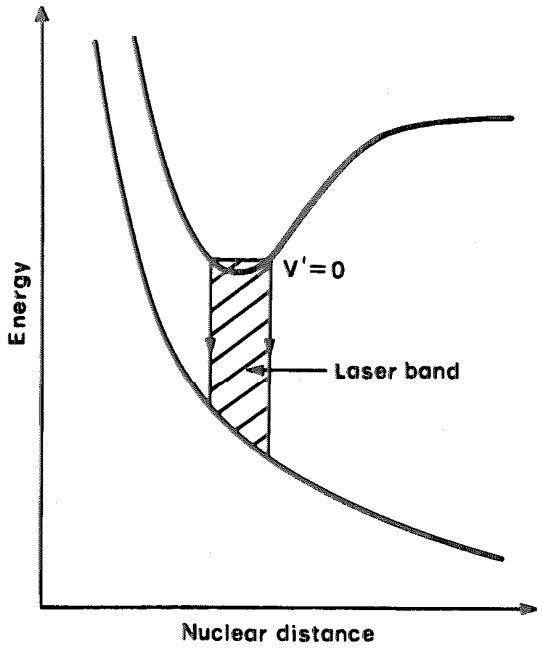

FIG. 10.20. Energy states of an excimer laser.

Excimer lasers have three notable and important properties: (1) Since the transition occurs between different electronic states of a molecule, the corresponding transition wavelength generally falls in the uv spectral region. (2) Once the molecule reaches the ground state, having undergone stimulated emission, it rapidly dissociates due to the repulsive potential of this state. This means that the lower laser level can be considered empty, so the laser operates according to the four-level laser scheme. (3) Due to the lack of energy levels in the ground state, no rotational-vibrational transitions there exist and the transition is observed to be featureless and relatively broad ($\Delta\nu = 20-100\ \text{cm}^{-1}$). Note, however, that, in some excimer lasers, the energy curve of the ground state does not correspond to a pure repulsive state, but it features a (shallow) minimum. In this case the transition occurs between an upper bound state and a lower (weakly) bound state (bound-bound transition). However, since the ground state is only weakly bound, a molecule in this state undergoes rapid dissociation either by itself (a process referred to as *predissociation*) or as a result of the first collision with another species of the gas mixture. Thus, in this case also, light emission produces a continuous spectrum.

We now consider a particularly important class of excimer laser in which a rare gas atom (notably Kr, Ar, Xe) is combined, in the excited state, with a halogen atom (notably F, Cl) to form a rare-gas-halide excimer.* Specific examples are ArF ($\lambda = 193\,\text{nm}$), KrF ($\lambda = 248\,\text{nm}$), XeF ($\lambda = 351\,\text{nm}$), and XeCl ($\lambda = 309\,\text{nm}$); all oscillate in the uv. Rare gas halides are readily formed, in the excited state, when an excited rare gas atom reacts with a ground-state halogen. In fact an excited rare-gas atom becomes chemically similar to an alkali atom, and such an atom is known to react readily with halogens. This analogy also indicates that bonding in the excited state has an ionic character. In the bonding process, the excited electron is transferred from the rare gas atom to the halogen atom. This bound state is also referred to as a charge transfer state.

* Strictly speaking these should not be referred to as excimers, since they involve binding between unlike atoms. In fact the word exciplex, a contraction of excited complex, was suggested as more appropriate for this case. However, the word excimer is now widely used in this context, so we follow this usage.

We now consider the KrF laser in some detail, since it represents one of the most important lasers of this category (Fig. 10.21). The upper laser level is an ionically-bound charge-transfer state that, at large internuclear distances ($R \rightarrow \infty$), corresponds to the ^2P state of the Kr positive ion and to the ^1S state of the negative F ion. Thus, for large internuclear distances, energy curves of the upper state obey the Coulomb law. The interaction potential between the two ions therefore extends to much greater distances (0.5–1 nm) than those occurring when covalent interactions predominate (compare with, e.g., Fig. 10.19). The lower state is covalently bonded; at large internuclear distances ($R \rightarrow \infty$), it corresponds to the ^1S state of the Kr atom and the ^2P state of the F atom. As a result of interaction of the corresponding orbitals, both upper and lower states are split, for short internuclear distances, into the $^2\Sigma$ and $^2\Pi$ states well known from molecular spectroscopy. Laser action occurs on the $B^2\Sigma \rightarrow X^2\Sigma$ transition, since it exhibits the largest cross section. Note that, during the transition, the radiating electron transfers from the F^- to the Kr^+ ion. Table 10.2 shows some relevant spectroscopic data for this transition.

The two main excitation mechanisms responsible for producing KrF excimers arise from either excited Kr atoms or Kr ions. The route involving excited atoms can be described by the following reactions

$$e + \mathrm{Kr} \rightarrow e + \mathrm{Kr}^* \tag{10.2.11a}$$

$$\mathrm{Kr}^* + \mathrm{F_2} \rightarrow (\mathrm{KrF})^* + \mathrm{F} \tag{10.2.11b}$$

where Kr is first excited by a discharge electron, then reacts with a fluorine molecule. The route involving Kr ions can be described by the following three reactions

$$e + \mathrm{Kr} \rightarrow 2e + \mathrm{Kr}^+ \tag{10.2.12a}$$

$$e + \mathrm{F_2} \rightarrow \mathrm{F}^- + \mathrm{F} \tag{10.2.12b}$$

$$\mathrm{F}^- + \mathrm{Kr}^+ + \mathrm{M} \rightarrow (\mathrm{KrF})^* + \mathrm{M} \tag{10.2.12c}$$

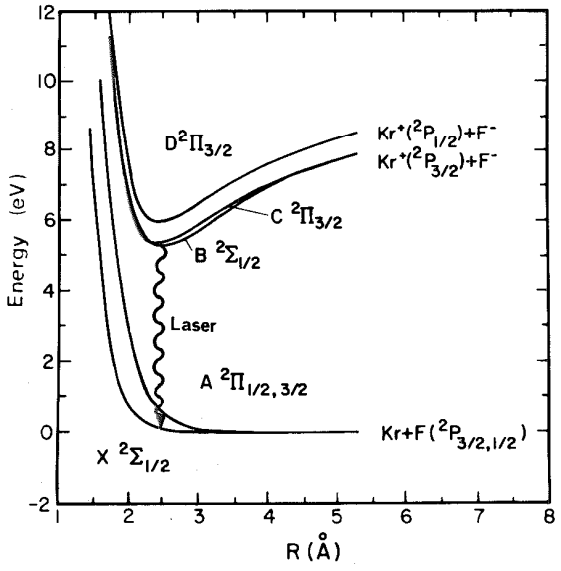

FIG. 10.21. Potential energy diagram showing the energy states of KrF. (From Ref. 17, with kind permission from Elsevier Science-NL, Sara Burgerhartstraat 25, 1055 KV Amsterdam, The Netherlands.)

involving first production of Kr and F ions, then their recombination, in the discharge volume, in the presence of a third partner (usually He, referred to as a buffer gas) to satisfy both energy and momentum conservation. Note that reaction (10.2.12b) is a peculiar one (it is usually referred to as dissociative attachment) and results from the high electron affinity of F atoms. Note also that, due to the long-range interaction between the two reacting ions, reaction (10.2.12c) can proceed very rapidly provided the buffer gas pressure is sufficiently high. Indeed, He partial pressures well above atmospheric pressure are normally used. (A typical gas mixture may contain ~120 mbar of Kr, 6 mbar of F_2, and 2400 mbar of He.) Under this condition, the reaction pathway described by reaction (10.2.12) becomes the dominant mechanism of (KrF)* production.

Since the pressure of the gas mixture is above atmospheric pressure, excimer lasers can be operated only in a pulsed regime, so the general TEA configuration in Fig. 10.17 is used; however, the components of the laser tube and laser flow system must now be compatible with the highly reactive F_2 gas. Furthermore, due to the shorter lifetime of the upper state and to avoid the onset of arc formation, faster pumping is usually provided for excimer lasers compared to TEA CO_2 lasers. (Pump durations of 10–20 ns are typical.) For standard systems, preionization is achieved, as in Fig. 10.17, by a row of sparks. For the largest systems, more complex preionization arrangements are adopted, which use either an auxiliary electron beam or an x-ray source.

Excimer lasers with high repetition rates (up to ~500 Hz) and high average power (up to ~100 W) are commercially available, while larger laboratory systems exist with a higher average power (in excess of a few kilowatts). The efficiency of these lasers is relatively quite high (2–4%) as a result of the high quantum efficiency (see Fig. 10.21) and the high efficiency of the pumping processes.

Excimer lasers are used to ablate plastics as well a biological materials with great precision, since these materials exhibit strong absorption at uv wavelengths. In fact, in some of these materials, the penetration depth for each laser pulse may be only a few micrometers. Due to the strong absorption and short pulse duration, a violent ablation process is produced, wherein the material is directly transformed into volatile components. Applications include drilling very precise holes in thin plastic films (as used, e.g., in the ink jet printer head) and corneal sculpting, to change the refractive power of the eye and hence correct myopia. In the field of lithography, the 248-nm uv light provides a good illumination source for achieving submicron-size features in semiconductor microchips. Excimer lasers can also be used as dye laser pumps, since most dyes absorb strongly in the uv.

10.3. CHEMICAL LASERS

A *chemical laser* is usually defined as one in which the population inversion is *directly* produced by an exothermic chemical reaction.* Chemical lasers usually involve either an associative or a dissociative chemical reaction between gaseous elements.[18,19]

An associative reaction can be described by an equation of the form $A + B \rightarrow AB$. In an exothermic reaction, some of the reaction heat appears as either rotational-vibrational or

* According to this definition, the gas dynamic CO_2 laser, briefly considered in Sect. 6.1., is not a chemical laser even though the upper state population arises ultimately from a combustion reaction.

electronic energy of the molecule AB. Thus, if a population inversion is achieved, the associative reaction can, in principle, lead to either a vibrational-rotational or a vibronic transition. In spite of much effort, however, only chemical lasers operating on vibrational-rotational transitions have been demonstrated so far. For this kind of transition, oscillation wavelengths so far range from 3 to 10 μm; the HF and DF lasers considered next are the most notable examples.

A dissociative reaction can be described by an equation of the general form $ABC \rightarrow A + BC$. If the reaction is exothermic, some of the reaction heat can be left as either electronic energy of the atomic species A or as internal energy of the molecular species BC. The most notable example of a laser exploiting this type of reaction is the atomic iodine laser, in which iodine is chemically excited to its $^2P_{1/2}$ state, so laser action occurs between the $^2P_{1/2}$ state and the $^2P_{3/2}$ ground state ($\lambda = 1.315\,\mu$m). Excited atomic iodine can be produced by the exothermic dissociation of CH_3I (or CF_3I, C_3F_7I), the dissociation being produced by means of uv light (~300 nm) from powerful flash lamps.

More recently, excited iodine was produced by generating excited molecular oxygen from molecular chlorine reacting with hydrogen peroxide. The molecular oxygen, excited to its long-lived singlet state (the ground electronic state of oxygen molecule is a triplet state), in turn transfers its energy to atomic iodine (oxygen-iodine chemical laser).

Chemical lasers are important for two main reasons: (1) They provide an interesting example of direct conversion of chemical energy into electromagnetic energy. (2) They are potentially able to provide either high output power (in cw operation) or high output energy (in pulsed operation). This occurs because the amount of energy available in an exothermic chemical reaction is usually quite large.*

10.3.1 HF Laser

HF chemical lasers can be operated by using either SF_6 or F_2 as compounds to donate the atomic fluorine; from a practical view point, the two lasers are very different.

In commercial devices, the inert SF_6 molecule is used as a fluorine donor, and the gas mixture also contains H_2 and a large amount of He. An electrical discharge is then used to dissociate the SF_6 and excite the reaction. The overall pressure of the mixture is around atmospheric pressure; the laser is pulsed, and the laser configuration is very similar to that of a CO_2 TEA laser. The output energy of this type of device is however appreciably smaller than the input electrical energy. Thus the laser derives only a small part of its output energy from the chemical reaction, so it can be considered only marginally to be a chemical laser.

In an $F_2 + H_2$ chemical laser, a certain amount of atomic fluorine is produced, by dissociation, from fluorine molecules. This atomic fluorine can then react with molecular hydrogen according to the reaction

$$F + H_2 \rightarrow HF^* + H \tag{10.3.1}$$

which produces atomic hydrogen. This atomic hydrogen can then react with molecular fluorine according to the second reaction:

$$H + F_2 \rightarrow HF^* + F \tag{10.3.2}$$

* For example, a mixture of H_2, F_2, and other substances (16% of H_2 and F_2 in a gas mixture at atmospheric pressure) has a heat of reaction of 2000 J/liter, of which 1000 J is left as vibrational energy of HF (a large value in terms of available laser energy).

Atomic fluorine is then restored, after this second reaction, so this fluorine atom can repeat the same reaction cycle, and so on. We thus have a classical chain reaction that can result in a large production of excited HF molecules. Note that the heats of reaction for Eqs. (10.3.1) and (10.3.2) are 31.6 kcal/mole and 98 kcal/mole, respectively; the two reactions are therefore referred to as the cold and hot reaction, respectively. Note also that, in the case of the cold reaction, the energy released, $\Delta H = 31.6$ kcal/mole, can easily be shown to correspond to an energy of $\Delta H \cong 1.372$ eV for each molecular HF produced. Now, the energy difference between two vibrational levels of HF, corresponding to a transition wavelength of $\lambda \cong 3\,\mu$m, is about $\Delta E \cong 0.414$ eV. So, if all this energy were released as vibrational excitation, vibrationally excited HF molecules, up to the $v = \Delta H/\Delta E \cong 3$ vibrational quantum number, could be produced (see Fig. 10.22a). However, the fraction of the reaction energy that goes into vibrational energy depends on the relative velocity of the colliding partners and on the orientation of this velocity compared to the H-H axis. In a randomly oriented situation, such as in a gas, one can then calculate the fraction of molecules found in the $v = 0$, 1, 2, or 3 vibrational states, respectively. The relative numbers $N(v)$ of excited HF molecules, in this way obtained, are also indicated in the same figure. For instance, 5 out 18 molecules are found in the $v = 3$ state and thus take up almost all the available energy as vibrational energy. On the other hand, 1 out of 18 molecules are found in the ground ($v = 0$) vibrational state and, in this case, all the reaction enthalpy is found as kinetic energy of the reaction products (mostly H, since this is the lightest product). From the figure we see that, if this were the only reaction, a population inversion would be established, particularly for the $(v = 2) \rightarrow (v = 1)$ transition.

In the case of the hot reaction, excited HF up to the $(v = 10)$ vibrational level can be produced (Fig. 10.22b). The relative populations of these vibrational levels $N(v)$ can also be calculated and are shown in the same figure. We see that a strong population inversion exists particularly for the $(v = 5) \rightarrow (v = 4)$ transition. Based on preceding considerations, we can

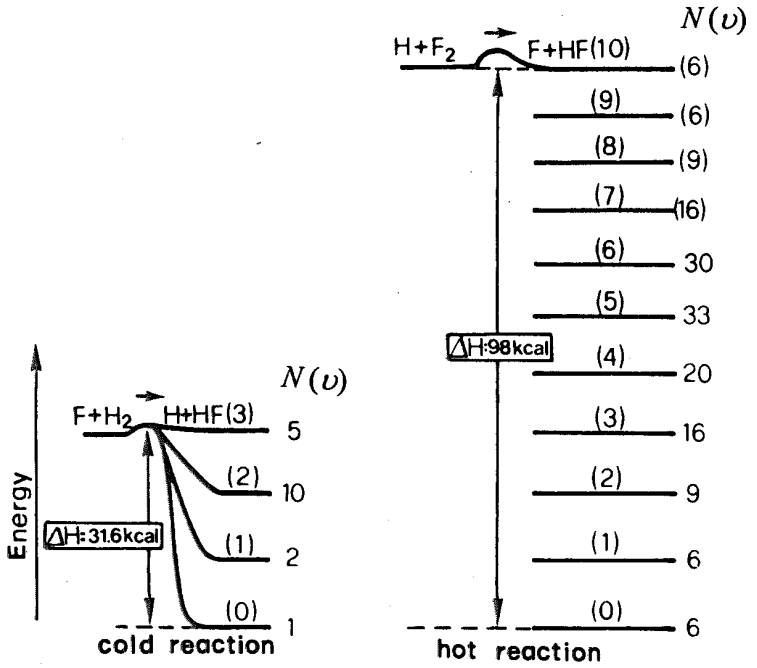

FIG. 10.22. Pumping vibrational levels of the HF molecule by the two reactions (a) $F + H_2 \rightarrow HF^* + H$ and (b) $H + F_2 \rightarrow HF^* + F$. The relative populations $N(v)$ of each vibrational state of quantum number v are also indicated in the two figures.

easily calculate that, e.g., for the cold reaction (10.3.1), more than 60% of the reaction energy is, on average, released as vibrational energy. To understand why the HF molecule is left in an excited vibrational state after a chemical reaction, consider an F atom colliding with a H_2 molecule. As a result of the high electron affinity of a fluorine atom, the interaction is strongly attractive, which leads to considerable polarization of the H_2 charge distribution, even at large F-H_2 distances. As a consequence of the electron's low inertia, an electron can then be transferred to the fluorine atom from the nearest hydrogen atom, hence forming the HF ionic bond, before the spacing between hydrogen and fluorine has adjusted to the internuclear separation corresponding to the HF equilibrium distance. This classical picture indicates that, after a reaction has occurred, the HF molecule is left in an excited vibrational state.

We can see from the preceding discussion that, as a consequence of the combined effect of cold and hot reactions described by Eqs. (10.3.1) and (10.3.2), a population inversion between several vibrational levels of HF occurs. If the active medium is placed in a suitable resonator, laser action on a number of transitions from vibrationally excited HF molecules is thus expected. Laser action has indeed been observed on several rotational lines from the $(v = 1) \rightarrow (v = 0)$ transition up to the $(v = 6) \rightarrow (v = 5)$ transition. In fact, due to the anharmonicity of the interaction potential, the vibrational energy levels in Fig. 10.22 are not equally spaced, so the laser spectrum actually consists of many roto-vibrational lines encompassing a rather wide spectral range ($\lambda = 2.7$–3.3 μm). It should be noted that the number of observed laser transitions is larger than expected according to the population inversion in Fig. 10.22. As discussed in the case of a CO laser, there are two reasons why oscillation can occur on so many lines: (1) The phenomenon of cascading: If, in fact, the $(v = 2) \rightarrow (v = 1)$ transition (usually the strongest one) lases, the population will be depleted from level 2 and will accumulate in level 1. Consequently, laser action on the $(v = 3) \rightarrow (v = 2)$ and $(v = 1) \rightarrow (v = 0)$ transitions now becomes more favored. (2) The phenomenon of partial inversion, according to which there may be a population inversion between some rotational lines even when no inversion exists between overall populations of the corresponding vibrational levels. Finally, it should be noted that, besides laser action in HF, laser action can also be achieved in the analogous compounds DF, HCl, and HBr, thus providing oscillation on a large number of transitions in the 3.5–5 μm range.

Figure 10.23 shows a possible configuration for a high-power cw HF or DF laser. Fluorine is thermally dissociated by an arc jet heater, then expanded to supersonic velocity (~Mach 4) through appropriate expansion nozzles. Molecular hydrogen is then mixed downstream through appropriate perforated tubes inserted in the nozzles. Downstream in the

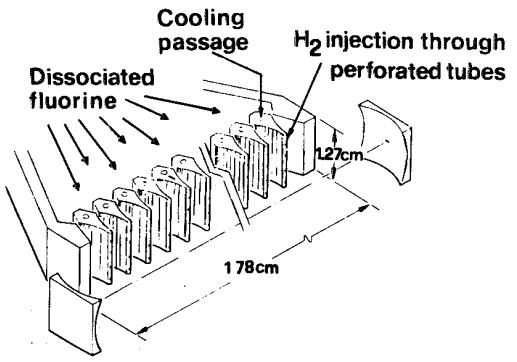

FIG. 10.23. Supersonic diffusion HF (or DF) chemical laser. (By permission from Ref. 18).

expansion regions, excited HF molecules are produced by chain reactions (10.3.1) and (10.3.2); a suitable resonator, with its axis orthogonal to the flow direction, is placed around this region. To handle the large power available in the expanding beam (usually of large diameter) unstable resonators exploiting metallic, water-cooled, mirrors are often used. Chemical lasers of this type can produce very large cw output powers (in the megawatt range!) with good chemical efficiency.

Pulsed TEA-type HF lasers are commercially available, and these have found a limited use when an intense source of middle-infrared radiation is needed (e.g., in spectroscopy). HF and DF chemical lasers of the type shown in Fig. 10.23 are used exclusively for military applications. Safety considerations have prevented the use of these lasers for commercial applications. In fact the F_2 molecule is one of the most corrosive and reactive elements known; its waste products are difficult to dispose of and, under certain conditions, the chain reaction (10.3.1) and (10.3.2) may even become explosive. In the military field, due to the large available output powers, these lasers can be used as directed energy weapons to, e.g., destroy enemy missiles. A military cw device named MIRACL (Mid-Infrared Advanced Chemical Laser), using DF, has given the largest cw power of any laser (2.2 MW). DF rather than HF was used because the system was intended for use from a ground station and DF emission wavelengths fall in a region of relatively good atmospheric transmission. High-power hydrogen-fluoride or, more likely, oxygen-iodine chemical lasers are under active consideration for use from either a high-altitude plane to destroy missiles during ballistic flight or from a space station to destroy missiles during their lift-off phase (when the rocket has lower speed and hence is more vulnerable).

10.4. FREE-ELECTRON LASERS

In free-electron lasers (FELs) an electron beam moving at a speed close to the speed of light passes through the magnetic field generated by a periodic structure (called the wiggler or undulator; see Fig. 10.24).[20] The stimulated emission process occurs through the interaction of the em field of the laser beam with these relativistic electrons moving in the periodic magnetic structure. As in any other laser, two end mirrors provide feedback for laser oscillation. Using suitable bending magnets, the electron beam is first injected into the laser cavity and then deflected out of the cavity.

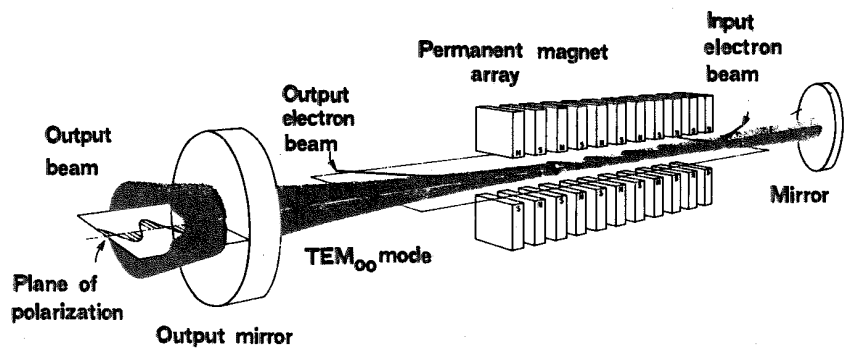

FIG. 10.24. Basic structure of a free-electron laser. (Courtesy of Luis Elias, University of California, at Santa Barbara Quantum Institute.)

To understand how this interaction occurs, we first consider the case of spontaneously emitted radiation, i.e., when no mirrors are used. Once injected into the periodic structure, the electrons acquire a wiggly, or undulatory, motion in the plane orthogonal to the magnetic field (Fig. 10.24). The resulting electron acceleration produces a longitudinal emission of the synchrotron radiation type. The frequency of the emitted radiation can be derived, heuristically, by noting that the electron oscillates in the transverse direction at an angular frequency $\omega_q = (2\pi/\lambda_q)v_z \cong (2\pi/\lambda_q)c$, where λ_q is the magnet period and v_z is the (average) longitudinal velocity of the electron (which is almost equal to the vacuum light velocity c). Let us now consider a reference frame moving longitudinally at velocity v_z. In this frame, the electron oscillates essentially in the transverse direction; thus it looks like an oscillating electric dipole. In this reference frame, due to the Lorentz time contraction, the oscillation frequency is given by

$$\omega' = \frac{\omega_q}{[1-(v_z/c)^2]^{1/2}} \tag{10.4.1}$$

and this is therefore the frequency of the emitted radiation. If we now go back to the laboratory frame, the radiation frequency undergoes a (relativistic) Doppler shift. The observer frequency ω_0 and the corresponding wavelength λ_0 are then given by

$$\omega_0 = \frac{1+(v_z/c)}{[1-(v_z/c)^2]^{1/2}}\omega' \cong \frac{2\omega_q}{1-(v_z/c)^2} \tag{10.4.2}$$

and

$$\lambda_0 = \frac{\lambda_q}{2}\left[1-\left(\frac{v_z}{c}\right)^2\right] \tag{10.4.3}$$

respectively. Note that, since $v_z \cong c$, λ_0 is generally much smaller than the magnet period. To calculate the quantity $[1-(v_z/c)^2]$ in Eqs. (10.4.2) and (10.4.3), we recall that, for a completely free electron moving with velocity v_z along the z-axis, one has $[1-(v_z/c)^2] = (m_0c^2/E)^2$, where m_0 is the rest mass of the electron and E its energy. However, for a given total energy, the wiggling motion reduces the value of v_z, i.e., it increases the value of $[1-(v_z/c)^2]$. A detailed calculation then shows that this quantity is given by

$$1-\left(\frac{v_z}{c}\right)^2 = (1+K^2)\left(\frac{m_0c^2}{E}\right)^2 \tag{10.4.4}$$

where the numerical constant K, which is usually smaller than 1, is referred to as the undulator parameter. Its value is obtained from the expression $K = e\langle B^2\rangle^{1/2}\lambda_q/2\pi m_0c^2$, where B is the magnetic field of the undulator and the average is taken along the longitudinal direction. From Eqs. (10.4.2)–(10.4.4), we obtain

$$\omega_0 = \frac{4\pi c}{\lambda_q}\left(\frac{1}{1+K^2}\right)\left(\frac{E}{m_0c^2}\right)^2 \tag{10.4.5}$$

and

$$\lambda_0 = \frac{\lambda_q}{2}\left(\frac{m_0c^2}{E}\right)^2(1+K^2) \tag{10.4.6}$$

which shows that the emission wavelength can be changed by changing the magnet period λ_q and/or the energy E of the electron beam. Assuming, as an example, $\lambda_q = 10\,\text{cm}$ and $K = 1$, we find that the emitted light can range from the infrared to the ultraviolet by changing the electron energy from 10^2 to 10^3 MeV. Note that, according to our earlier discussion, the emitted radiation is expected to be polarized in the plane orthogonal to the magnetic field direction (see also Fig. 10.24).

To calculate the spectral lineshape and the bandwidth of the emitted radiation, we observe that, in the reference frame previously considered, the electron emission lasts for a time $\Delta t' = (l/c)[1-(v_z/c)^2]^{1/2}$, where l is the overall length of the wiggler magnet. Using Eq. (10.4.1) we then see that emitted radiation from each electron consists of a square pulse containing a number of cycles $N_{cyc} = \omega'\Delta t'/2\pi = l/\lambda_q$, i.e., equal to the number of periods $N_w = l/\lambda_q$ of the wiggler. From standard Fourier-transform theory, it then follows that such a pulse has a power spectrum of the $[\sin(x/2)/(x/2)]^2$ form, where $x = 2\pi N_w(\nu - \nu_0)/\nu_0$. The spectral width $\Delta\nu_0$ (FWHM) is then approximately given by the relation:

$$\frac{\Delta\nu_0}{\nu_0} = \frac{1}{2N_w} \tag{10.4.7}$$

Figure 10.25a shows this spectrum as a function of the dimensionless quantity x. Since all electrons, injected with the same velocity and in the same direction, show the same lineshape, Eq. (10.4.7) gives the homogeneous linewidth for the FEL laser. Inhomogeneous effects arise from such factors as spread in electron energy, angular divergence of the electron beam, and variation in magnetic field over the beam cross section. Note that, since the number of undulator periods may typically be $N_w \sim 10^2$, from Eq. (10.4.7) one has $\Delta\nu_0/\nu_0 \cong 5\times10^{-3}$.

It is worthwile to point out that there is an alternative way of considering the behaviour of the emitted rediation. In the rest frame of the electron, that we considered earlier, the magnetic field of the undulator appears to move at nearly the velocity of light. It can be shown that the static magnetic field then appears to the electrons essentially like a counter-propagating em wave. The synchrotron emission can therefore be considered to arise from Compton backscattering of this virtual em wave from the electron beam. For this reason, the corresponding type of FEL is sometimes referred to as operating in the Compton regime (Compton FEL).

A calculation of the stimulated emission cross section requires a detailed analysis, which we do not consider here, of the interaction between a longitudinally propagating em wave and the electron propagating in the wiggler magnetic field. We merely point out that, unlike the situation previously considered for other lasers, the spectral distribution of this cross section is not the same as that for spontaneously emitted radiation; instead it is proportional to its frequency derivative. Accordingly, its shape is as shown in Fig. 10.25b, with gain on the low-frequency side and loss on the high-frequency side of the transition. This unusual behavior essentially arises because the interaction is based on a light-scattering process rather than absorption or emission from bound states.

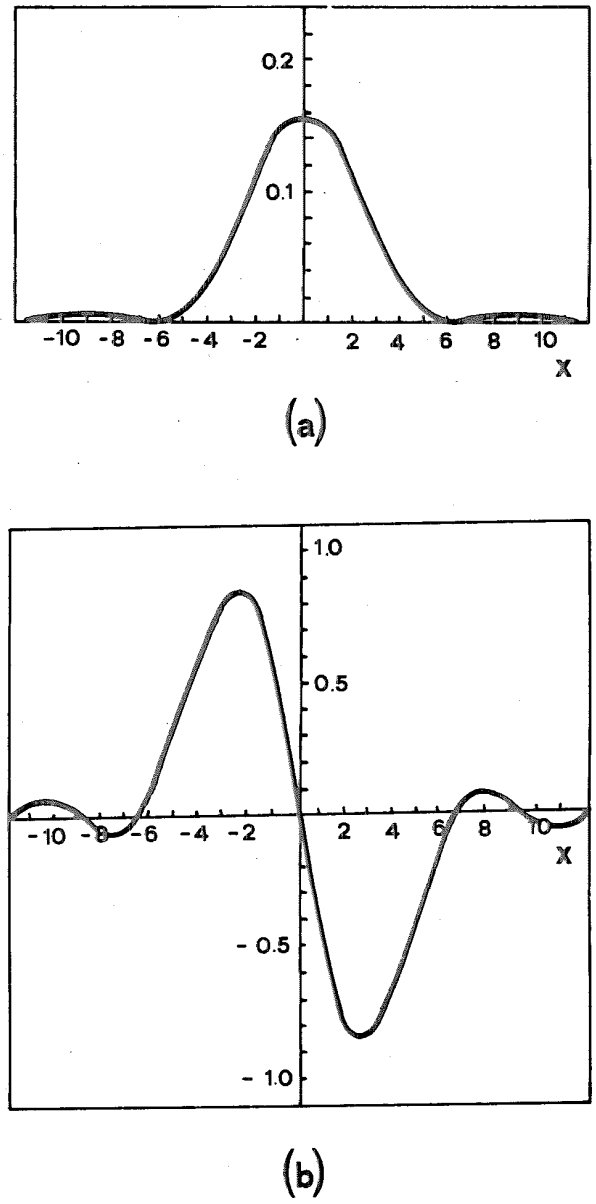

FIG. 10.25. Spectrum (a) of the spontaneously emitted radiation and (b) the stimulated emission cross section in a free-electron laser as a function of the normalized quantity $z = 2\pi N_w(\nu - \nu_0)/\nu_0$.

So far, demonstrations of FEL operation have been made on several devices (more than 10) around the world, with oscillation wavelengths ranging from millimeter waves to the uv region. All of these lasers require large facilities, since they involve using rather large *e*-beam accelerators. Historically, the first FEL was operated at $\lambda = 3.4$ μm using the Stanford University superconducting linear accelerator.[21] Since the incoming *e*-beam consisted of 3.2-ps pulses separated by $\tau = 84.7$ ns, the cavity length L was chosen so that τ equals the cavity round-trip time (i.e., $L = c\tau/2 = 12.7$ m); thus, the laser was operated in the synchronously mode-locked regime.

One of the most important issues for a FEL is related to its efficiency. Since the emitted frequency depends on electron energy [see Eq. (10.4.5)], the maximum energy which can be extracted from the electron is that which shifts its energy so that the corresponding operating frequency falls outside the gain curve. Consequently the maximum efficiency η_{max}, defined as the ratio between the maximum energy given to the laser beam and the initial electron

energy, is approximately given by $\Delta\nu_0/\nu_0$, i.e., $\eta_{max} = (1/2N_w)$. This means that the efficiency in such a device is rather limited (10^{-2}–10^{-3}). Two ways of obtaining higher efficiency are being actively pursued: (1) The period of the magnet is gradually decreased along the *e*-beam direction to keep the λ_q/E^2 ratio constant (tapered wiggler). (2) The energy remaining in the electron beam, after leaving the wiggler, is recovered by decelerating the electrons. Much higher efficiencies are predicted to be achievable using these approaches, and indeed they have been achieved to some degree.

As a final comment we point out that all the FELs described so far use high-energy ($E > 10$ MeV) and low-current ($I \sim 1$–100 A) *e*-beam machines. Under these conditions, as previously discussed, light emission can be described as arising from Compton scattering of the virtual quanta of the magnetic field from individual electrons (*Compton regime FEL*). Free electron lasers using *e*-beams of lower energy ($E = 1$–2 MeV) and much higher currents ($I \sim 10$–20 kA) have also been operated. In this case the electron-electron interaction becomes so strong that collective oscillatory motions (plasma waves) are induced in the *e*-beam when interacting with the em wave in the wiggler. The emission can then be considered to arise from scattering of the virtual quanta of the magnetic field from these collective motions, rather than from single electrons. The emitted frequency $\nu_0 = 2\pi/\omega_0$ is then no longer given by Eq. (10.4.5), but in fact it is downshifted by the frequency of this collective motion. The phenomenon is analogous to Raman scattering of light from molecular vibrations; the corresponding laser is said to operate in the *FEL-Raman regime.* Because of the lower value of electron energy involved, these lasers oscillate in the millimeter wave region.

To conclude this section we list the most attractive properties of FELs: Wide tunability, excellent beam quality (close to the diffraction limit), and potentially very high efficiency and thus very high laser power (average power of the *e*-beam of the Stanford Linear Accelerator is about 200 kW). Free-electron lasers are however inherently large and expensive machines; interest in their applications is thus likely to be strongest in frequency ranges where more conventional lasers are not so readily available, e.g., the far-infrared (100–400 μm) or vacuum uv ($\lambda < 100$ nm).

10.5. X-RAY LASERS

The achievement of coherent oscillation in the x-ray region was a dream that is slowly but steadily coming true.[22] The potential applications of x-ray lasers are indeed very important. They include, in fact, such possibilities as: (1) X-ray holography or x-ray microscopy of, e.g., living cells or cell constituents, allowing, respectively, three-dimensional or two-dimensional pictures with subnanometer resolution to be obtained. (2) X-ray lithography, where patterns with extremely high resolution could be produced.

Before discussing what has been achieved so far in this wavelength region, we indicate the difficulties that must be overcome to obtain x-ray laser operation. Starting with fundamental considerations, we recall that the threshold pump power of a four-level laser is given by Eq. (7.3.12):

$$P_{th} = \frac{h\nu_{mp}}{\eta_p}\frac{\gamma A}{\sigma\tau} \tag{10.5.1}$$

The minimum threshold, P_{mth} is of course attained for $\sigma = \sigma_p$ where σ_p is the cross section at the transition peak. Furthermore, one must also take into account that, in the x-ray region, the upper state lifetime τ is established by the spontaneous lifetime τ_{sp}. From Eqs. (2.4.29) and (2.3.15) we then obtain $1/\sigma_p\tau_{sp} \propto \nu_0^2/g_t(0)$, independent of the transition matrix element $|\mu|$. For either Eq. (2.4.9a) (homogeneous line) or Eq. (2.4.28) (inhomogeneous line) we find that $g_t(0) \propto 1/\Delta\nu_0$, where $\Delta\nu_0$ stands for transition linewidth for either a homogeneous or inhomogenous line. Thus, in either case, from Eq. (10.5.1), with $h\nu_{mp} \cong h\nu_0$, we obtain $P_{mth} \propto \nu_0^3\Delta\nu_0$. At frequencies in the vuv to soft x-ray region and at moderate pressures, we assume that the linewidth is dominated by Doppler broadening. Hence [see Eq. (2.5.18)] one has $\Delta\nu_0 \propto \nu_0$ and P_{mth} is expected to increase as ν_0^4. At the higher frequencies, corresponding to the x-ray region, linewidth is dominated by natural broadening, since the radiative lifetime becomes very short (down to the femtosecond region). In this case one has $\Delta\nu_0 \propto 1/\tau_{sp} \propto \nu_0^3$ and P_{mth} is expected to increase as ν_0^6. Thus, if we go from, e.g., the green ($\lambda = 500$ nm) to the soft x-ray region ($\lambda \cong 10$ nm), the wavelength decreases by a factor of 50 and P_{mth} is expected to increases by many orders of magnitude!

From a technical viewpoint, a major difficulty arises from the fact that multilayer dielectric mirrors for the x-ray region are lossy and difficult to make. A basic problem is that the difference in refractive index between various materials becomes very small in this region. Dielectric multilayers with a large number of layers (hundreds) are therefore needed to achieve reasonable reflectivity. Light scattering at the many interfaces then makes the mirrors very lossy; furthermore, the mirrors have difficulty withstanding the high intensity of an x-ray laser beam. For these reasons, so far, x-ray lasers have been operated without mirrors as ASE devices.

As a representative example, we consider the soft x-ray laser based on 24-times ionized selenium (Se^{24+}) as the active medium.[23] In fact, this is the first laser of a kind (the *x-ray recombination laser*) which now includes a large number of other multiply-ionized species as laser media. Pumping was achieved by the powerful second-harmonic beam ($\lambda = 532$ nm) of the Novette laser (pulse energy ~1 kJ, pulse duration ~1 ns), consisting of one arm of the Nova laser at Lawrence Livermore Laboratory in the United States. The beam is focused to a fine line ($d \cong 200$ μm, $l = 1.2$ cm) on a thin stripe (75 nm thick) of selenium, evaporated on a 150-nm-thick foil of Formvar (Fig. 10.26). The foil can be irradiated from one or both sides. Exposed to the high intensity of this pump beam ($\sim 5 \times 10^{13}$ W/cm^2), the foil

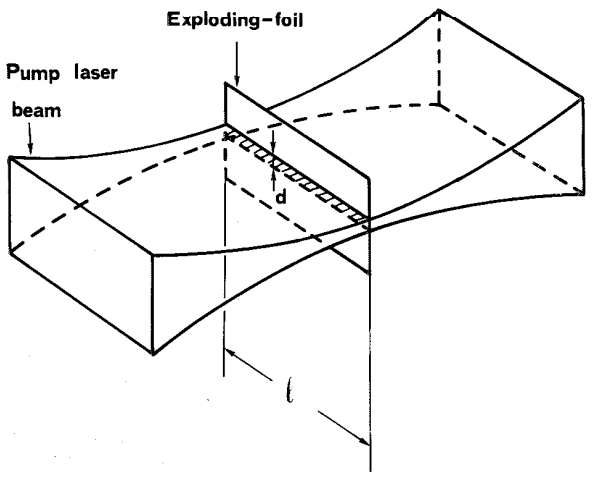

FIG. 10.26 Transverse irradiation geometry of a soft x-ray laser using the exploding-foil technique.

explodes to form a highly ionized, approximately cylindrical, selenium plasma whose diameter is $d \cong 200\,\mu$m. During the electron-ion recombination process, a particulary long-lived constituent of this plasma, is formed, which consists of Se^{24+}. This ion has the same ground-state electronic configuration as neutral Ne ($1s^2 2s^2 2p^6$; see Fig. 10.1); accordingly, it is usually referred to as neon-like selenium. Impact collisions with hot-plasma electrons ($T_e \cong 1$ keV) then raise Se^{24+} from its ground state to excited states, thereby achieving population inversion between the states $2p^5 3p$ and $2p^5 3s$ because the lifetime of the $3s \rightarrow$ ground-state transition is much shorter than the lifetime of the $3p \rightarrow 3s$ transition. (Both transitions are electric-dipole allowed.) With the pump configuration in Fig. 10.26, a strong longitudinal emission due to ASE is observed on two lines ($\lambda_1 = 20.63$ nm and $\lambda_2 = 20.96$ nm) of the $2p^5 3p \rightarrow 2p^5 3s$ transition (see Fig. 10.1). Due to the much higher nuclear charge of Se compared to Ne, these lines fall in the soft x-ray region. From the length dependence of the emitted energy, one deduces that a maximum single-pass gain, $G = \exp(\sigma_p N l)$, of about 700 was obtained. Note that this gain is still well below the threshold for ASE, as defined in Sect. 2.9.2. In fact, for the experimental situation described here, the emission solid angle is $\Omega \cong 10^{-4}$ sterad and the linewidth is still expected to be dominated by Doppler broadening. From Eq. (2.9.4b) we then obtain $G_{th} \cong 4.5 \times 10^5$. This means that the emitted intensity, due to ASE, is still much smaller than the saturation intensity of the amplifier. Indeed, the x-ray output energy produced was an extremely small fraction ($\sim 10^{-10}$) of the pump energy.

Since this first laser was demonstrated, research activity in this field has been very strong.[24] Thus many new active media have been operated, namely many more neon-like ions (from Ag^{37+} to Ar^{8+}), many hydrogen-like ions (from Al^{12+} to C^{5+}), lithium-like ions (from Si^{11+} to Al^{10+}), and nickel-like ions (from Au^{51+} to Eu^{35+}). The range of oscillation wavelengths now extends from ~3.6 to 47 nm, while the single-pass gain G generally ranges from 10 to 10^3. To achieve the high peak powers required [see Eq. (10.5.1)] and at the same time reduce the required pump energy, picosecond or even femtosecond laser pulses are now often used for pumping. Amplified spontaneous emission (at $\lambda = 46.9$ nm) has also been observed in neonlike Ar^{8+} by passing a strong current pulse, of short duration, through a 1–10 cm long capillary filled with Ar.

10.6. CONCLUDING REMARKS

Chapter 10 considers the most notable examples of lasers involving low-density media. In general these lasers tend to be bulkier and often less efficient than lasers considered in Chapter 9 (notably semiconductor and diode-pumped solid-state lasers). For these reasons, whenever possible, such low-density lasers are tending to be superseded by their solid-state laser counterparts. Such is the case for the Argon laser, which faces strong competition from the green beam emitted by a diode-pumped Nd laser (e.g., Nd:YVO_4) with intracavity second-harmonic generation. For quite a few applications, this is also the case of the red-emitting He-Ne laser, which faces strong competition from red-emitting InGaAlP semiconductor lasers. Low-density lasers will however survive in frequency ranges not covered effectively by semiconductor or diode-pumped solid-state lasers. This is, for instance, the case for middle-infrared lasers (the CO_2 lasers being the most notable example), and lasers oscillating in the uv (e.g., excimer lasers) and x-ray spectral regions.

Another field of applications where low-density lasers will continue to perform well is where very high powers are required, with CO_2 lasers, excimer lasers, and chemical lasers as important examples. Thus, as a conclusion, one can foresee that lasers based on low-density media will continue to play an important role in the laser field.

PROBLEMS

10.1. List at least four lasers, using a low-density active medium, whose wavelengths fall in the infrared.

10.2. List at least four lasers, using a low-density active medium, whose wavelengths fall in the uv to soft x-ray region. What problems are faced in achieving laser action in the uv or x-ray region?

10.3. Metal-working applications require a laser with a cw output >1 kW. Which lasers meet this requirement?

10.4. The 514.5-nm transition of an argon ion laser is Doppler-broadened to a linewidth of ~3.5 GHz. The cavity length of the laser is 100 cm; when pumped three times above threshold, the laser emits a power of 4 W in a TEM_{00} mode profile. Assuming that the frequency of one of the oscillating TEM_{00} modes coincides with the center of the gain line, calculate the number of TEM_{00} modes expected to oscillate.

10.5. Consider the argon ion laser described in Problem 10.4 and assume that the laser is mode-locked by an acoustooptic modulator. Calculate: (a) The duration and peak power of the mode-locked pulses; (b) the drive frequency of the rf oscillator.

10.6. Assume that the bond between the two nitrogen atoms of the N_2 molecule can be simulated by a spring of suitable elastic constant. Knowing the vibrational frequency (Fig. 10.9) and the atomic mass, calculate the elastic constant. Compare this constant with that obtainable from the ground-state curve in Fig. 10.19.

10.7. Show that if the elastic constant of the N-N bond is the same as that of the isoelectronic CO molecule, the $(v' = 1) \rightarrow (v = 0)$ transition wavelengh of the N_2 molecule is approximately the same as that of the CO molecule.

10.8. Assume that each of the two oxygen-carbon bonds of the CO_2 molecule can be simulated by a spring with elastic constant k. Assuming there is no interaction between the two oxygen atoms and knowing the ν_1 frequency ($\nu_1 = 1337\ \text{cm}^{-1}$), calculate this constant.

10.9. Knowing the elastic constant k between the two oxygen carbon bonds obtained in Problem 10.8, calculate the expected frequency ν_3 of the asymmetric stretching mode and compare the result with the value shown in Fig. 10.9.

10.10. Show that each C-O bond of the CO_2 molecule cannot be simulated by elastic springs if the harmonic oscillation corresponding to the bending mode of frequency ν_2 has to be calculated.

10.11. Knowing that, for a Boltzmann distribution, the maximum population of the upper laser level of a CO_2 molecule occurs for the rotational quantum number $J' = 21$ (see Fig. 10.11), calculate the rotational constant B [assume $T = 400$ K, which corresponds to an energy kT such that $(kT/h) \cong 280\ \text{cm}^{-1}$]. From this value calculate the equilibrium distance between the C atom and each O atom.

10.12. Using the result from Problem 10.11, calculate the frequency spacing (in cm^{-1}) between the rotational lines of the CO_2 laser transition. (Assume that the rotational constant of the lower laser level is the same as that of the upper laser level and remember that only levels with odd values of J are occupied in a CO_2 molecule.)

10.13. The linewidth due to collision broadening of the CO_2 laser transition is given by $\Delta\nu_c = 7.58(\psi_{CO_2} + 0.73\psi_{N_2} + 0.6\psi_{He})p(300/T)^{1/2}$ MHz where ψ are fractional partial pressures of the gas mixture, T is the gas temperature, and p is the total pressure (in torr) (see Example 3.3). Taking the ratio of the partial pressures of CO_2, N_2, and He molecules as 1:1:8 and assuming a separation between rotational lines of the CO_2 laser transition of $\Delta\nu_r \cong 2\ cm^{-1}$, calculate the total gas pressure needed to make all rotational lines merge together. What is the width of the gain curve?

10.14. Consider a CO_2 laser with high enough pressure to have all its rotational lines merged together. If this laser is mode-locked, what is the order of magnitude of the corresponding laser pulse width?

10.15. Show that a reaction energy of 31.6 kcal/mole, as in the HF cold reaction [see Eq. (10.3.1)], is equivalent to an energy of 1.372 eV released for each molecular reaction.

10.16. Considering the cold reaction in Fig. 10.22a, take the values shown in the figure for the relative populations of HF molecules that are left in the first three vibrational levels after reaction. Calculate the fraction η of heat released in the reaction that goes into vibrational energy.

10.17. Repeat the previous calculation for the hot reaction in Fig. 10.22b.

10.18. To reach the final end products of the cold reaction [see Eq. (10.3.1)], we can choose a reaction path where we first dissociate the H_2 molecule to obtain the single atoms F, H, and H. Then we let the fluorine and one hydrogen atom recombine together. Similarly, for the hot reaction [see Eq. (10.3.2)], we first dissociate molecular fluorine, then recombine one fluorine with the hydrogen atom. Given the two possibilities, relate the difference in reaction heat from these two reactions to the difference in dissociation energy in the fluorine and hydrogen molecules.

REFERENCES

1. R. Arrathoon, Helium-Neon Lasers and the Positive Column, in *Lasers*, vol. 4 (A. K. Levine and A. J. De Maria, eds.) (Marcel Dekker, New York, 1976), Chap. 3.
2. W. B. Bridges, Atomic and Ionic Gas Lasers, in *Methods of Experimental Physics*, vol. 15 (C. L. Tang, ed.) (Academic, New York, 1979), pp. 33–151.
3. A. Javan, W. R. Bennett, and D. H. Herriott, Population Inversion and Continuous Optical Maser Oscillation in a Gas Discharge Containing a He-Ne Mixture, *Phys. Rev. Lett*, **6** (1961).
4. C. E. Webb, Metal Vapor Lasers, Recent Advances and Applications, in *Gas Flow and Chemical Lasers*, Springer Proceedings in Physics N. 15 (S. Rosenwork ed.), (Springer-Verlag, Berlin, 1987), pp. 481–494.
5. C. C. Davis and T. A. King, Gaseous Ion Lasers, in *Advances in Quantum Electronics*, vol. 3 (D. W. Goodwin, ed.) (Academic, New York, 1975), pp. 170–437.
6. D. H. Dunn and J. N. Ross, Argon Ion Laser, in *Progress in Quantum Electronics*, vol. 4 (J. H. Sanders and S. Steinholm, eds.) (Pergamon, London, 1977), pp. 233–270.
7. W. B. Bridges, Laser Oscillation in Singly Ionized Argon in the Visible Spectrum, *Appl. Phys. Letters* **4**, 128 (1964).
8. P. K. Cheo, CO_2 Lasers, in *Lasers*, Vol. 3 (A. K. Levine and A. J. De Maria, eds.) (Marcel Dekker, New York, 1971), Chap. 2.
9. A. J. De Maria, Review of High-Power CO_2 Lasers, in *Principles of Laser Plasma*, (G. Bekefi, ed.) (Wiley, New York, 1976), Chap. 8.

10. C. K. N. Patel, W. L. Faust, and R. A. McFarlane, CW Laser Action on Rotational Transitions of the $\Sigma_u^+ \rightarrow \Sigma_g^+$ Vibrational Band of CO_2, *Bull. Am. Phys. Soc.* **9**, 500 (1964).
11. D. R. Hall and C. A. Hill, Radiofrequency-Discharge-Excited CO_2 Lasers, in *Handbook of Molecular Lasers* (P. Cheo, ed.) (Marcel Dekker, New York, 1987), Chap. 3.
12. K. M. Abramski, A. D. Colley, H. J. Baker, and D. R. Hall, Power Scaling of Large-Area Transverse Radiofrequency Discharge CO_2 Lasers, *Appl. Phys. Letters* **54**, 1833 (1989).
13. P. E. Jackson, H. J. Baker, and D. R. Hall, CO_2 Large-Area Discharge Laser Using an Unstable Waveguide Hybrid Resonator, *Appl. Phys. Letters* **54**, 1950 (1989).
14. R. E. Center, High-Power, Efficient Electrically Excited CO Laser, in *Laser Handbook*, vol. 3 (M. L. Stitch, ed. (North-Holland, Amsterdam, 1979), pp. 89–133.
15. C. S. Willet, *An Introduction to Gas Lasers: Population Inversion Mechanisms* (Pergamon, Oxford, UK, 1974), Sects. 6.2.1, 6.2.3.
16. N. G. Basov, V. A. Danilychev, and Y. M. Popov, Stimulated Emission in the Vacuum Ultraviolet Region, *Soviet J. Quantum Electrons.* **1**, 18 (1971).
17. J. J. Ewing, Excimer Lasers, in *Laser Handbook*, vol. 3 (M. L. Stitch, ed.) (North-Holland, Amsterdam, 1979), pp. 135–97.
18. A. N. Chester, Chemical Lasers, in *High-Power Gas Lasers* (E. R. Pike, ed.) (Institute of Physics, Bristol and London, 1975), pp. 162–221.
19. C. J. Ultee, Chemical and Gas Dynamic Lasers, in *Laser Handbook*, vol. 3 (M. L. Stitch and M. Bass, eds.) (North-Holland, Amsterdam, 1985), pp. 199–287.
20. G. Dattoli and R. Renieri, Experimental and Theoretical Aspects of the Free-Electron Lasers, in *Laser Handbook*, vol. 4 (M. L. Stitch, ed.) (North-Holland, Amsterdam, 1979), pp. 1–142.
21. D. A. G. Deacon, L. R. Elias, J. M. J. Madey, G. J. Ramian, H. A. Schwettman, and T. I. Smith, First Operation of a Free-Electron Laser, *Phys. Rev. Lett.* **38**, 892 (1977).
22. R. C. Elton, *X-Ray Lasers* (Academic, Boston, 1990).
23. D. L. Matthews *et al.*, Demonstration of a Soft X-Ray Amplifier, *Phys. Rev. Lett.* **54**, 110 (1985).
24. *X-Ray Lasers 1996*, (S. Svanberg and C. G. Wahlstrom, eds.), Institute of Physics Conference Series N. 151 (Institute of Physics, Bristol 1996).